AD-A261 117

ENTATION PAGE

Form Approved
OMB No. 0704-0188

(2)

	PORT DATE	3. REPORT TYPE AND DATES COVERED
	Oct 92	Final 25 Jun 91 - 24 Jun 92

4. TITLE AND SUBTITLE

Theoretical and Experimental Investigation of Electron Beam Acceleration and Sub-Millimeter Wave Generation

5. FUNDING NUMBERS

DAAL03-91-G-0190

6. AUTHOR(S)

Professor N.C. Luhmann, Jr.
Dr. D.B. McDermott

7. PERFORMING ORGANIZATION NAME(S) AND ADDRESS(ES)

University of California, Los Angeles
Electrical Engineering Department
405 Hilgard Avenue
Los Angeles, CA 90024

8. PERFORMING ORGANIZATION REPORT NUMBER

9. SPONSORING/MONITORING AGENCY NAME(S) AND ADDRESS(ES)

U. S. Army Research Office
P. O. Box 12211
Research Triangle Park, NC 27709-2211

10. SPONSORING/MONITORING AGENCY REPORT NUMBER

ARO 28396.1-PH

11. SUPPLEMENTARY NOTES

The view, opinions and/or findings contained in this report are those of the author(s) and should not be construed as an official Department of the Army position, policy, or decision, unless so designated by other documentation.

12a. DISTRIBUTION/AVAILABILITY STATEMENT

Approved for public release; distribution unlimited.

12b. DISTRIBUTION CODE

13. ABSTRACT *(Maximum 200 words)*

The overall objective of our research for ARO is to develop devices that have the potential for being compact generators of submillimeter-wave radiation. (1) The high-harmonic gyro-frequency multiplier, which is an efficient generator of high frequency rf, will be tested at the tenth-harmonic in our rebuilt test-stand. (2) High-power harmonic gyro-TWTs can be designed to operate in high order modes in large size waveguide by using the marginal stability design criterion. (3) Our high power, second-harmonic TE_{21} gyro-TWT, which is predicted to generate an order of magnitude higher power than state-of-the-art fundamental frequency gyrotrons, has been fully designed and construction is well underway. (4) The interaction strength in our high-harmonic CARM increases as the electron Larmor radius moves closer to the wall radius as the magnetic field is lowered towards a grazing intersection. (5) A high performance amplifier is predicted to result from our initial gryo-klystron experiment.

14. SUBJECT TERMS

Submillimeter-wave radiation, compact generators, frequency multiplication, high-harmonic, gyro-TWT, stability

15. NUMBER OF PAGES

16. PRICE CODE

17. SECURITY CLASSIFICATION OF REPORT	18. SECURITY CLASSIFICATION OF THIS PAGE	19. SECURITY CLASSIFICATION OF ABSTRACT	20. LIMITATION OF ABSTRACT
UNCLASSIFIED	UNCLASSIFIED	UNCLASSIFIED	UL

THEORETICAL AND EXPERIMENTAL INVESTIGATION OF ELECTRON BEAM ACCELERATION AND SUB-MILLIMETER WAVE GENERATION

Final Report

Table of Contents

I. FORWARD

A major objective of our research under the ARO contract is to investigate novel approaches which will lead to practical, high frequency (> 100 GHz) sources. For cost effectiveness, we have carried out a significant portion of the work at lower frequencies where we can economically assemble the basic experiments necessary to carry out proof-of-principle physics studies. One must demonstrate ingenuity and cleverness to make dramatic advances with our moderate level of funding. However, as discussed in detail in Secs. III and IV, all of the devices under study have the potential for high frequency operation.

During the last year of the contract, four important papers describing our ARO-funded contributions to millimeter-wave and sub-millimeter wave source development were published in Special Issues of Scholarly Journals. The paper, "Marginal Stability Design Criterion for Gyro-TWTs and Comparison of Fundamental with Second Harmonic Operation," by A.T. Lin, K.R. Chu, C.C. Lin, C.S. Kou, D.B, McDermott and N.C. Luhmann, Jr., (*Int. J. Electronics*, 72, 873 (1992)) introduced a method for building stable gyro-TWTs with the best performance possible. The papers, "High-Power Harmonic Gyro-TWT's - Part I: Linear Theory and Oscillation Study," by C.S Kou, Q.S. Wang, D.B. McDermott, A.T. Lin, K.R. Chu, and N.C. Luhmann, Jr., (*IEEE. Trans on Plasma Science*, 20, 155, (1992)) and "High-Power Harmonic Gyro-TWTs -Part II: Nonlinear Theory and Design," by Q.S. Wang, C.S. Kou, D.B. McDermott, A.T. Lin, K.R. Chu, and N.C. Luhmann, Jr. (*IEEE Trans. on Plasma Science*, 20, 163 (1992)), explained why harmonic gyro-TWTs can be expected to deliver extremely high power and yet remain stable. Finally, the paper, "Bragg Reflectors," by C.K. Chong, D.B. McDermott, M.M. Razeghi, N.C. Luhmann, Jr., J. Pretterebner, D. Wagner, M. Thumm, B. Kulke and M. Caplan (IEEE Trans. on Plasma Science 20, 393 (1992)), describes the performance and capability of a frequency selective reflector that is sure to play an important role in future high power overmoded oscillators.

The organization of this final report is as follows. Section II contains a list of the report's illustrations, tables and appendixes. Section III states the objectives of the research. A summary of the research findings is presented in Sec. IV with references given in Sec. IV.F. Our publications and technical reports produced during the last year are listed in Sec. V. Section VI lists all scientific personnel at UCLA participating in the research. Section VII contains the report on inventions. Copies of four publications funded by the contract are included in the Appendix.

II. LIST OF ILLUSTRATIONS, TABLES AND APPENDIXES

Illustrations

Tables

Appendixes

III. STATEMENT OF PROBLEM

The overall objective of our research for ARO is to develop devices that have the potential for being compact generators of submillimeter-wave radiation. Our efforts have focussed on gyrotron devices because they have proven to be efficient generators. High frequency gyrotrons can be made more compact by reducing the cathode voltage and by operating at harmonics of the cyclotron frequency which reduces the required magnetic field by a factor of the harmonic number. In the first eight years of our ARO funding, we developed high-harmonic gyro devices driven by rf-accelerated electron beams, with an eleventh-harmonic gyrotron, a fifth-harmonic gyro-klystron amplifier and an eighth-harmonic gyro-TWT amplifier being three notable accomplishments. It is of interest to note that industry (Varian, Litton and Northrop) is currently developing several types of high-harmonic gyro-amplifiers at 95 GHz, based in large part on our work. Additional research efforts include a successful 250 GHz CARM oscillator experimental collaboration with Lawrence Livermore National Laboratory.

During the most recent contract period, we have continued our development of gyro-devices that have a potential for high frequency, high harmonic operation. (1) The high harmonic gyro-frequency multiplier is an efficient generator of high frequency rf, where the harmonic number can be as high as ten, or perhaps even higher. The primary problem is to inject an electron beam into the accelerator with a beam radius much smaller than the transverse wavelength of the mode being excited. Another major problem is to taper the magnet field so that the electrons continuously lose energy during their transit through the cavity. (2) Using the marginal stability design criterion, high-power harmonic gyro-TWTs can be designed to operate in high order modes in large size waveguide. The primary problem is to determine the start-oscillation lengths for all modes in the tube. The other major problem is to find whether there is sufficient gain for the gyro-TWT's operating mode. (3) In our high power, second-harmonic TE_{21} gyro-TWT, the primary problem will be to create an electron beam with a small spread in its axial velocity. Another major problem will be to suppress harmonic gyro-BWO modes whose instability can be excited by poorly terminated severs. (4) The high harmonic CARM will also be dependent on a high quality electron beam. In addition, the circuit must be sliced carefully to suppress the competing modes without interfering with the design mode. (5) In the initial gyro-klystron experiment, the primary problem will be to suppress gyrotron oscillation in the cavities. The next major problem will be to keep the beam sufficiently cold so that high efficiency can be realized. In the succeeding harmonic gyro-klystron experiments, it will be even more challenging to suppress the excitation of the stronger, lower harmonic gyrotron modes in the cavities and in the drift-tubes.

IV. SUMMARY OF RESEARCH FINDINGS, 6/25/91 - 6/24/92

A. High Harmonic Gyro-Frequency Multiplier

Summary

A major objective of the program is to upgrade our previous third-harmonic gyro-frequency multiplier experiment to much higher output power and efficiency and at a much larger harmonic. A simulation code has been written to design the output cavity and investigate efficiency enhancement through magnetic tapering. Efficiencies as high as 70% are realizable. A new buncher/accelerator cavity has been built to accelerate much higher levels of electron beam current. A new high-perveance electron beam injector has been built and successfully tested for injecting the required higher values of beam current.

We have been involved in the design of a significant extension of our successful high harmonic gyro-frequency multiplier (i.e., prebunched gyrotron). In addition to potentially generating rf in the sub-mm wave region, the gyro-multiplier promises to be extremely efficient because the electrons from the rf-accelerator/buncher cavity enter the output cavity already bunched and, due to the extended gyro interaction, they remain in near resonance throughout the cavity. This results in a first-order interaction, rather than the weaker second-order interaction associated with the conventional gyrotron. The results of our first prebunched gyrotron experiment [1] was that our third harmonic multiplier generated 28 GHz rf with a conversion power of 6.7 kW with an efficiency of 13%. In this initial experiment, the beam's radial guiding center spread was fairly large so that all the electrons did not enter the multiplier cavity at the same decelerating phase as desired.

The high frequency potential of this device is primarily limited only by the availability of high power, high frequency sources to drive the accelerator/buncher cavity [2]. For example, a tenth-harmonic gyro-multiplier utilizing a 140 GHz rf-accelerator would generate high power electromagnetic waves with a wavelength of 0.21 mm in a magnetic field of 50 kG. Gyrotrons currently exist which can generate cw power levels of 0.5 MW at 140 GHz and higher frequency gyrotrons are under development. Therefore, this frequency multiplication approach offers exciting possibilities for submillimeter wave power generation.

The goals of the new experiment are 1) to use a much more tightly focused electron beam so that the entire beam enters the multiplier cavity closer to the same optimum phase, 2) to use a much higher value of beam current for higher power, 3) to operate at much higher harmonics, and 4) to design the cavity and/or use magnetic tapering for higher efficiency. We have decided to perform the next prebunched gyrotron experiment at the tenth harmonic, which will be at a frequency of 29 GHz since a 2.9 GHz, 1 MW klystron amplifier will be used. However, as mentioned above, this concept scales to much higher frequencies. We have built a new gyroresonant rf accelerator cavity. Whereas the cavity used in our previous experiments was designed to accelerate electrons to high energy (250-500 keV), the new cavity is designed to accelerate much higher current beams (2-5 A) to the more moderate energy of 50- 100 keV. The length of the new accelerator is roughly one-half

of the previous cavity. Also, lossy Eccosorb epoxy has been added to lower its loaded Q to 150. The cavity is currently undergoing cold-tests to measure its Q factor while we increase the coupling by enlarging the size of the coupling slots. Our simulation code has been used to study the acceleration characteristics of the new cavity. Figure 1 shows the performance that can be expected when using 75% of our available input power of 1 MW. As desired, the final electron energy and velocity ratio α ($= v_\perp/v_\parallel$) are relatively constant as the magnetic field is varied around the operating value of $\Omega_{co}/\omega_{acc} = 1.2$.

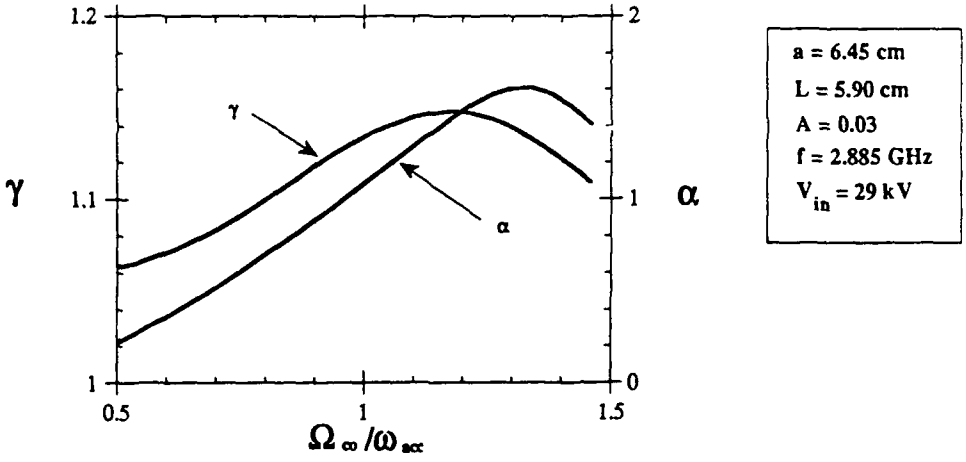

Figure 1: Predicted dependence of Lorentz factor and velocity ratio $\alpha = v_\perp/v_\parallel$ on ratio of rest-mass cyclotron frequency to accelerator rf frequency in gyroresonant TE_{111} rf accelerator. The field value of A = 0.03 would be achieved for Q=135 with a power of P = 750 kW.

We have devoted considerable effort to construct a high perveance electron gun and optimize the magnetic pole piece. The gun is identical to the electron gun from the SLAC 5045 Klystron, but scaled down in size by a factor of 3.5 for lower voltage operation. In order to achieve the same magnetic field shape as in the 5045 Klystron (but scaled by the same factor of 3.5), our magnetic pole piece has a DC offset coil and a Helmholtz gradient coil in addition to the iron pole piece. As shown in Fig. 2, the resultant magnetic field shape is a very close fit to the desired profile, especially at the emitting surface, which is the most important region. With this Pierce electron gun, we were able to successfully transmit a 5A, 30 kV beam through a 3 mm diameter aperture. In addition, the solenoid has been reconfigured to contain a separate solenoid for the electron gun and a long uniform region for the gyroresonant rf accelerator and gyro-multiplier cavities. The magnetic field profile of the new solenoid is shown in Fig. 3.

A particle tracing simulation code was written to design an optimized frequency multiplier cavity for the new experiment. To first order, where the finite beam size is neglected, all electrons follow the same trajectories in the multiplier cavity, and the structure of the cavity mode is unaffected by the beam. After the amplitude of the mode is specified, the code follows the electrons through the cavity by solving the equations of motion. In this way, a plot of efficiency versus wave amplitude can be constructed, which can then be made into a plot of efficiency versus beam current. This is a similar procedure to that used for gyrotron optimization [3]

Figure 4 shows one such plot for a cavity corresponding roughly to our previous exper-

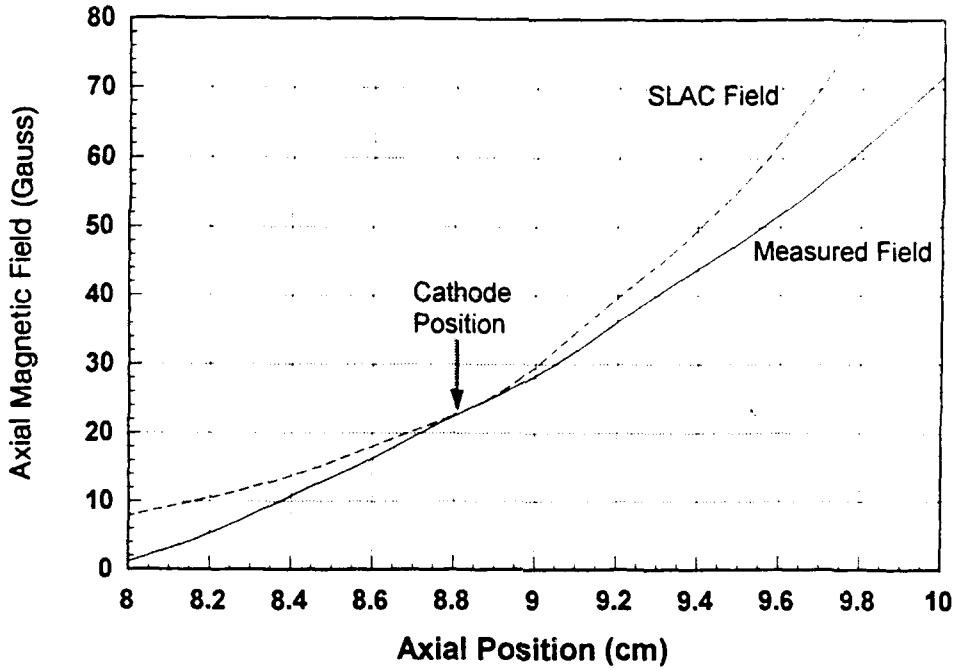

Figure 2: Dependence of magnetic field in electron gun for scaled SLAC 5045 gun from measurement (solid curve) and scaling of the actual SLAC 5045 profile (dashed curve). The center of the emitting surface is at $z = 8.8$ cm.

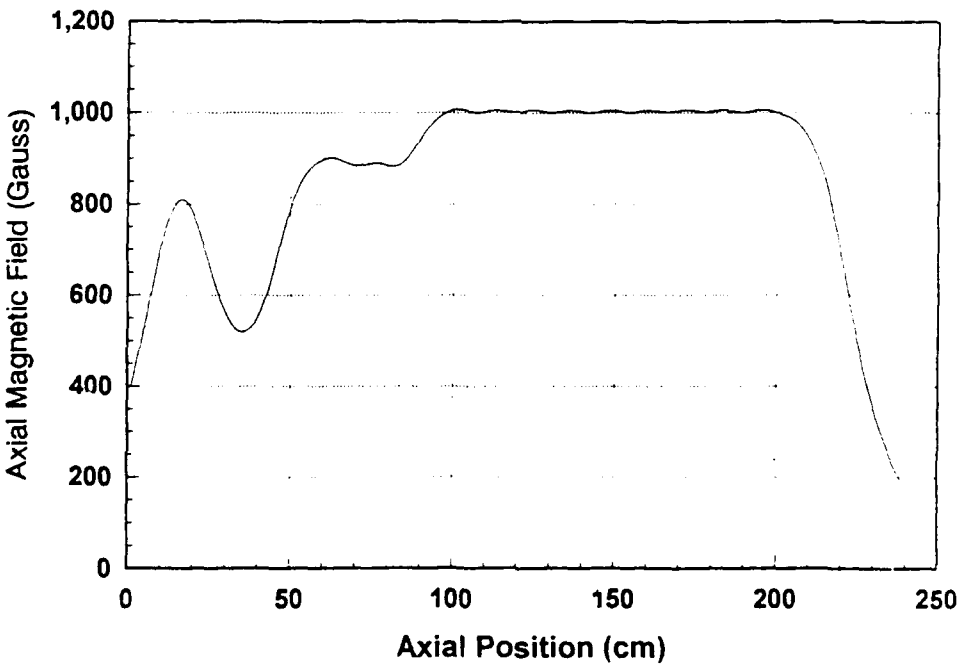

Figure 3: Profile of magnetic field in solenoid for high-harmonic gyro-frequency multiplier experiment.

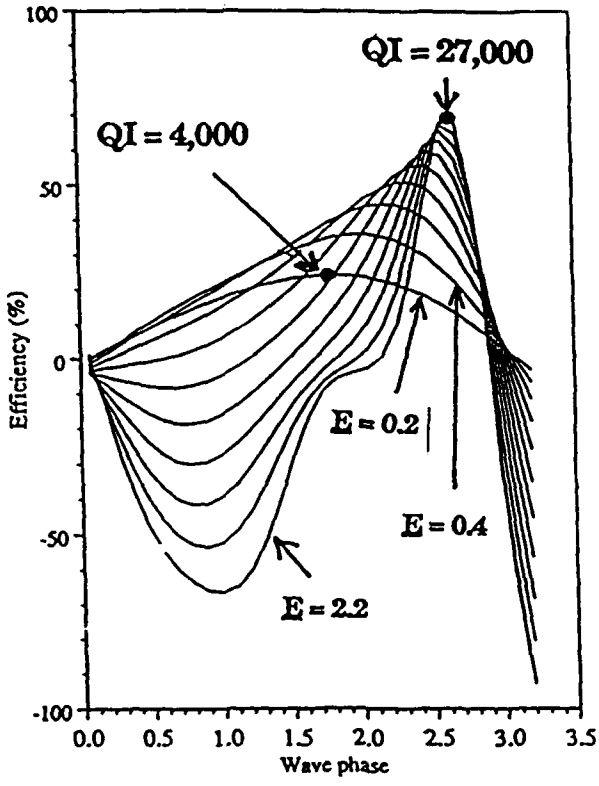

Figure 4: Dependence of conversion efficiency on phase of TE_{312} wave at input of third harmonic multiplier for ten values of normalized electric field amplitude, $\bar{E} \equiv E_o e r_w / mc^2$ (200 kV, α = 2.0, L/a = 2.0, $\bar{E}$ = 0.2, 0.4,..., 2.2).

iment. If the electrons enter the cavity at the optimum small-signal wave phase of $\phi = \pi$ (maximum deceleration), then the peak efficiency is 30%. The electrons fall out of resonance as they lose energy. An efficiency of nearly 70% is obtained if the electrons enter the cavity at the phase at which the electric field is a null. Although this situation probably is not realizable since the wave will grow for the phase which gives maximum small signal gain ($\phi = \pi$), a similar efficiency will result if the magnetic field is tapered. Magnetic tapering will be investigated. The purpose of making these plots is to determine the cavity Q at which the optimum efficiency will be attained for the available beam current. The cavity's length will be varied to find the value for optimum efficiency. We will also investigate the effectiveness of magnetic field tapering to prolong resonance and thereby enhance the efficiency. Since our solenoid is comprised of many discrete magnets, magnetic tapering is an option. Our code can also model a realistic beam with finite radial thickness. The beam's size determines the maximum harmonic for efficient operation.

Our well-collimated electron beam will allow efficient operation at the tenth harmonic. Using the particle-tracing simulation code, we have begun to design a 29 GHz, $TE_{10,1,2}$ mode tenth-harmonic gyro-multiplier cavity. Although this proof-of-principle experiment will generate power at 29 GHz by using a 2.9 GHz rf-accelerator/buncher, it must be noted that power at much higher frequency can be generated by using a higher frequency accelerator/buncher cavity. For example, by using a 0.5 MW cw, 140 GHz gyrotron to drive the accelerator/buncher cavity, a scaled ten-harmonic multiplier will generate cw power at 1.4 THz.

B. Overmoded Gyro-TWT Stability

Summary

A gyro-TWT amplifier can be stabilized by breaking it into several short stable interaction sections separated by attenuating severs for isolation. The marginal stability design procedure can be used to design any arbitrary s^{th}-harmonic TE_{mn}-mode gyro-TWT by first determining the start-oscillation length of the relevant harmonic gyrotron and gyro-BWO competing modes. The length of the interaction sections must be less than the shortest start-oscillation length. The number of interaction sections is then chosen to obtain the desired gain.

High power, submillimeter-wave devices are more readily built if the interaction waveguide's transverse dimensions are as large as possible. To increase a gyro-TWT's lateral dimensions, it is necessary to increase the operating mode number of the waveguide. For example, the inner diameter of a 110 GHz gyro-TWT designed for the TE_{52} mode would be 1 cm, whereas it would be only 2 mm if the lowest order TE_{11} mode were employed. A conventional device's stability, which is problematic even in a fundamental mode device, would be highly unlikely for such an overmoded case. However, the marginal stability design criterion [4] that we developed considerably relaxes the design constraints. Using this procedure, an overmoded gyro-TWT would be comprised of many short stable isolated sections.

We are investigating whether the marginal stability design criterion can be used to build a high performance, fundamental frequency TE_{01} gyro-TWT, which was the configuration of the first gyro-TWTs to be tested. [5] If they can be kept stable, the TE_{0n} modes are probably the best modes to operate a gyro-TWT because of their low ohmic dissipation and their favorable interaction strength. We will use the new technique, the marginal stability design procedure, to design a stable TE_{01} gyro-TWT amplifier. For the TE_{01} device, the dominant competing mode that must be suppressed is the TE_{21} gyro-BWO. Therefore, the interaction sections of the gyro- TWT must be chosen shorter than the start-oscillation length for the TE_{21} gyro-BWO. One must then determine how much gain for the TE_{01} mode will result for that length. It will almost certainly be less than the gain required for most applications ($\geq$ 30 dB). Higher gain can be achieved by using several stable sections separated by attenuating severs.

C. High Power, Second Harmonic Gyro-TWT

Summary

An extremely high power three-section second-harmonic 35 GHz gyro-TWT has been designed with a self-consistent nonlinear simulation code [6]. An output power of 530 kW with 21 % efficiency, 54 dB gain and 6 % bandwidth is predicted. To substantiate the theoretical predictions that a harmonic gyro-TWT can generate significantly

higher output power with better stability than fundamental gyro-TWTs due to the higher beam currents allowed for the weaker harmonic interaction, a proof-of-principle Ku-band experiment is being constructed at UCLA with comparable performance predicted. A single anode 100 kV, 20 A MIG is being built to generate the $\alpha = v_\perp/v_\parallel = 1$ electron beam with $\Delta v_\parallel/v_\parallel = 8\%$. The input and rf couplers have been designed and are currently being built.

Operation at the second harmonic allows the requisite magnetic field to be reduced by a factor of two, an important concern for high frequency gyro-TWTs. Combining this with the case used in the previous section could result in a 220 GHz, TE_{52} gyro-TWT amplifier with an inner diameter of 0.5 cm in a magnetic field of $\sim$ 45 kG. Also, it must be pointed out that several years ago we successfully tested an eighth-harmonic gyro- TWT [7] under ARO funding.

Harmonic gyro-TWT's not only require a substantially weaker magnetic field and offer nearly the same high efficiency as conventional fundamental gyro-TWT's, but also have the potential to **stably** generate significantly higher levels of power [4, 6, 8]. Basically, since the harmonic interaction is generally weaker than the fundamental interaction, the threshold beam current level for oscillation is raised significantly. This is seen in Fig. 5 where the threshold beam current for the absolute instability is given for both a fundamental and a second-harmonic interaction (B_g is the magnetic field at which the particle wave resonance line grazes the operating waveguide mode curve). It is seen that for $\alpha = v_\perp/v_\parallel = 1$, the allowable electron beam current in a second harmonic gyro-TWT is higher by more than fivefold from that in a fundamental gyro-TWT. The higher working beam current not only provides a larger amount of beam power available for millimeter-wave power generation, but also makes up for the loss in interaction strength. Thus, a high performance amplifier with superior power capability is possible.

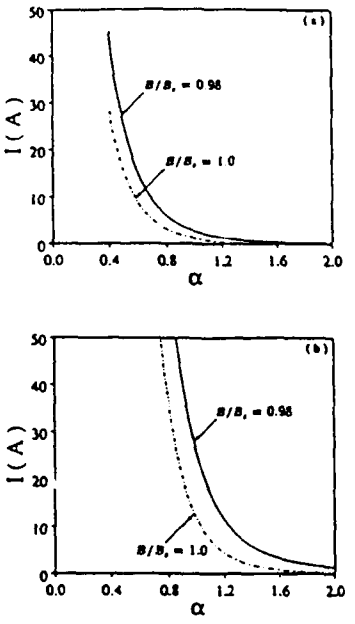

Figure 5: Dependence of threshold beam current for absolute instability on velocity ratio $\alpha = v_\perp/v_\parallel$ in (a) fundamental TE_{11} and (b) second-harmonic TE_{21} gyro-TWT amplifiers for two values of magnetic field (100 kV, axis-encircling beam).

The cold waveguide dispersion relation of the $TE_{21}^{(2)}$ gyro-TWT amplifier (the superscript refers to the cyclotron harmonic number) shown in Fig. 6 reveals the key feature that interaction at the fundamental cyclotron frequency will not occur. The optimum electron beam for a $TE_{21}^{(2)}$ gyro-TWT is an axis-encircling electron beam, because it would produce the strongest interaction and only $TE_{m1}^{(m)}$ interactions ($m \geq 2$) could then occur. However, since there has not yet been a successful demonstration of such a beam with the requisite low axial velocity spread, the designs given in this paper utilize MIG beams which have long been employed in the gyrotron community with great success.

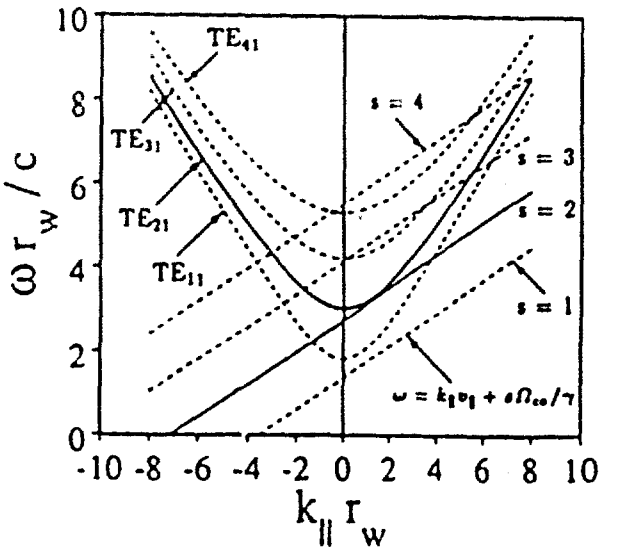

Figure 6: Uncoupled dispersion relation of operating mode (intersection of unbroken curves) and likely oscillating modes (intersections of broken curves with negative $k_\parallel$) for $TE_{21}^{(2)}$ gyro-TWT amplifier (100 kV, $\alpha = 1$, $B_0 = 0.98B_g$).

Based on a marginal stability procedure [4], a high power second harmonic TE_{21} gyro-TWT using a 100 kV, 25 A MIG beam with $\alpha = 1$ and $\Delta v_\parallel / v_\parallel = 5$ % has been designed [6], where the interaction tube is comprised of three sections separated by absorbing severs [9]. The length of each interaction section is shorter than the length at which the device will spontaneously oscillate and is determined through a combination of analytical theory and multi-mode PIC code simulation [6]. Figure 7 shows the threshold lengths for the most threatening oscillation modes in our $TE_{21}^{(2)}$ amplifier design. Here, the length of the interaction sections is limited by the start oscillation length for the *3rd* harmonic TE_{31} gyro-BWO mode. The number of sections is chosen to yield the desired gain. For the 530 kW $TE_{21}^{(2)}$ gyro-TWT described in Table I, the spatial power profile and frequency bandwidth obtained from nonlinear, self-consistent simulations are shown in Figs. 8 and 9 respectively. For a MIG beam with 5 % axial velocity spread, the FWHM constant-drive bandwidth is 6 % with a peak output power of 533 kW and efficiency of 21.3 % at 34.5 GHz. These results show that a harmonic gyro-TWT can deliver output power at least an order of magnitude higher than that possible in state-of-the-art fundamental gyro-TWTs.

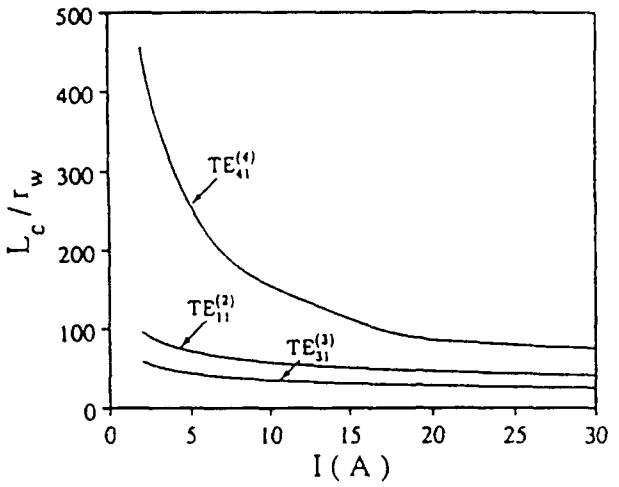

Figure 7: Oscillation threshold lengths for $TE_{31}^{(3)}$, $TE_{11}^{(2)}$ and $TE_{41}^{(4)}$ gyro-BWO modes as a function of beam current. r_w is the waveguide radius.

Table I: Second Harmonic Gyro-TWT Design

Beam Voltage	100 kV
Beam Current	25 A
$\alpha = v_\perp / v_\parallel$	1.0
Magnetic Field	6.4 kG
Center Frequency	35 GHz
Mode	TE_{21}
Cyclotron Harmonic	2nd
Circuit Radius	0.44 cm
r_c / r_w	0.4
B / B_g	0.98
$\Delta v_\parallel / v_\parallel$	5 %
Number of Stages	3
Sever Length	3 cm

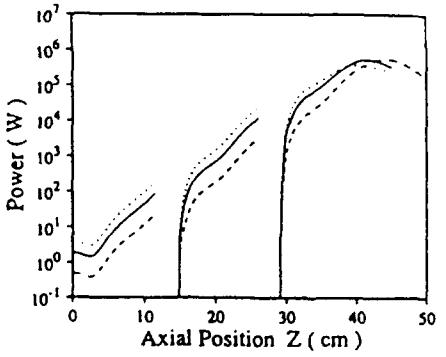

Figure 8: Predicted spatial power profile of 35 GHz wave in proposed three-stage $TE_{21}^{(2)}$ gyro-TWT (Table I) for input power of 0.5 W (dashed curve), 1.9 W (solid curve), and 4 W (dotted curve).

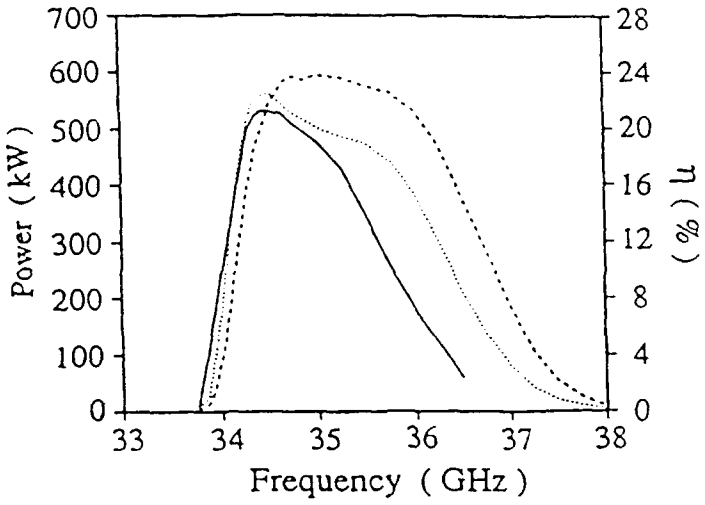

Figure 9: Constant-drive bandwidth of proposed three-stage $TE_{21}^{(2)}$ gyro-TWT (Table I) for axial velocity spreads of 0% (dashed curve), 3%(dotted curve) and 5% (solid curve) with input power of 0.21 W, 0.55 W and 1.9 W, respectively.

As seen from Fig. 7, the start oscillation length for the $TE_{41}^{(4)}$ gyro-BWO is approximately three times longer than for the $TE_{31}^{(3)}$ gyro-BWO. Therefore, if the TE_{31} and TE_{11} modes can be eliminated, a single-stage device can yield high gain and yet remain stable.

Such a single-stage proof-of-principle device is being built at UCLA on the ARO program with the design parameters listed in Table II. By slicing the cylindrical waveguide axially with two cuts separated in azimuth by 90°, both the TE_{11} and TE_{31} modes will be suppressed. A similar procedure was successfully employed in a previous experiment [10]. The performance of the gyro-TWT given in Table II was also numerically simulated. Compared with the previous multi-stage gyro-TWT design, the single-stage device provides comparable performance and is less sensitive to the beam's axial velocity spread. For the case of 8% axial velocity spread, a peak output power of 400 kW, peak efficiency of 20% and gain of 33 dB are predicted at 15.9 GHz and the FWHM constant-drive bandwidth is 6 %. The bandwidth of the gyro-TWT is shown in Fig. 10.

Table II : Proof-of-Principle Experiment Design

Beam Voltage	100 kV
Beam Current	20 A
$\alpha = v_\perp / v_\parallel$	1.0
Magnetic Field	2.9 kG
Center Frequency	16.1 GHz
Mode	TE_{21}
Cyclotron Harmonic	2nd
Circuit Radius	0.95 cm
r_c / r_w	0.4
B/B_g	0.98
$\Delta v_\parallel / v_\parallel$	8 %
Circuit Length	65 cm

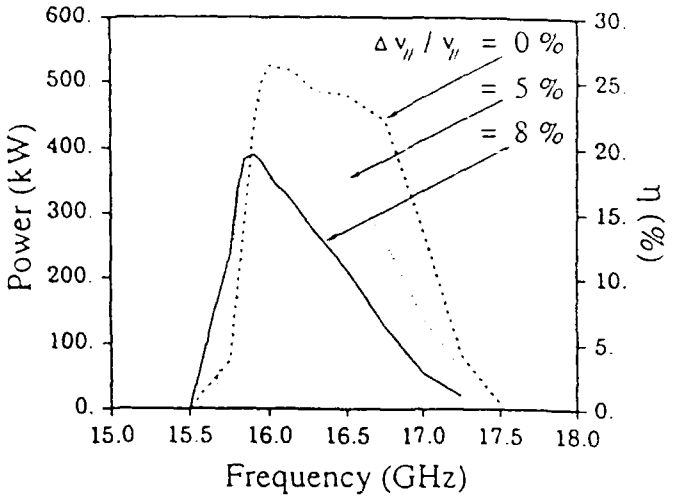

Figure 10: Constant-drive bandwidth of proposed three-stage $TE_{21}^{(2)}$ gyro-TWT (Table I) for axial velocity spreads of 0% (dashed curve), 3%(dotted curve) and 5% (solid curve) with input power of 0.21 W, 0.55 W and 1.9 W, respectively.

Although the interaction length has been reduced to 80% of the $TE_{41}^{(4)}$ gyro-BWO threshold length, the gain of the single-stage device is still appreciable for such a high power amplifier.

The 100 kV, 20 A beam with α = 1 will be emitted, as shown in Fig. 11, from the curved cathode surface of the single anode MIG described in Table III. It is predicted by the EGUN code to yield $\Delta v_z/v_z$ = 8% and is being built by NTHU. The MIG beam will be compressed adiabatically into the interaction region where a magnetic field with ± 0.25% uniformity over 1 m is provided by a 4 kG, liquid cooled, aluminum foil-wound solenoid. Using HP's high frequency structure simulator, a two-mode axial phase velocity coupler has been modeled and simulated. The rf input coupler shown in Fig. 12 will couple a rectangular waveguide's TE_{10} mode to a circular guide's TE_{21} mode with 0 dB coupling over a 20 % bandwidth [11]. The predicted bandwidth of the input coupler is shown in Fig. 13. The high power TE_{21} output wave from the amplifier will be converted into the more useful TE_{11} mode in the 12 cm length, two-period beat wave converter [11, 12, 13] shown in Fig. 14 with a predicted 0.5 dB bandwidth of 10 % and a conversion efficiency of 99.5 % at 16.1 GHz. The TE_{21}/TE_{11} mode converter design resulted from our collaboration with Dr. J. Pretterebner of Stuttgart University. The predicted performance of the converter is shown in Fig. 15.

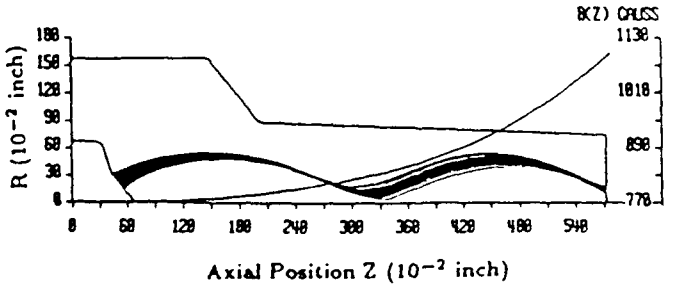

Figure 11: Trajectories of electrons emitted from the 100 kV, 20 A single anode MIG. The electrode and magnetic field profile are also shown.

Table III : Single Anode MIG Design

Beam Voltage	100 kV
Beam Current	20 A
$\alpha = v_\perp / v_\parallel$	1.0
Cathode Loading	9.7 A / cm^2
Cathode Radius	0.57 cm
Cathode Angle	52°
Radius of Cathode Curvature	4.06 cm
Emitting Strip Length	0.58 cm
Cathode to Anode Distance	4.1 cm
Magnetic Compression Ratio	3.8
$\Delta v_\parallel / v_\parallel$	8 %

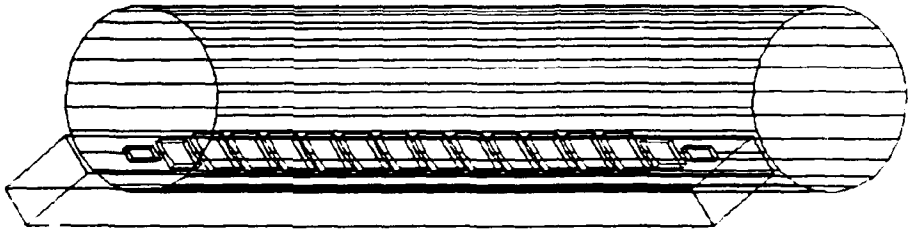

Figure 12: Schematic of $TE_{10}^{\square}$ to TE_{21}° mode rf input directional coupler.

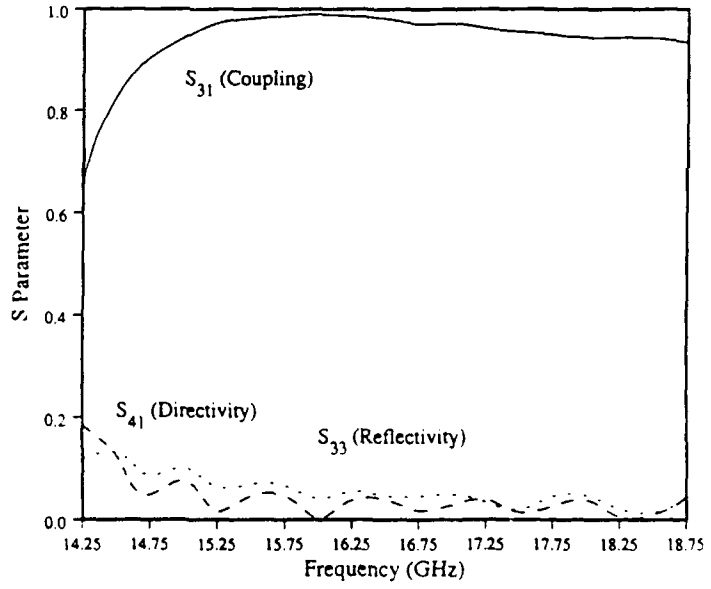

Figure 13: Bandwidth of S-parameters from HFSS for TE $^{\square}_{10}$ to TE_{21}° mode input directional coupler.

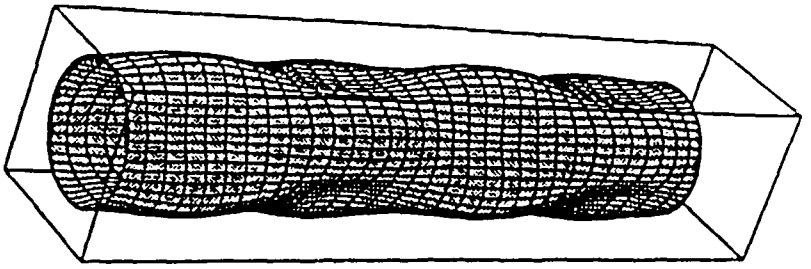

Figure 14: Schematic of output wave TE_{21} to TE_{11} mode beat-wave converter.

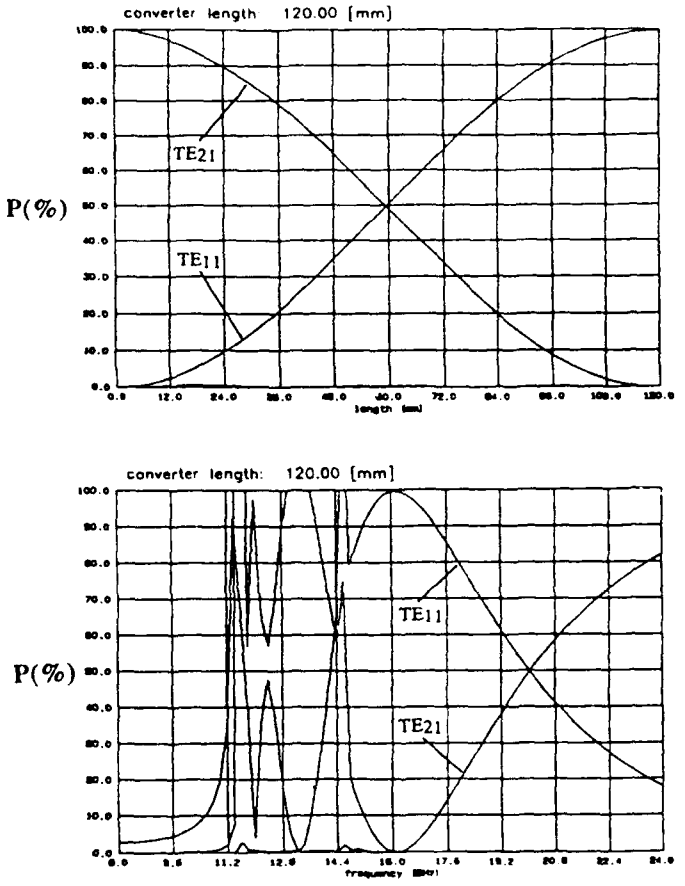

Figure 15: Mode distribution of wave energy in TE_{21}/TE_{11} mode converter for TE_{21} input as a function of (a) axial position for 16.3 GHz wave and (b) frequency.

D. High Power Harmonic CARMs

Summary

The interaction strength of an nth harmonic TE_{n1} CARM amplifier with an axis-encircling electron beam can be significantly enhanced by reducing the magnetic field to achieve a grazing intersection of the cyclotron-resonance line with the waveguide mode and thereby increasing the electron Larmor radius towards the wall radius where the fields are stronger. A grazing intersection also considerably relaxes the requirements on beam quality. We have performed preliminary investigations of a third-harmonic TE_{31} CARM-TWT amplifier which could be driven by our 350 kV electron gun and modulator.

CARMs [14, 15, 16, 17, 18] can generate very short wavelength emission much more readily than gyrotrons. Due to the large axial velocity of the electrons, the output wave is Doppler-upshifted by the factor $2\gamma_{\parallel}^2$ as in a FEL. For example, a 500 kV, 10 A CARM in a 60 kG magnetic field can be expected to produce 1 MW at 500 GHz. Harmonic interaction results in a further reduction of the magnetic field by a factor of the harmonic number. CARMs can handle extremely high power because the attenuation is weak since they are operated far above the cutoff. A similar voltage gyrotron operating at 500 GHz would require a magnetic field of $\simeq$ 350 kG and would be limited to much lower power levels. Another feature of CARMs is that they can be extremely efficient due to the autoresonance, where the electrons stay in resonance with the wave even as they lose energy to it due to the compensation between the two terms in the resonance condition. The change is the relativistic cyclotron frequency is compensated by the change in the Doppler-shift. The proof-of-principle experiment [19] that we performed in collaboration with LLNL produced megawatt power levels up to 270 GHz. We are proposing in our ARO basic studies to carefully provide the detailed physics basis for the next generation of devices since experiments to date have not yet satisfied this need.

We have investigated the advantage of a third-harmonic, multi-section CARM-TWT amplifier driven by a high voltage, low current axis-encircling electron beam (350 kV, 2 A). The axis-encircling beam will be produced by passing a pencil beam through a gyroresonant wiggler. The beam will emerge from the wiggler with a modest velocity ratio ($v_\perp/v_z = \alpha$) of 0.5 and a considerable $\gamma_z = (1 - v_z/c)^{-1/2}$ of 1.44. The resulting large value of γ_z will be used to give a substantial enhancement of the coupling strength for the harmonic interaction. For an n-th harmonic interaction, the coupling constant is proportional to [20]

$$H_n = \left[J_n'(q_{n1} r_L / r_w)\right]^2$$

where r_L and r_w are the Larmor and cavity radii, respectively, and q_{n1} is the first zero of $J_n'(x)$. Our ARO-funded high-harmonic gyro-devices with axis-encircling beams that were developed over the last ten years have been based on this coupling constant. By using the equations of motion ($v_\perp = r_L \Omega_c$), the equation for the cutoff frequency ($\omega_c = q_{n1} c / r_w$), and the condition for grazing intersection of the n-th harmonic cyclotron resonance line with the waveguide mode ($\omega_c = \gamma_z n \Omega_c$), the above coupling constant can be written as

$$H_n = \left[J_n'(\gamma_z n \beta_\perp)\right]^2$$

where $\beta_\perp$ is the electrons' transverse velocity normalized to the speed of light. The dependence of H_n on $\beta_\perp$ for a third harmonic CARM-TWT is shown in Fig. 16(a) for several values of γ_z. For our proposed experiment with $\gamma_z = 1.44$ and $\beta_\perp = 0.36$, it can be seen that the interaction strength increases by a factor of four compared to the unenhanced case of $\gamma_z = 1$. For these parameters, the interaction constant is sufficiently strong to yield a high gain, efficient amplifier.

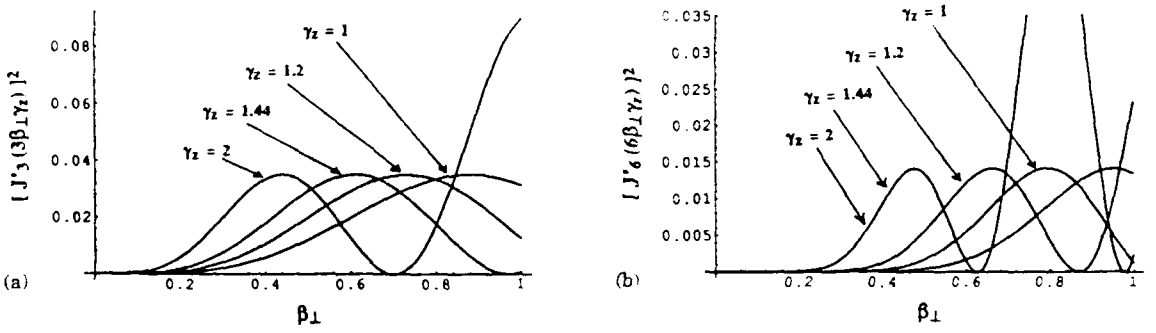

Figure 16: Dependence of (a) third-harmonic interaction strength H_3 and (b) sixth-harmonic interaction strength H_6 on normalized transverse velocity $\beta_\perp = v_\perp/c$ for four values of axial Lorentz factor $\gamma_{||} = (1 - \beta_{||}^2)^{-1/2}$ ($\gamma_{||} = 1$, 1.2, 1.44 and 2.0).

The marginal stability design procedure, which was recently developed and published by our group in collaboration with Drs. A.T. Lin and K.R. Chu for creating stable, high performance gyro-TWTs [4] can be used to design the CARM-TWT circuit. In this design procedure, the amplifier is comprised of several interaction sections separated by attenuating severs and each with a length shorter than the start-oscillation length for the most prevalent oscillation mode, which is usually a gyro-BWO interaction. The circuit will be designed for a 350 kV, 2 A electron beam with an α of 0.5 by finding the start-oscillation length for all the possible modes and then setting the length for the interaction sections to be $\sim 10\%$ less than this. The desired gain for the amplifier determines the number of interaction sections needed. The cylindrical waveguide circuit will be sliced axially with three cuts separated by 120° in azimuth to suppress all modes except those with a threefold azimuthal symmetry. Figure 16(b) shows the coupling constant for the strongest surviving mode, the TE_{61} mode. Since the value of H_6 is smaller than for our design mode by a factor of ten, we can expect significant gain for the relatively long interaction length available.

A CARM's desirable features of high efficiency, high power, and large output frequency to rest-mass gyrofrequency ratio can be attained only if the electron beam's axial velocity-spread can be kept low ($\Delta v_z/v_z \leq 2\%$), which is difficult to achieve for a high current beam with the requisite transverse velocity. We have investigated gyroresonant wigglers [21] for the production of low velocity-spread helical beams. Using a PIC simulation code, we found that a near-optimized gyroresonant wiggler designed for a final α of 0.6 resulted in an axial velocity ratio of 6.5% for a 150 A beam as shown in Fig. 17 and 4% for 20 A. Emittance growth is due to the space-charge of the non-axisymmetric helical-shaped beam. These numbers were found using a self-consistent beam simulation code which includes space-

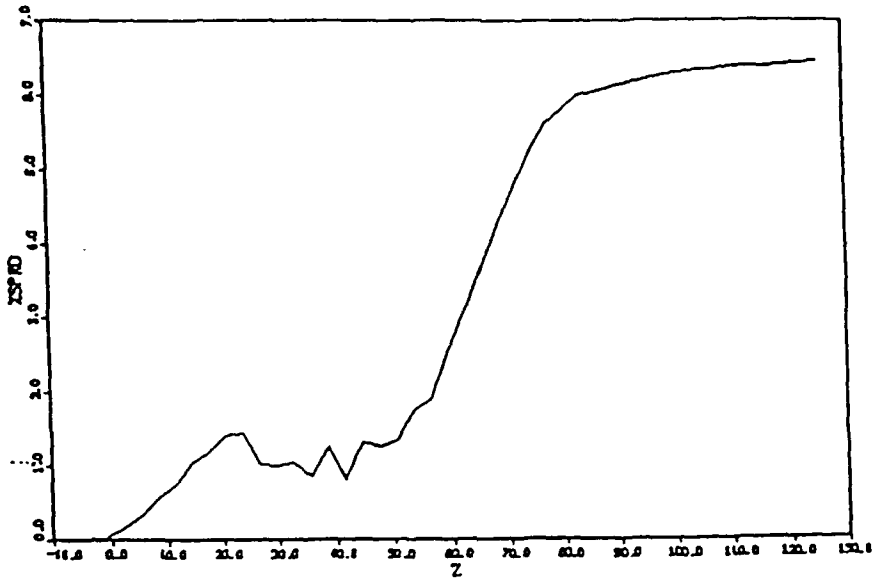

Figure 17: Spatial growth of axial velocity-spread due to gyroresonant wiggler at z = 0 cm to z = 40 cm (250 kV; 150A; beam radius = 1 cm; wall radius = 2 cm; wiggler period = 8 cm; relative wiggler amplitude, B_w/B_o = 0.02).

charge and which was provided to us by our collaborator Dr. M. Caplan of LLNL. This code will be used to design the wiggler for the proposed experiment. We expect to be able to achieve an axial velocity spread better than 2% for our 2 A beam. In addition, since the initial experiment will be performed with a grazing intersection, the beam velocity-spread requirements are considerably relaxed.

The parameters of a our proof-of-principle experiment are given in Table IV. It will utilize equipment available in our laboratory. Our high voltage SLAC 5045 Klystron gun driven by our SLAC-style 400/800 kV modulator will create the initial pencil beam. The experiment will be performed in our 3 kG, 2 m long, 20 cm bore copper solenoid. The vacuum system is currently operating in the 10^{-8} Torr range.

Table IV. Parameters of 33 GHz third-harmonic sliced TE_{31} CARM-TWT

Voltage	350 kV
Current	2A
$\alpha = v_\perp/v_\parallel$	0.5
Power	140 kW
Efficiency	20%
Magnetic Field	3.3 kG
Guiding Center Radius, r_{gc}	0
Wall Radius, r_w	0.88 cm
Larmor Radius, r_L	0.32 cm
Wiggler Period	4.5 cm
Initial Beam Radius	0.6 mm

E. High Performance Gyro-Klystron

Summary

The objective of this work is to investigate the basic physics issues associated with the design and operation of a high performance millimeter-wave gyroklystron amplifier. Our approach is to begin by improving the performance of Varian's pioneering 28 GHz gyroklystron by employing our physics design. A state-of-the-art self-consistent nonlinear simulation code to design the amplifier was provided to us by our colleague Dr. K.R. Chu. Using the simulation code, a 250 kW, 33 GHz gyro-klystron with an efficiency of 39% and saturated gain of 52 dB has been designed for an 80 kV, 8 A electron beam with $\alpha = 1.5$ and an axial velocity spread of 7%. A superconducting solenoid appropriate for the experiment was donated by Hughes EDD and several 28 GHz gyrotron MIG electron guns were donated by Varian Associates.

Our initial work on the ARO program has been on the development of high performance, high power millimeter-wave fundamental-frequency gyro-klystrons. However, it is envisioned that our research will soon lead to the development of high-harmonic gyro-klystrons using high power MIG electron beams. Whereas our previous fifth-harmonic [22] gyro-klystron used a more moderate power, gyroresonantly rf-accelerated axis-encircling electron beam and generated 0.5 kW, our future harmonic gyro-klystrons will be at the 100 kW output power level. Harmonic operation allows the magnetic field to be reduced by the harmonic number. A third-harmonic, 100 GHz gyro-klystron would require a magnetic field of only 14 kG. Because a gyro-klystron's cavities are fairly short in order to avoid oscillation, operation of a harmonic gyro-klystron is much more straightforward than operation of a harmonic gyrotron. We therefore are confident that 200 GHz gyroklystrons could be readily developed and have this as our long term aim.

A self-consistent computer [23] code written by Professor K.R. Chu and used both for the University of Maryland's high power gyroklystron and our large-orbit gyro-klystron was employed to optimize parameters for our first gyro-klystron, which is intended to be a significant extension of Varian Associates' pioneering 28 GHz gyroklystron [24]. The code allows for beam loading of the cavities, beam velocity spread and radial guiding center spread. Additionally, the user may choose the analysis for each cavity to be either linear or nonlinear. The code was used successfully in predicting the results of the University of Maryland's gyroklystron and our ARO-funded fifth harmonic, large-orbit gyroklystron. The code was also tested against Varian's earlier results with good agreement. Varian designed a two-cavity 28 GHz gyroklystron for ECH applications with a circular TE_{01} input cavity, a circular TE_{02} output cavity and an $\alpha \equiv v_\perp / v_\parallel = 2$. Severe oscillation problems were encountered, but after some redesign, an output power of 50 kW was obtained. The efficiency remained under 10%. Figure 18 shows the nonlinear gain predicted by the above mentioned nonlinear code for the original Varian experimental device for varying the output cavity Q, which allows us to determine the peak efficiency by searching for the electric field amplitude which gives optimum energy extraction. Figure 19 shows the dependence of nonlinear gain on the beam's axial velocity spread. It is evident that the efficiency for this design is highly dependent on the velocity spread. This explains why the Varian device displayed a rather poor efficiency.

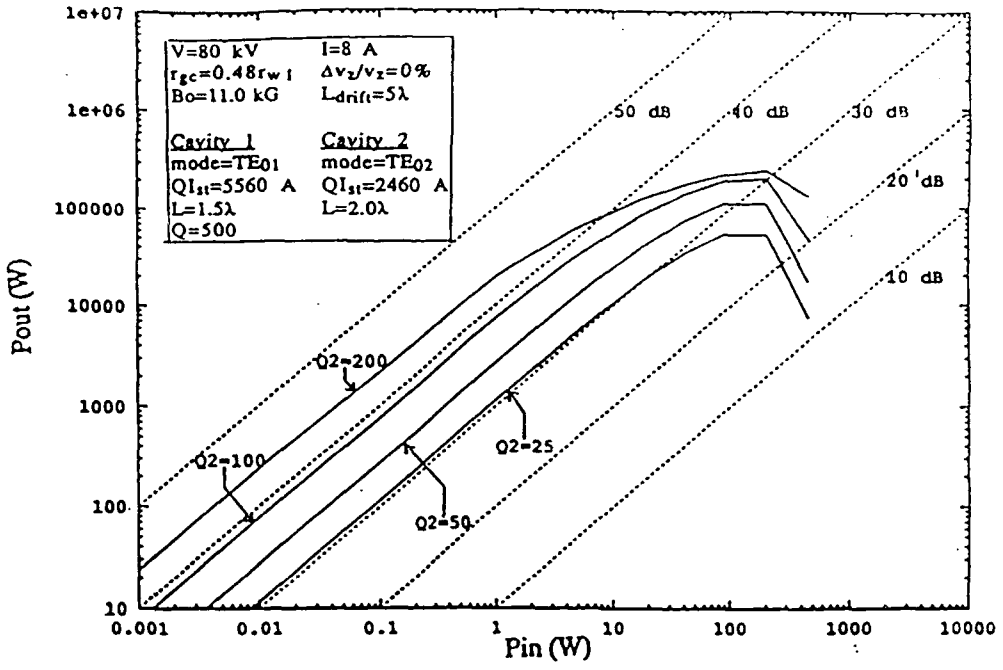

Figure 18: Gain characteristics of Varian two-cavity gyro-klystron for several values of output cavity Q.

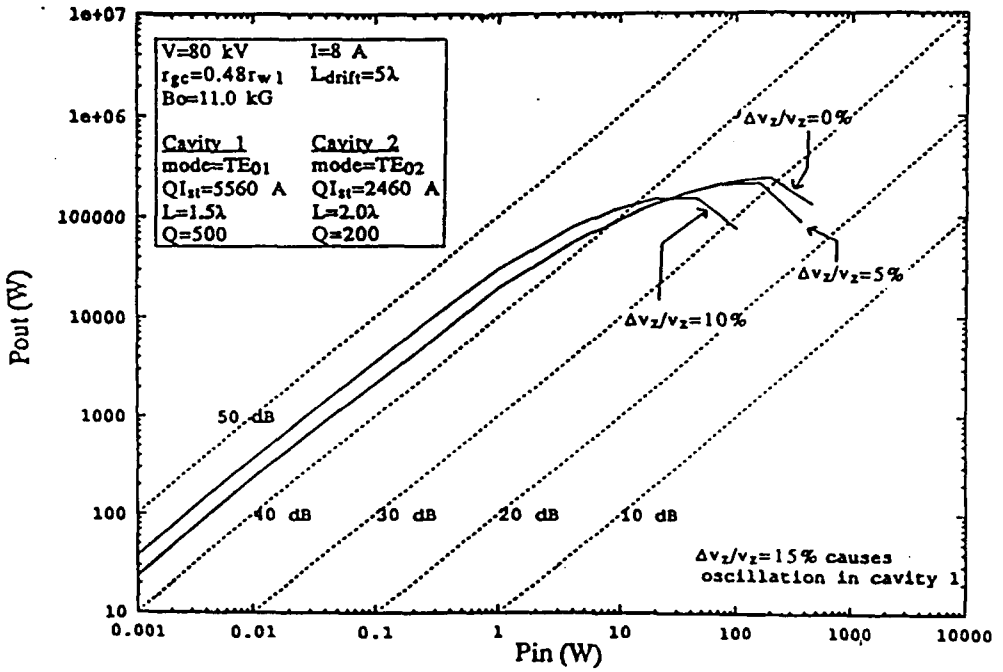

Figure 19: Gain characteristics of Varian two-cavity gyro-klystron for several values of axial velocity spread.

The purpose of our new experiment is to improve Varian's earlier gyroklystron and produce a high power, high performance amplifier. An additional buncher cavity has been added to increase gain and the design was completed with a lower α for better stability. The drift tubes will be loaded with a thin ceramic tube with a lossy inner coating as used for the absorbing sever in a recent successful gyro-TWT experiment [25]. The frequency has been increased to 33.2 GHz and the magnetic field was optimized for the new frequency.

The operating parameters of the new design along with simulation results can be seen in Table V. For an ideal beam, the code predicts an optimum output power of 300 kW, 51 dB saturated gain and 46% efficiency. Using a more realistic axial velocity spread of 7%, the predicted results are an output power of 250 kW with an efficiency of 39% and a saturated gain of 49 dB. Figure 20 shows the predicted linear and nonlinear gain characteristics for several values of velocity spread. It can be seen that the device will saturate for an input power of approximately 6 W.

Table V. Parameters of High Performance, Fundamental Three-Cavity Gyro-Klystron Amplifier

Voltage	80 kV
Current	8 A
Frequency	33.2 GHz
Magnetic Field	13 kG
$\alpha = v_\perp / v_\parallel$	1.5
$\Delta v_z / v_z$	7%
r_{gc} / r_w	0.48
Mode (#1, #2, #3)	TE_{01}, TE_{01}, TE_{02}
Q (#1, #2, #3)	300, 300, 550
L_{cavity} (#1, #2, #3)	2λ, 2λ, 2λ
$L_{\text{drift-tube}}$ (#1, #2)	3λ, 3λ
Circuit Length	10.8 cm
Simulation Results:	
Power	250 kW
Efficiency	39%
Gain (Saturated)	52 dB

The electron beam will be produced by a 28 GHz gyrotron MIG donated by Varian Associates. A 32.9-33.5 GHz tunable, 50 kW magnetron will initially provide the input signal. Eventually, this will be replaced by a 10 W helix TWT Ka-band amplifier. A seven-coil superconducting solenoid with a 12 cm uniform region donated by Hughes Aircraft Co. will be used to generate the 12.4 kG field necessary in the interaction region. All three cavities are 2λ long and are connected by 3λ long drift tubes. The driver and buncher

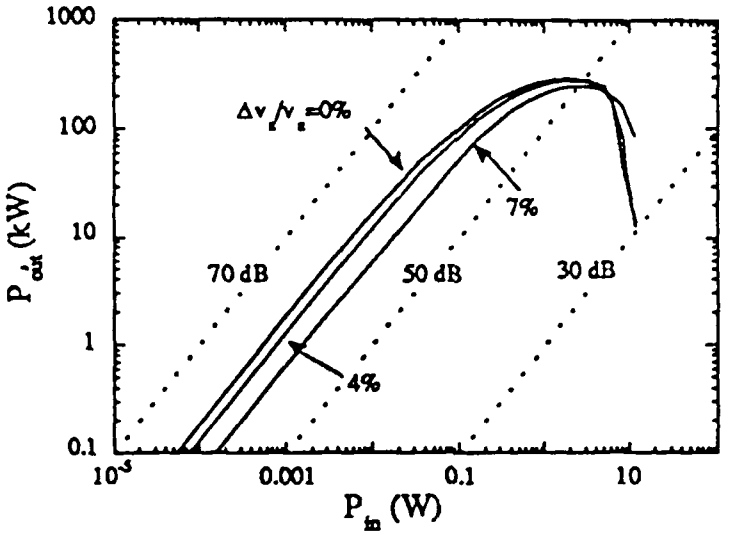

Figure 20: Gain characteristics of UCLA three-cavity gyro-klystron amplifier described in Table V for several values of axial velocity spread.

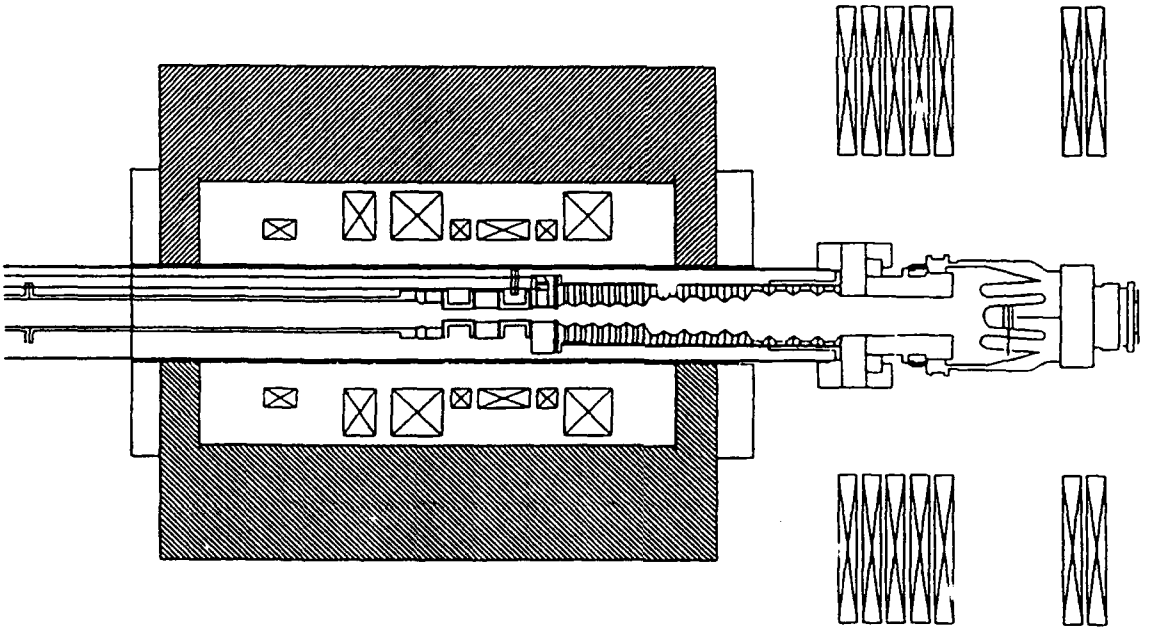

Figure 21: CAD layout of gyroklystron circuit within its vacuum chamber and superconducting solenoid dewar.

cavity will operate in the TE_{01} mode and the output cavity operates in the TE_{02} mode so as to allow cw operation. The circuit layout has been completed using a CAD program. The full drawing is shown in Fig. 21.

The diffraction coupled output cavity was designed using a computer code written by Professor K.R. Chu for the UCLA ATRI program [26]. Given the physical dimensions of the cavity and the TE_{mnl} mode in which the cavity is to operate in, the code predicts the field distribution in the cavity, the cavity's Q, and the resonant frequency. The code works for any arbitrarily shaped cylindrical cavity of slowly varying cross-section. The cavity must be closed at one end (the cross-section must be smaller than the cut-off cross-section), and can be either open or closed at the other end. The code can also account for wall loss in the cavity. As in the Varian Associates experiment, it was decided to design the cavity for TE_{021} operation with a length of 2λ. The cavity was designed to have a Q of 550 and an operating frequency of 33.2 GHz as specified by the gyroklystron simulation code. The profile of the output cavity is shown in Fig. 22(a) and Fig. 22(b) shows the resultant electromagnetic profile of the cavity's TE_{021} mode.

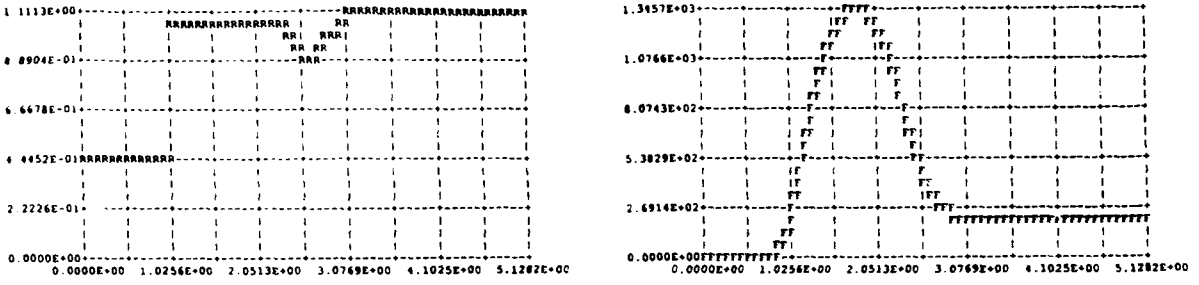

Figure 22: (a) Dependence of inner wall radius on axial distance for gyroklystron diffraction-coupled output cavity and (b) axial profile of gyroklystron output cavity's TE_{021} mode including emitted wave.

To prevent oscillation from occurring in the beam compression region, lossy MgO-SiC rings have been ordered and received. To keep the drift-tubes between the gyroklystron cavities from oscillating, we will use a technique successfully demonstrated in a recent gyro-TWT experiment [25]. An excellent attenuator can be achieved with a thin dielectric tube coated with graphite on the inside wall. In addition, the input and gain cavities must also be loaded with lossy rings in order to achieve the correct value of Q in the normally high-Q TE_{01} cavities. Two options are available for this. Because carbon impregnated aluminum silicate rings [27] have the advantage that the turn-around time can be relatively quick, we have devoted considerable effort to develop this technique. The other option is to again use lossy carbon coated dielectric tubes for this application too.

The magnetic field required for the MIG electron gun will be produced by copper solenoids external to the superconductor's dewar. The profile has been designed to conform to the magnetic field profile of the Varian gyrotron. Our magnetic field profile is

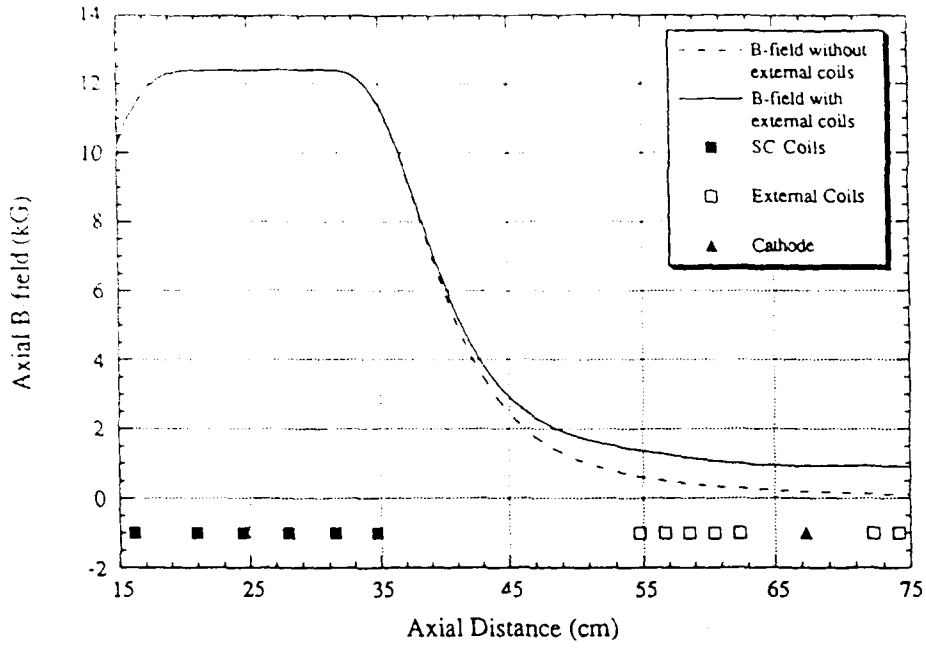

Figure 23: Gyro-klystron's magnetic field profile on axis with and without external gun coils activated. The positions of the superconducting and external coils are shown as well as the cathode location.

shown in Fig. 23. The solenoids are currently being mounted to the superconducting dewar. The vacuum chamber and pumps have been assembled and produce a vacuum in the 10^{-8} range. Also, we have constructed a modulator to drive the 50 kW, 33.2 GHz tunable magnetron that will serve as the initial input source for the gyroklystron amplifier. A high voltage power supply, thyratron and pulse transformer were assembled and a 40 Ω distributed transmission line was built and tested. The magnetron was driven to its full 50 kW output power. Directional couplers and attenuators are available to reduce the power to the required drive level.

Penultimate cavity detuning [28, 29] has also been investigated. Similar to the linear klystron, a gyroklystron's efficiency may be enhanced by properly mistuning the bunching cavities so as to increase the electron bunching. In the gyroklystron, it is desirable to have the leading phase electrons accelerated and lagging phase electrons decelerated. This can be accomplished by detuning the cavity frequency downward. It can be seen in Fig. 24 that for zero velocity spread, significant enhancement of the efficiency is predicted, but at the expense of gain. This loss in gain could be compensated by the addition of more bunching cavities. However, when a more realistic velocity spread of 7% was included, simulation showed that the increase in efficiency was negligible and the gain was still greatly reduced. For this reason, detuning of the penultimate cavity in our three-cavity gyro-klystron is not planned.

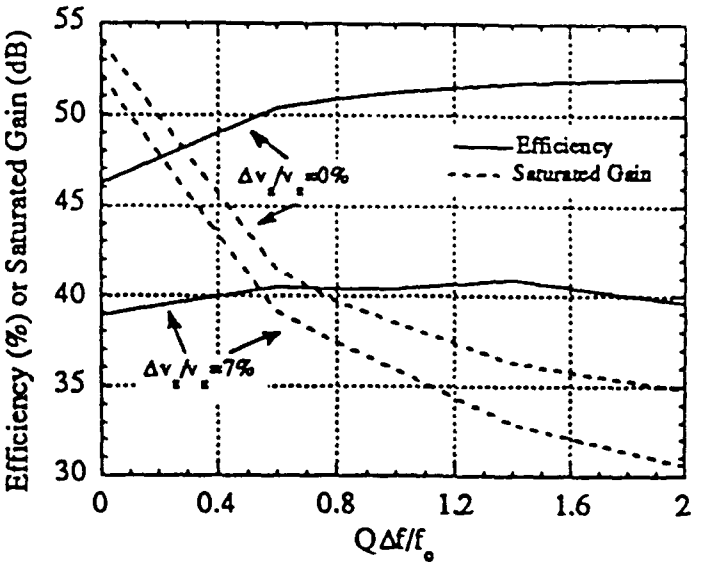

Figure 24: Efficiency and saturated gain of UCLA gyro-klystron as a function of penultimate cavity detuning for two value of axial velocity spread ($\Delta v_{\|}/v_{\|}$ = 0% and 7%).

References

[1] C.S. Kou, D.B. McDermott, N.C. Luhmann, Jr., and K.R. Chu, "Prebunched High-Harmonic Gyrotron", *IEEE Trans. on Plasma Science*, 18, 343, 1990.

[2] D.B. McDermott, D.S. Furuno and N.C. Luhmann, Jr., "Production of Relativistic, Rotating Electron Beam by Gyroresonant RF Acceleration in a TE_{111} Cavity", *J. Appl. Phys.*, 58, 4501, (1985).

[3] K.R. Chu, M.E. Read, A.K. Ganguly, "Methods of Efficiency Enhancement and Scaling for the Gyrotron Oscillator", *IEEE Trans. on Microwave and Techniques*, 28, 318-325, 1980.

[4] A.T. Lin, K.R. Chu, C.C. Lin, C.S. Kou, D.B. McDermott and N.C. Luhmann, Jr. , "Marginal Stability Design Criterion for Gyro-TWTs and Comparison of Fundamental with Second Harmonic Operation", *Int. J. Electronics*, 5, 873, 1992.

[5] L.R. Barnett, K.R. Chu, J.M. Baird, V.L. Granatstein, and A.T. Drobot, "Gain, Saturation and Bandwidth Measurements of the NRL Gyrotron Traveling Wave Amplifier", *Tech. Digest of IEEE Int. Electron Devices Meeting*, page 164, 1979.

[6] Q.S. Wang, C.S. Kou, D.B. McDermott, A.T. Lin, K.R. Chu, and N.C. Luhmann, Jr., "High-Power Harmonic Gyro-TWTs-Part II: Nonlinear Theory and Design", *IEEE Trans. on Plasma Science*, 20, 163, 1992.

[7] D.S. Furuno, D.B. McDermott, C.S. Kou, N.C. Luhmann, Jr., and P. Vitello, "Theoretical and Experimental Investigation of High Harmonic Gyro-Travelling-Wave-Tube Amplifier", *Phys. Rev. Lett.*, 62, 1314-1317, 1989.

[8] C.S. Kou, Q.S. Wang, D.B. McDermott, A.T. Lin, K.R Chu, and N.C. Luhmann, Jr., "High Power Harmonic Gyro-TWTs: I Linear Theory and Oscillation Study", *IEEE Trans. on Plasma Science*, 20, 155, 1992.

[9] A.K. Ganguly and S. Ahn, "Self-Consistent Large Signal Theory of the Gyrotron Travelling Wave Amplifier", *Int. Journal Electronics*, 53, 641, 1982.

[10] D.B. McDermott, N.C. Luhmann, Jr., D.S. Furuno, A. Kupiszewski and H.R. Jory, "Operation of a Millimeter-Wave Harmonic Gyrotron", *Int. J. Infrared and Millimeter Waves*, 4, 639, 1983.

[11] Q.S. Wang, D.B. McDermott, C.S. Kou, A.T. Lin, K.R. Chu, N.C. Luhmann, Jr., and J. Pretterbner, "High-Power Second-Harmonic Gyro-TWT Amplifier", *1992 IEEE Int. Electron Devices Meeting*, 1992.

[12] M. Thumm, "High-Power Millimeter-Wave Mode Converters in Overmoded Circular Waveguides Using Periodic Wall Perturbations", *Int. J. Electronics*, 57, 1225, (1984).

[13] C.F. Kinney, "High Power Mode Converters", *UCLA M.S. Thesis*, 1992.

[14] V.L. Bratman, G.G. Denisov, N.S. Ginzburg, and M.I. Petelin, *IEEE J. Quantum Electronics*, QE-19, 282, (1983).

[15] K.R. Chu and A.T. Lin, "Gain and Bandwidth of the Gyro-TWT and CARM Amplifiers", *IEEE Trans. on Plasma Science*, 16, 90, 1988.

[16] Q.S. Wang, C.S. Kou, K.C. Leou, C.K. Chong, D.B. McDermott, A.T. Lin, N.C. Luhmann, Jr., M. Caplan, A. Salop, B. Kulke and K.R. Chu, "Cyclotron Autoresonance Maser Amplifiers and Oscillators", *Digest of Int. Electron Devices Meeting*, page 759, (1989).

[17] G. Bekefi, A. DiRienzo, C. Leibovitch and B.G. Danly, "35 GHz Cyclotron Autoresonance Maser Amplifier", *Appl. Phys. Lett.*, 54, 1302, 1989.

[18] Q.S. Wang, D.B. McDermott, A.T. Lin, N.C. Luhmann, Jr., K.R. Chu, A. Salop and M. Caplan, "CARM Amplifier Designs for High Power", *Int. J. IR & mm-Waves*, 12, 297, (1991).

[19] M. Caplan, B. Kulke, G.A. Westenskow, D.B. McDermott, and N.C. Luhmann, Jr., "Induction-Linac-Driven Millimeter-Wave CARM-Oscillator", *LLNL Explorary Research and Development Report*, page 144, 1990.

[20] K.R. Chu, "Theory of Electron Cyclotron Maser Interaction in a Cavity at the Harmonic Frequencies", *Phys. Fluids*, 21, 2354, 1978.

[21] P. Ferguson and R. Symons, "C-Band Gyro-TWT", *IEEE Int. Electron Devices Meeting*, page 310, 1980.

[22] D.S. Furuno, D.B. McDermott, N.C. Luhmann, Jr., P. Vitello and K. Ko, "Operation of a Large-Orbit High-Harmonic Multicavity Gyroklystron Amplifier", *IEEE Trans. on Plasma Science*, 16, 155, 1988.

[23] K.R. Chu, V.L. Granatstein, P.E. Latham, W. Lawson, and C.D. Striffler, "30 MW Gyro-Klystron-Amplifier Design for High-Energy Linear Accelerators", *IEEE Trans. Plasma Science*, 13, 424, 1985.

[24] H.R. Jory, F. Friedlander, S.J. Hegji, J.F. Shively and R.S. Symons, "Gyrotrons for High Power Millimeter Wave Generation", *Digest of Int. Electron Devices Meeting*, page 234, 1977.

[25] K.R. Chu, L.R. Barnett, W.K. Lau, L.H. Chang and C.S. Kou, "Recent Developments in Millimeter Wave Gyro-TWT Research at NTHU", *IEEE Int. Electron Devices Meeting Technical Digest*, page 699, 1990.

[26] K.R. Chu, "Time Domain Analysis of Open Cavities", *submitted to IEEE Trans. on Microwave Theory & Tech.*, 1992.

[27] J.P. Calame and W. Lawson, "A Modified Method for Producing Carbon Loaded Vacuum Compatible Microwave Absorbers from a Porous Ceramic", *submitted for publication*, 1992.

[28] K.R. Chu, P.E. Latham and V.L. Granatstein, "Penultimate Cavity Tuning of the Gyroklystron Amplifier", *Int. J. Electronics*, 65, 419, 1988.

[29] G.S. Park, V.L. Granatstein, S.Y. Park, C.M. Armstrong and A.K. Ganguly, "Experimental Study of Efficiency Optimization in a Three-Cavity Gyroklystron Amplifier", 20, 224, 1992.

V. PUBLICATIONS AND TECHNICAL REPORTS, 6/25/91 - 6/24/92

A.T. Lin, K.R. Chu, C.C. Lin, C.S. Kou, D.B. McDermott and N.C. Luhmann, Jr., "Marginal Stability Design Criterion for Gyro-TWT's and Comparison of Fundamental with Second Harmonic Operation," *Int. J. Electronics*, 72, 873 (1992).

C.K. Chong, D.B. McDermott, M.M. Razeghi, N.C. Luhmann, Jr., J. Pretterebner, D. Wagner, M. Thumm, M. Caplan and B. Kulke, "Bragg Reflectors," *IEEE Trans. on Plasma Science*, 3, 393 (1992).

C.S. Kou, Q.S. Wang, D.B. McDermott, A.T. Lin, K.R. Chu, and N.C. Luhmann, Jr., "High Power Harmonic Gyro-TWTs- Part I: Linear Theory and Oscillation Study," *IEEE Trans. on Plasma Science*, 3, 155 (1992).

Q.S. Wang, D.B. McDermott, C.S. Kou, A.T. Lin, K.R. Chu and N.C. Luhmann, Jr., "High-Power Harmonic Gyro-TWT's-Part II: Nonlinear Theory and Design," *IEEE Trans. on Plasma Science*, 3, 163 (1992).

Q.S. Wang, D.B. McDermott, C.S. Kou, A.T. Lin, K.R. Chu, N.C. Luhmann, Jr., and J. Pretterebner, "High-Power Second Harmonic Gyro-TWT Amplifier," *Technical Digest of 1992 Int. Electron Devices Meeting*, to be published.

Q.S. Wang, C.K. Chong, C.S. Kou, D.B. McDermott, N.C. Luhmann, Jr., A.T. Lin, K.R. Chu, "High Power, Harmonic Gyro-TWTs," *Digest of 1991 Int. Conf. on IR and mm-Waves*.

Q.S. Wang, C.S. Kou, D.B. McDermott, A.T. Lin, K.R. Chu and N.C. Luhmann, Jr., "High-Power Harmonic Gyro-TWT Design," *Proceedings of SPIE Conf. on Intense Microwave and Particle Beams*, Los Angeles, CA 1992.

J.D. McNally, M.P. Bobys, D.B. McDermott and N.C. Luhmann, Jr., "250 kW, 33.2 GHz Gyroklystron Amplifier Design," *Proceedings of SPIE Conf. on Intense Microwave and Particle Beams*, Los Angeles, CA 1992.

K.C. Leou, T.R. Stephenson, J.D. McNally, G. Vasilakos, G.D. Ramlow, M.P. Bobys, D.B. McDermott and N.C. Luhmann, Jr., "Fast-Wave Research at UCLA: Gyro-TWT, Gyro-BWO and Gyro-Klystron," *Digest of Microwave Power Tube Conference*, Monterey, CA 1992.

C.K. Chong, Q.S. Wang, C.S. Kou, T.L. Stewart, A.J. Balkcum, C.F. Kinney, D.B. McDermott, A.T. Lin, K.R. Chu and N.C. Luhmann, Jr., "Harmonic 35 GHz Gyro-TWT Amplifiers at UCLA," *Digest of Microwave Power Tube Conference*, Monterey, CA 1992.

Q.S. Wang, D.B. McDermott, N.C. Luhmann, Jr., A.T. Lin, C.S. Kou and K.R. Chu "Harmonic Gyro-TWT Amplifier for High Power," *Technical Digest of 9th Intl. Conf. on High Power Particle Beams*, Washington, D.C. 1992.

J.D. McNally, M.P. Bobys, D.B. McDermott and N.C. Luhmann, Jr., "High Performance 33.2 GHz Gyroklystron," *Technical Digest of 9th Intl. Conf. on High Power Particle Beams*, Washington, D.C. 1992.

Q.S. Wang, D.B. McDermott, A.T. Lin, N.C. Luhmann, Jr., and J. Pretterebner, "Single Stage High Power Second Harmonic Gyro-TWT," *Digest of 1992 Int. Conf. on IR and Millimeter Waves*, to be published.

J.D. McNally, M.P. Bobys, D.B. McDermott and N.C. Luhmann, Jr., "33.2 GHz, 3-Cavity Gyro-Klystron," *Digest of 1992 Int. Conf. on IR and Millimeter Waves*, to be published.

M.P. Bobys, J.D. McNally, D.B. McDermott, N.C. Luhmann, Jr., "High Efficiency Phase-Locked 60 GHz Gyro-Klystron Oscillator," *Bulletin of the American Physical Society*, **36**, 2392 (1991).

D.B. McDermott, C.K. Chong, N.C. Luhmann, Jr., M. Thumm, J. Pretterebner, "Bragg Reflectors with Hamming Window Taper," *Bulletin of the American Physical Society*, **36**, 2389 (1991).

Q.S. Wang, C.S. Kou, D.B. McDermott, N.C. Luhmann, Jr., A.T. Lin, K.R. Chu, "High Power, Second Harmonic Gyro-TWT," *Bulletin of the American Physical Society*, **36**, 2405 (1991).

Q.S. Wang, D.B. McDermott, A.T. Lin, N.C. Luhmann, Jr., and J. Pretterebner, "High Power, Second Harmonic TE_{21} Gyro-TWT," submitted to *1993 SPIE Conf. on Intense Microwave Pulses*.

Q.S. Wang, D.B. McDermott, A.T. Lin, and N.C. Luhmann, Jr. and J. Pretterebner, "High Power Harmonic Gyro-TWT," submitted to *1992 Conf. of APS Div. of Plasma Physics*.

J.D. McNally, M.P. Bobys, D.B. McDermott and N.C. Luhmann, Jr., "250 kW, 33.2 GHz Gyroklystron Amplifier," submitted to *1992 Conf. of APS Div. of Plasma Physics*.

A.J. Balkcum, K.C. Leou, D.B. McDermott and N.C. Luhmann, Jr., "High-Harmonic Pre-bunched Gyrotron/Magnicon," submitted to *1992 Conf. of APS Div. of Plasma Physics*.

VI. LIST OF SCIENTIFIC PERSONNEL

Professor N.C. Luhmann, Jr.
Dr. D.B. McDermott
Mr. C.S. Kou*
Mr. Q.S. Wang
Mr. A.J. Balkcum
Mr. M.P. Bobys
Mr. J.D. McNally

*Ph.D. was awarded to Chwung-Shan Kou

VII. INVENTION REPORT

None

A. APPENDIX

A.1. Marginal Stability Design Criterion for Gyro-TWTs and Comparison of Fundamental with Second Harmonic Operation

INT. J. ELECTRONICS, 1992, VOL. 72, NOS. 5 AND 6, 873–885

Marginal stability design criterion for gyro-TWTs and comparison of fundamental with second harmonic operation

A. T. LIN†, K. R. CHU†‡, C. C. LIN†, C. S. KOU§‖, D. B. McDERMOTT§ and N. C. LUHMANN JR§

Stability properties of both the fundamental and second harmonic gyrotron travelling wave amplifier (gyro-TWT) are examined with multi-mode particle simulations. The second harmonic cyclotron interaction with an axis-encircling electron beam is found to be more stable to oscillations and can yield significantly greater power than the fundamental harmonic gyro-TWT. A multiple stage interaction structure based on a marginal stability criterion is proposed and illustrated with examples of a 128 kW fundamental gyro-TWT and a 532 kW second harmonic gyro-TWT. Stable amplification at much higher power levels is in principle possible.

1. Introduction

The gyrotron travelling wave amplifier has superior power handling capability compared to the conventional TWT because the gyro-TWT employs a fast wave interaction and a smooth wall geometry. In the millimetre-wave band, the demonstrated peak power (~25 kW) (Barnett *et al.* 1979, 1989, Granatstein *et al.* 1983, 1984, Chu *et al.* 1990 a) and bandwidth (Chu *et al.* 1990 a) (~10%) of gyro-TWTs are already comparable to those of state-of-the-art TWTs (see, for example, Butterworth and Wallace 1987). However, in these demonstrations of the fundamental harmonic gyro-TWT, a relatively large magnetic field (~12 kG for the Ka-band) was required. Also, the power levels achieved are still too low fully to realize the power handling capability of the gyro-TWT.

The strong beam-wave interaction at the fundamental cyclotron harmonic has been the cause of unwanted oscillations which limit the output power. There are various ways to increase the oscillation threshold, such as (i) lowering the beam α ($\equiv v_\perp/v_z$) to reduce the interaction strength, (ii) increasing the beam voltage to move away from the cut-off frequency of the operating mode, and (iii) employing a severed interaction waveguide. While all of these methods have proved effective in improving the stability and power, additional measures are required if still higher power is desired.

In this study, we investigate methods of stably operating the fundamental and harmonic gyro-TWT as a high power amplifier. Harmonic interaction is much

Received 23 June 1991; revised 19 September 1991.

†Department of Physics, University of California, Los Angeles, CA 90024, U.S.A.

‡Permanent address: Department of Physics, National Tsing Hua University, Hsinchu, Taiwan, Republic of China.

§Department of Electrical Engineering, University of California, Los Angeles, CA 90024, U.S.A.

‖Present address: Department of Physics, National Tsing Hua University, Hsinchu, Taiwan, Republic of China.

0020-7217/92 $3.00

weaker, but it offers the important advantage of a reduced magnetic field requirement. To compensate for the weaker interaction, one can introduce an azimuthally corrugated interaction structure (Lau and Barnett 1982, Chu and Dialetis 1985, Namkung 1984, Destler 1983) which ripples the RF field lines in a way to strengthen a specific harmonic field component. Alternatively, one can employ a large orbit concentric electron beam (hundreds of kilovolts) (Destler 1983, McDermott *et al.* 1983, Kou *et al.* 1990) with the electrons located in the vicinity of the peak field of an azimuthal mode. However, the brute-force remedy of increasing the electron beam current (as considered in this study) may be the most suitable for high power operation. It offers the dual merits of moderate voltage and smooth waveguide structure.

Our study is concerned with power levels well beyond the state of the art. Self-oscillations are inevitability present in such a regime. It is thus essential that a multi-mode analysis be employed to examine the physical behaviour of these modes. More importantly, means of stabilizing the unwanted oscillations must also be investigated so as to push upward the stability boundary and hence the power output.

The basic tools of the subsequent studies consist of an analytical linear theory (Chu and Lin 1988), a single-mode particle tracing code (Kou *et al.* 1991), and a multi-mode particle simulation code (Lin and Lin 1989), which complement and validate one another. The first two tools allow us to determine the parameters for optimum single-mode operation. The resultant stability properties are then examined by the multimode particle simulation code.

In §2, the simultaneous evolution of various oscillating modes are analysed in multi-mode simulation, which leads to the conclusion that the second harmonic gyro-TWT is generally more stable than the fundamental harmonic gyro-TWT. Based on these stability considerations, a procedure is developed in §3 for the design of a marginally stable gyro-TWT. It is found that, under the marginally stable operating condition, the second harmonic gyro-TWT produces significantly greater power than the fundamental harmonic gyro-TWT with comparable gain, bandwidth, and efficiency.

2. Self-oscillation in fundamental and second harmonic gyro-TWTs

Start-oscillation conditions for the forward (Chu and Lin 1988, Lau *et al.* 1981, Davies 1989) and backward (Park *et al.* 1984) waves in the gyro-TWT and cyclotron autoresonance maser amplifiers have been extensively studied in the literature. Theoretical calculations and experimental evidence all indicate that oscillation of one kind or another is the norm rather than exception in a high power gyro-TWT. In this section, we investigate the spontaneous growth of these oscillations and their saturated behaviour through particle simulations. To determine the appropriate parameters to use for the simulation, we have employed the linear theory (Chu and Lin 1988) and the single-mode particle tracing code (Kou *et al.* 1991) to arrive at the two cases shown in the Table. The electron beam in Case a is consistent with a magnetron injection gun (Baird and Lawson 1986), while Case b corresponds to a cusp electron gun (Scheitrum *et al.* 1989). Each case represents a compromise between stability, gain, power, bandwidth, and efficiency. Here, B_g is the magnetic field which results in a grazing intersection between the operating mode and the operating cyclotron harmonic resonance line. In Fig. 1, the operating mode is shown by the (near grazing) intersection of the two unbroken curves. Intersections that

occur for negative k_z are potential sources of oscillations. For Case b however, only the $s=m$ modes are unstable because the beam is assumed to be axis-encircling. Furthermore, all the possible oscillating modes have a harmonic number equal to or greater than the operating harmonic ($s=2$).

To emphasize and enhance the self-oscillations, we first perform the simulations in a relatively long (15 cm, unsevered) interaction waveguide in the absence of an input signal. Figure 2 shows the temporal behaviour of the TE^s_{mn} field amplitudes (superscript indicates the harmonic number of the interaction) from noise to saturation. There are three spontaneously growing modes for the case of fundamental harmonic interaction (Case a) with the operating mode being the dominant one at saturation. In contrast, only one spontaneously growing mode is present for the second harmonic interaction (Case b) despite a five-fold increase in beam current. It is also significant that the operating mode is stable with respect to the absolute instability in Case b. Comparison between Case a and Case b supports our earlier assertion that the harmonic interaction is a viable scheme for high power generation. This point will be further reinforced by efficiency and bandwidth considerations in the following section.

To quantify the effects of these oscillations, Figs 3 and 4 display, respectively, the electron momentum and energy distributions corresponding to the saturated state of Fig. 2. The beam quality is so degraded that no significant amplification can be expected to take place. As an illustration, Fig. 5(*a*) shows the temporal growth of a TE_{21} drive wave amplified by the spoiled beam described by Figs 3(*b*) and 4(*b*). Figure 5(*b*) shows the temporal growth of the same drive wave due to a good quality beam (see the Table, Case b) with the oscillating modes artificially suppressed (i.e. single-mode model). Comparison of Figs 5(*a*) and 5(*b*) dramatically demonstrates the deficiency of a single-mode treatment of high power gyro-TWTs.

3. Marginal stability design procedure for high power generation

The dominance of self-oscillations in the cases examined in the previous section suggests that measures must be taken to stabilize these oscillations in order for the gyro-TWT to function properly as an amplifier. There exists a tuning range for the magnetic field of at most a few percent for normal gyro-TWT operation. While this is a sufficient tuning range to stabilize the self-oscillation of the operating mode, it offers no remedy for other oscillating modes. Reducing the beam current can

	Case a	Case b
Waveguide radius (r_w)	0·26 cm	0·44 cm
Operating mode	TE_{11}	TE_{21}
Operating cyclotron harmonic (s)	1	2
Beam voltage (V_b)	100 kV	100 kV
Beam current (I_b)	5 A	25 A
Guiding centre position (r_c)	0·35 r_w	0
Electron velocity ratio $\alpha(v_{\perp 0}/v_{z0})$	1·0	1·0
Axial velocity spread ($\Delta v_z/v_{z0}$)	5%	5%
Magnetic field (B_0/B_g)	0·98	0·98

Parameters of the fundamental harmonic (Case a) and second harmonic gyro-TWT (Case b)

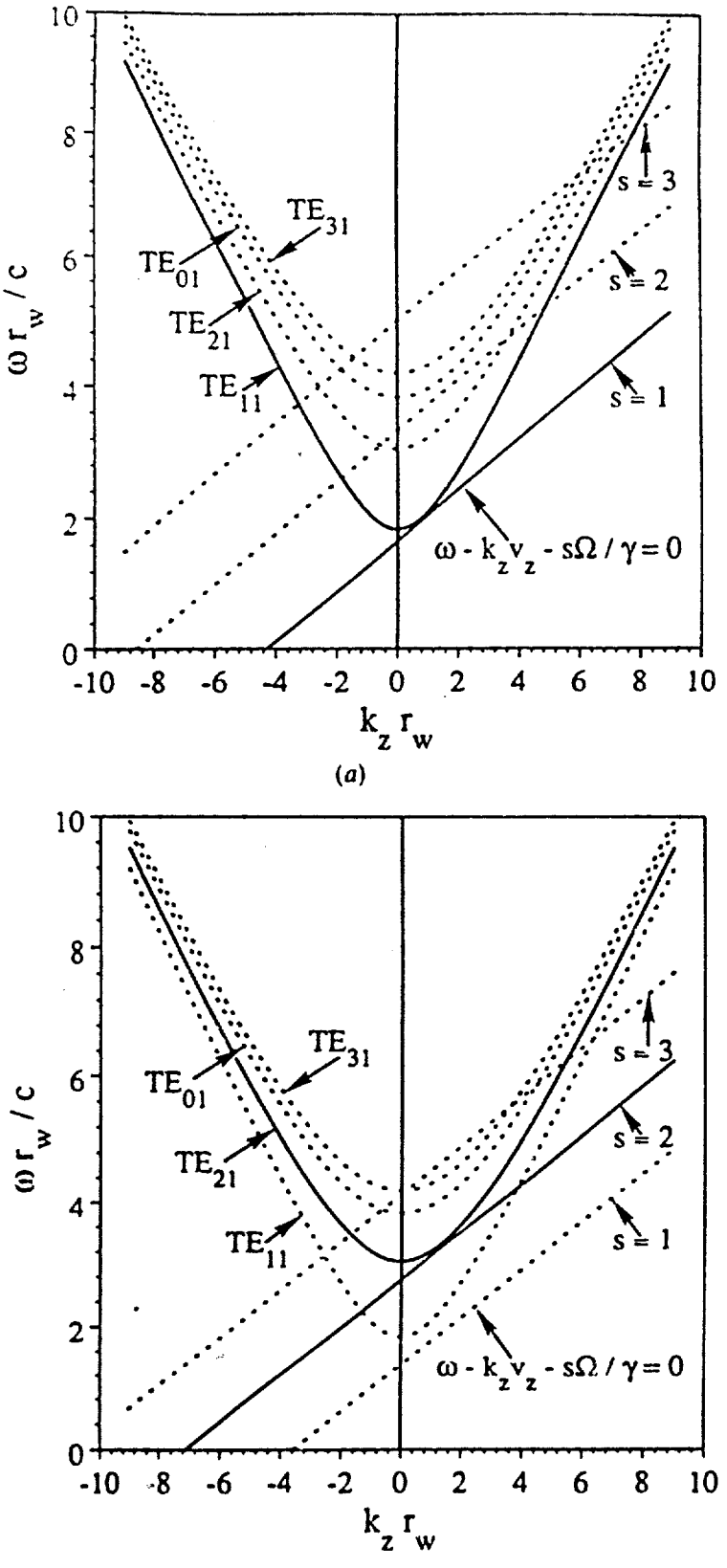

Figure 1. Uncoupled dispersion relation of operating mode (intersection of unbroken curves) and likely oscillating modes (intersections with negative k_z) for (*a*) Case a and (*b*) Case b of Table.

eventually stabilize all oscillations, but this is normally associated with reduced output power. The selective suppression of undesirable modes by special circuit design can be effective in some cases, but does not have universal applicability.

Because of the sensitivity of the oscillation threshold to the interaction length (Davies 1989), reducing the interaction length appears to offer a practical and effective means for oscillation stabilization. The resultant loss in gain can be recovered with a multi-stage interaction structure. Indeed, a recent severed gyro-

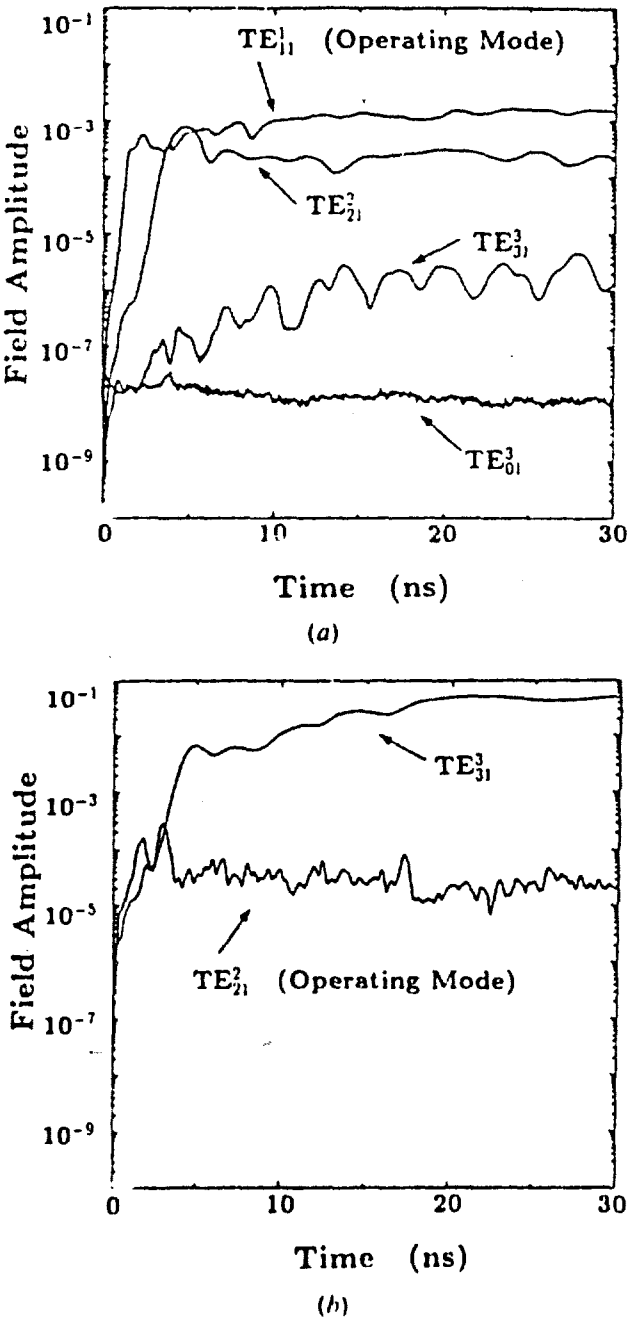

Figure 2. Field amplitudes of self-oscillating modes versus time in an unsevered interaction waveguide of 15cm in length for (*a*) Case a and (*b*) Case b (superscript indicates cyclotron harmonic number).

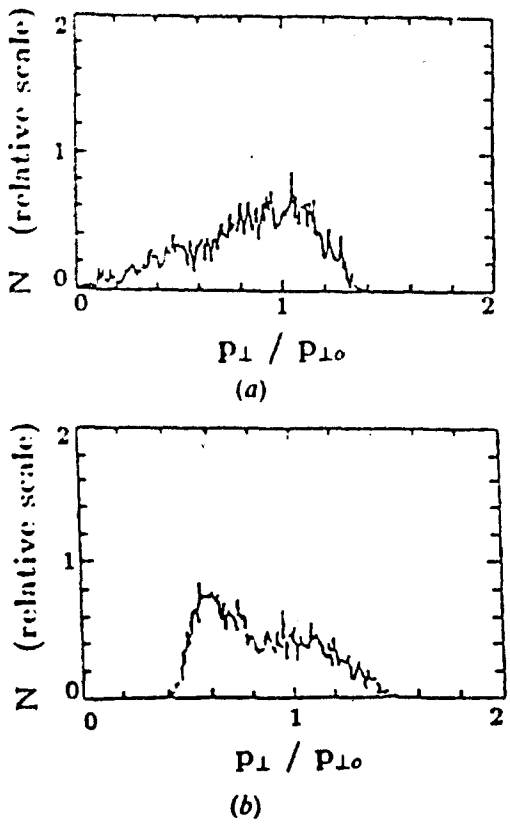

Figure 3. Distribution of transverse electron momentum at saturation for (*a*) Case a and (*b*) Case b.

TWT experiment has convincingly demonstrated (Chu *et al.* 1990 b) the effectiveness of such a scheme. Below we explore a design procedure based on this approach which can be systematically employed for high power gyro-TWT designs.

The design procedure is based on a marginal stability criterion, namely the conditions of each single stage are pushed to the point of marginal stability at the desired beam power and multiple stages (separated by attenuators) are employed to provide the desired gain.

To implement the marginal stability design, we first define a critical waveguide length (L_c) as the length below which all the modes are stable and above which one or more modes will be spontaneously oscillating. This length can readily be obtained by iterative simulation runs with all the likely oscillating modes included. The critical length thus obtained is observed in Fig. 6 to be a sensitive function of the beam current. At beam currents of interest to high power generation, L_c becomes too short to achieve significant gain in a single section. Hence, multiple stages are required. The simulation results provide a useful design guide. Upon fixing the beam current from power considerations, the marginal waveguide length can be found from Fig. 6, which is then taken to be the length of each section of the multi-stage gyro-TWT. Since each stage is stable to oscillations, the single-mode particle tracing code (Kou *et al.* 1991) can be employed for the subsequen. optimization of bandwidth, gain, and efficiency.

Figures 7 and 8 present examples of multi-stage gyro-TWT designs using the parameters of the Table. For Case a, the interaction length must be reduced to

4.5 cm completely to avoid oscillation of the various modes. To obtain a substantial gain, a three-stage system is required. Simulation results of the fundamental gyro-TWT based on the single mode particle tracing code are shown in Fig. 7. Employing a 5 A, 100 kV electron beam with an axial velocity spread of 5%, the fundamental harmonic gyro-TWT is predicted to achieve a maximum saturated gain of 50 dB, saturated output power of 128 kW (25·6% efficiency), and a 3·2 GHz bandwidth (9·3%). On the other hand, an interaction length of 7·95 cm suffices to exclude all oscillations for Case b. A three-stage system is again used to provide ample gain. Simulation results of the second harmonic gyro-TWT are presented in Fig. 8. Using a 25 A, 100 kV electron beam with an axial velocity speed of 5%, the second harmonic gyro-TWT is predicted to achieve a maximum saturated gain of 54 dB, a saturated output power of 532 kW (21·3% efficiency), and a 2·0 GHz bandwidth (8·7%).

4. Summary and discussion

This investigation begins with a multi-mode, time-dependent simulation study of the stability properties of the gyro-TWT. For high beam power, it is shown that self-oscillations arising from the interactions of various waveguide modes and different cyclotron harmonics can grow to significant saturation levels such that they completely spoil the amplification process. To address the critical issue of stability, we propose a marginal stability design procedure which has been motivated by two recent experimental developments. The demonstration of a severed gyro-TWT (Chu

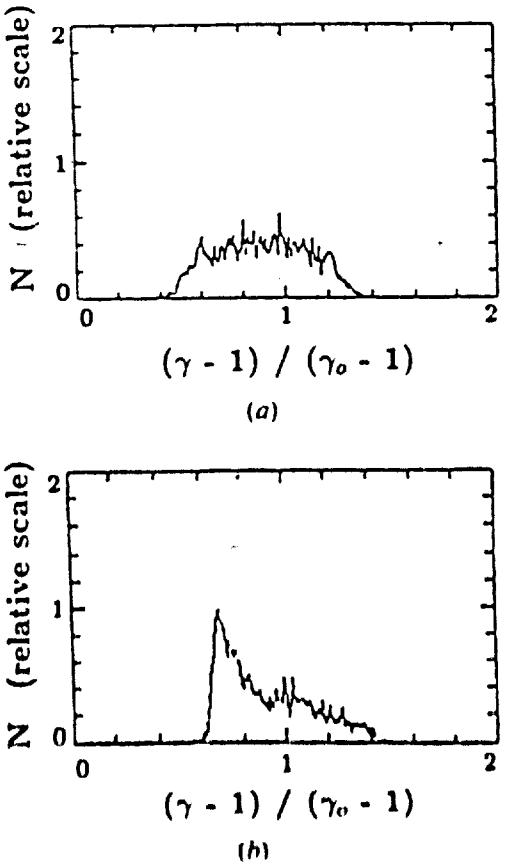

Figure 4 Distribution of electron energy at saturation for (*a*) Case a and (*b*) Case b

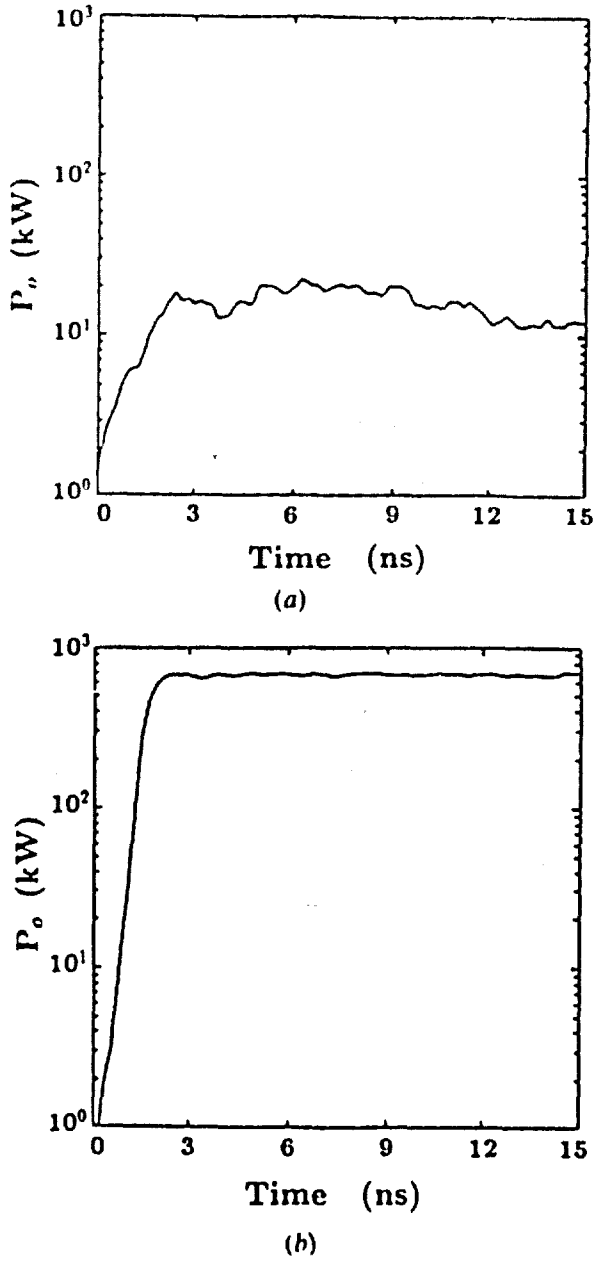

Figure 5. Temporal growth of TE_{21} drive wave for Case b due to (*a*) spoiled beam of Figs 3(*b*) and 4(*b*) and (*b*) good quality beam.

et al. 1990 b) proves the feasibility of a multi-stage interaction structure which is an essential element of the design scheme. The demonstration of the suppression of oscillation by a drive wave (Barnett *et al.* 1989, Chu *et al.* 1990 a, 1991) justifies the proposed borderline design concept, since weak oscillations, if present, can be effectively suppressed by the drive. In many applications, where occasional oscillation is unacceptable, an unconditionally stable gyro-TWT can be obtained by choosing the section lengths to be less than L_c by a safety margin of $\sim 5\%$.

The stability analysis and design examples all indicate that a gyro-TWT operating at the second cyclotron harmonic has significantly greater power capability than the fundamental harmonic version. As one keeps increasing the output

power through the marginal stability design procedure, an ultimate limit will be imposed by factors not accounted for in the present model. DC space charge depression of the electron beam is a well-known limiting factor in beam formation. AC space-charge effects (Charbit *et al.* 1981, Liu and Yang 1981, Chen and Chu 1986, Chu and Lyu 1986, Antonsen *et al.* 1986, Latham 1990) can modify the operating mode (growth rate, mode structure, etc.) or introduce entirely new unstable modes. The ultimate capacity of the gyro-TWT will not be known until we have a better understanding of these various high current effects.

Finally, several caveats on these high power gyro-TWTs should be discussed. In the analysis, the ends of each section were assumed to be perfect matches, not only at the operating frequency, but also for the various harmonic interactions. This is especially difficult to achieve for the input coupler. The gyro-BWO stability length can be expected to decrease for finite reflections. Fortunately, the relevant parameter for oscillation is the product of the two reflection coefficients and it is fairly straightforward to build a broadband attenuator, although this is somewhat complicted by the fact that the most serious competing mode is the first and

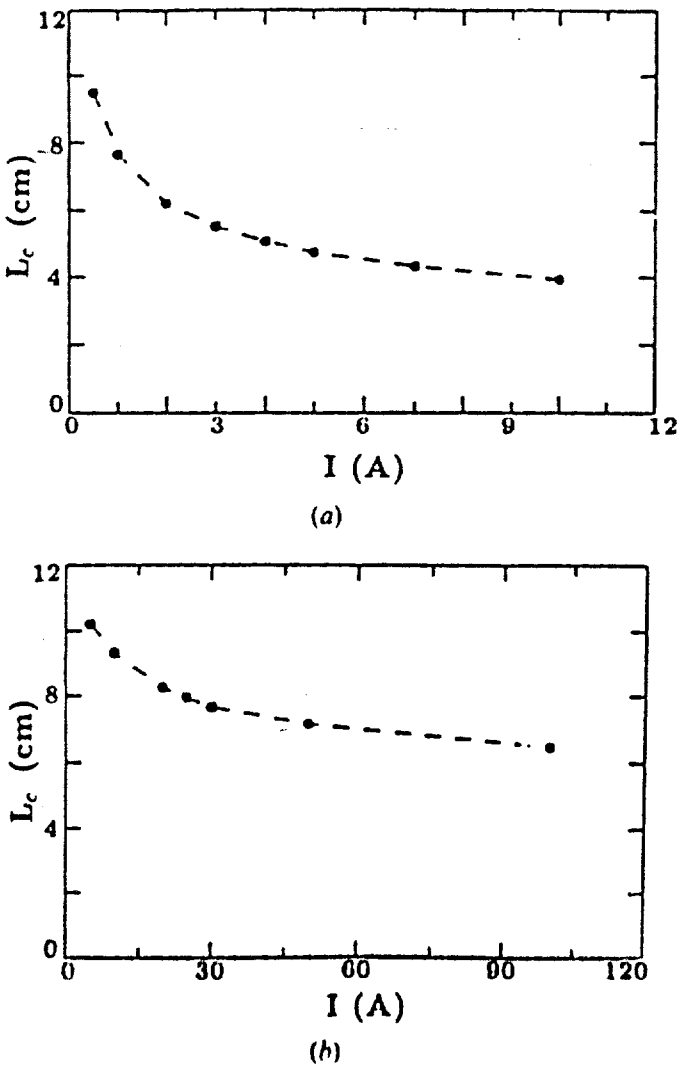

Figure 6. Dependence of start oscillation length on beam current for (*a*) Case a and (*b*) Case b.

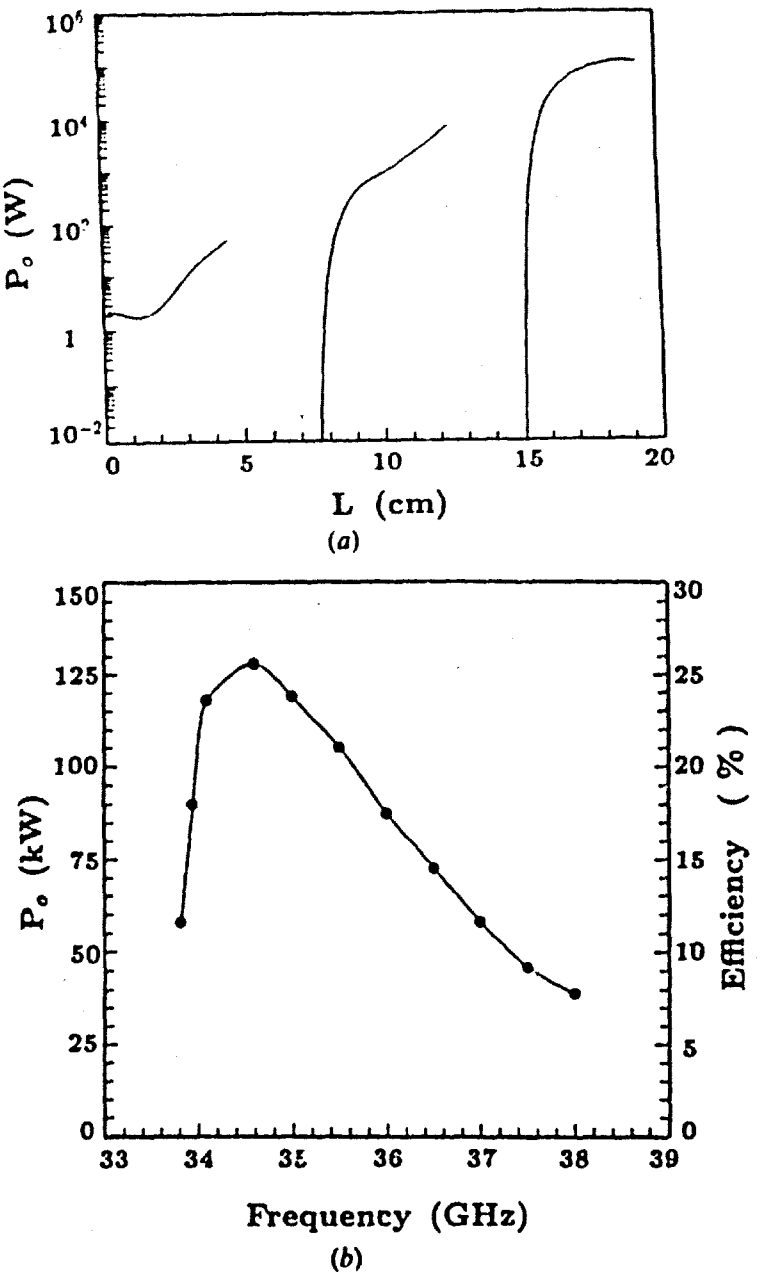

Figure 7. Performance of Case a using a three-stage design: (*a*) Spatial power profile of 34·6 GHz wave driven into saturation and (*b*) saturated output power and efficiency versus frequency.

second harmonic amplifiers threatens to oscillate near its cut-off. A further concern is the high power capability of the attenuating sever. The attenuator used in the recent severed gyro-TWT experiment (Chu *et al.* 1990 b) was a tapered ceramic tube with a lossy inner coating. An improved version may have to be designed before these devices are operated with high average power.

Acknowledgments

We thank Dr R. B. True of Litton for his informative comments about the capabilities of cusp electron guns, which provided guidelines for the choice of beam

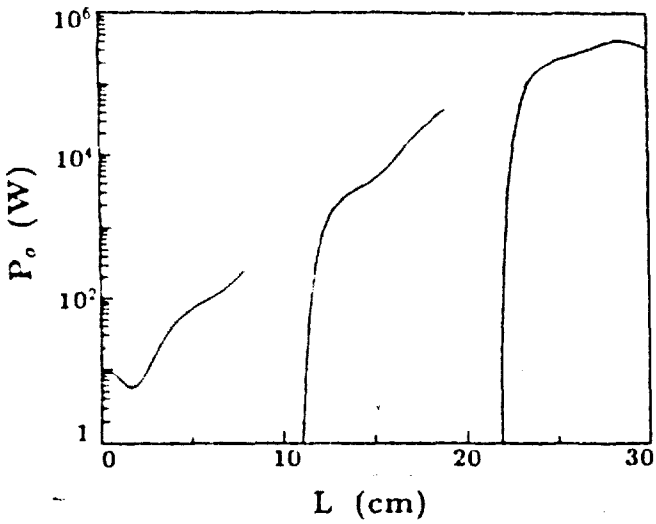

(*a*)

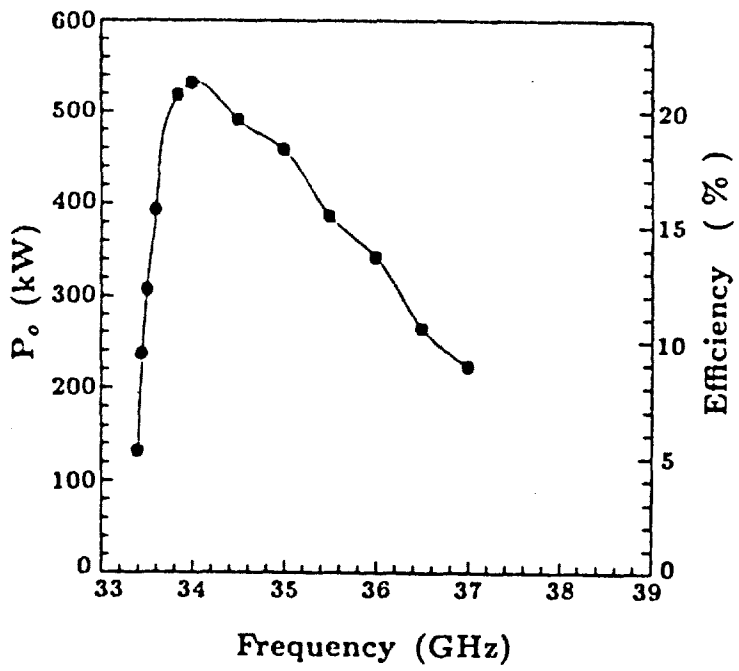

(*b*)

Figure 8. Performance of Case b using a three-stage design: (*a*) Spatial power profile of 34 GHz wave driven into saturation and (*b*) saturated output power and efficiency versus frequency.

parameters in the simulations and design. This work is sponsored by DARPA through Navy/White Oak Laboratory NSWC (Contract No. N60921-90-C-0253), the Air Force Office of Scientific Research (Contract No. 91-0006), the Army Research Office (Contract No. DAAL03-91-G-0190) and the San Diego Supercomputing Center.

References

Antonsen, T. M., Jr, Manheimer, W. M., and Levush, B., 1986, Effect of AC and DC transverse self-fields in gyrotrons. *International Journal of Electronics*, **61**, 823-854.

BAIRD, J. M., and LAWSON, W., 1986, Magnetron injection gun (MIG) design for gyrotron applications. *International Journal of Electronics*, **61**, 953-967.

BARNETT, L. R., CHANG, L. H., CHEN, H. Y., CHU, K. R., LAU, W. K., and TU, C. C., 1989, Absolute instability competition and suppression in a millimeter-wave gyrotron traveling-wave tube. *Physical Review Letters*, **63**, 1062-1065.

BARNETT, L. R., CHU, K. R., BAIRD, J. M., GRANATSTEIN, V. L., and DROBOT, A. T., 1979, Gain, saturation, and bandwidth measurements of the NRL gyrotron traveling amplifier. *Technical Digest of the I.E.E.E. International Electron Devices Meeting*, New York, pp. 164-167.

BUTTERWORTH, J. C., and WALLACE, T. V., 1987, High power MMW transmitters. *Principles and Applications of Millimeter-Wave Radar*, edited by N. C. Currie and C. E. Brown (Norwood, Mass: Artech House), p. 465.

CHEN, K. R., and CHU, K. R., 1986, Study of a noise amplification mechanism in gyrotrons. *I.E.E.E. Transactions on Microwave Theory and Techniques*, **34**, 72-79.

CHARBIT, P., HERSCOVICI, A., and MOURIER, G., 1981, A partly self-consistent theory of the gyrotron. *International Journal of Electronics*, **51**, 303.

CHU, K. R., BARNETT, L. R., LAU, W. K., CHANG, L. H., and CHEN, H. Y., 1990a, A wide-band millimeter-wave traveling wave amplifier experiment. *I.E.E.E. Transactions on Electron Devices*, **37**, 1557-1560.

CHU, K. R., BARNETT, L. R., LAU, W. K., CHANG, L. H., and KOU, C. S., 1990b, Recent developments in gyro-TWT research in NTHU. *Technical Digest of the I.E.E.E. International Electron Devices Meeting*, New York, pp. 699-702.

CHU, K. R., BARNETT, L. R., LAU, W. K., CHANG, L. H., LIN, A. T., and LIN, C. C., 1991, Nonlinear dynamics of the gyrotron traveling wave amplifier. *Physics of Fluids* B, **3**, 2403-2408.

CHU, K. R., and DIALETIS, D., 1985, Kinetic theory of harmonic gyrotron oscillator with slotted resonant structure. *Infrared and Millimeter Waves*, Vol. 13, edited by K. J. Button (New York: Academic Press), Chap. 3.

CHU, K. R., and LIN, A. T., 1988, Gain and bandwidth of the gyro-TWT and CARM amplifiers. *I.E.E.E. Transactions on Plasma Science*, **16**, 90-104.

CHU, K. R., and LYU, L. H., 1986, Simulation of electrostatic noise amplification in gyrotrons. *I.E.E.E. Transactions on Microwave Theory and Techniques*, **34**, 690-695.

DAVIES, J. A., 1989, Conditions for absolute instability in the cyclotron resonance maser. *Physics of Fluids* B, **1**, 663-669.

DESTLER, W. W., KULKARNI, R., STRIFFLER, C. D., and WEILER, R. L., 1983, Microwave generation from rotating electron beams in magnetron-type waveguides. *Journal of Applied Physics*, **54**, 4152-4162.

GRANATSTEIN, V. L., and PARK, S. Y., 1983, Survey of recent gyrotron developments. *Technical Digest of the I.E.E.E. International Electron Devices Meeting, I.E.E.E.*, New York, pp. 263-266.

GRANATSTEIN, V. L., READ, M. E., and BARNETT, L. R., 1984, Measured performance of gyrotron oscillators and amplifiers. *Infrared and Millimeter Waves*, Vol. 5, edited by K. J. Button (New York: Academic Press), Chap. 5.

KOU, C. S., 1991, The design procedure of a stable high power gyro-TWT. Ph.D. dissertation, Department of Electrical Engineering, University of California, Los Angeles.

KOU, C. S., MCDERMOTT, D. B., and LUHMANN, N. C., JR, 1991, A nonlinear self-consistent analysis of a two-stage gyro-TWT amplifer, to be published.

KOU, C. S., MCDERMOTT, D. B., LUHMANN, N. C., JR, and CHIU, K. R., 1990, Prebunched high-harmonic gyrotron. *I.E.E.E. Transactions on Plasma Science*, **18**, 343-349.

LATHAM, P. E., 1990, AC space-charge effects in gyroklystron amplifiers. *I.E.E.E. Transactions on Plasma Science*, **18**, 273-285.

LAU, Y. Y., and BARNETT, L. R., 1982, Theory of a low field harmonic gyrotron. *International Journal of Infrared Millimeter Waves*, **3**, 619-644.

LAU, Y. Y., CHU, K. R., BARNETT, L. R., and GRANATSTEIN, V. L., 1981, Gyrotron traveling-wave amplifier: analysis of oscillations. *International Journal of Millimeter Waves*, **2**, 373-393.

LIN, A. T., and LIN, C. C., 1989, Stabilization of the absolute instability in cyclotron autoresonance maser amplifiers by a drive wave. *Physics of Fluids* B, **1**, 2286-2288.

LIU, S., and YANG, Z., 1981, The kinetic theory of the electron cyclotron maser with space charge effect. *International Journal of Electronics*, **51**, 341.

MCDERMOTT, D. B., LUHMANN, N. C., JR, FURUNO, D. S., KUPISZEWSKI, A., and JORY, H. R., 1983, Operation of a millimeter-wave harmonic gyrotron. *International Journal of Millimeter Waves*, **4**, 639-664.

NAMKUNG, W., 1984, Observation of microwave generation from a cusptron device. *Physics of Fluids*, **27**, 329-330.

PARK, S. Y., GRANATSTEIN, V. L., and PARKER, R. K., 1984, A linear theory and design study for a gyrotron backward-wave oscillator. *International Journal of Electronics*, **57**, 1109-1123.

SCHEITRUM, G. P., SYMONS, R. S., and TRUE, R. B., 1989, Low velocity spread axis encircling electron beam forming system. *Technical Digest of the I.E.E.E. International Electron Devices Meeting*, New York, pp. 743-746.

A.2. High-Power Harmonic Gyro-TWTs - Part I: Linear Theory and Oscillation Study

High-Power Harmonic Gyro-TWT's—Part I: Linear Theory and Oscillation Study

C. S. Kou, Q. S. Wang, D. B. McDermott, *Member, IEEE*, A. T. Lin, K. R. Chu, *Senior Member, IEEE*, and N. C. Luhmann, Jr.

Abstract— **A linear theory using Laplace transforms is presented which is applicable to both gyrotron traveling wave amplifiers (gyro-TWT's) and gyrotron backward wave oscillators (gyro-BWO's). The validity of the linear theory is verified by comparing it with an existing nonlinear self-consistent theory based on a different approach. In conjunction with a time-dependent multimode particle simulation code, the linear theory is applied to study the stability of harmonic gyro-TWT's. It is shown that a harmonic gyro-TWT can be made stable to all forms of spontaneous oscillations by employing a multistage interaction structure and that it can generate power levels far in excess of those possible for a fundamental gyro-TWT. The linear bandwidth of a second-harmonic gyro-TWT amplifier is also calculated.**

I. Introduction

BEING an amplifier capable of high-power millimeter-wave generation, the gyro-TWT is finding an increasing number of applications, particularly in radar and communication systems, owing mainly to its promise of high gain and broad bandwidth. Yet, in contrast to the more developed gyrotron oscillators, gyro-TWT amplifier research is still in a very preliminary state. To date, only a few fundamental gyro-TWT experiments have been completed [1]–[3], and the gain, efficiency, and bandwidth of these amplifiers are still significantly below theoretical predictions. A very important obstacle has been the gyro-TWT's susceptibility to oscillation.

Two types of oscillations have been observed to degrade the performance experimentally. In an early TE_{01} gyro-TWT experiment at the Naval Research Laboratory [4], oscillation near cutoff caused by the absolute instability [5] occurred and was stabilized in a later experiment by using a waveguide with a resistive wall [6]. The second kind of oscillation, gyrotron backward wave oscillation (gyro-BWO), was observed in a recent gyro-TWT experiment performed at the National Tsing Hua University, in Taiwan [2], where clear evidence of competition with the amplified TE_{11} circular waveguide mode from backward wave oscillation in the TE_{21} mode at the second harmonic was recorded. The experiment also indicated the effectiveness of an attenuating sever in suppressing the spontaneous oscillations.

Many theoretical works [7]–[23] on the general physics of gyro devices, including gyro-TWT's, have been published, but only a few theoretical studies on the problem of spontaneous oscillations have appeared [24], [25]. These theoretical analyses provide important insight into the absolute oscillation threshold for gyro-TWT's. Meanwhile, a linear theory has been formed for the design of a gyro-BWO [26], where a wave is excited which propagates toward the electron gun. The stability of a gyro-TWT can also be jeopardized by gyro-BWO interactions in many possible modes and at various harmonics. The purpose of this paper is to apply a similar linear theory to study the stability problem of harmonic gyro-TWT's operating in any TE_{mn} circular waveguide mode. In conjunction with a multimode particle simulation code [27], it will be shown that a harmonic gyro-TWT amplifier can be made stable to all types of spontaneous oscillations by shortening its interaction length.

In a fundamental gyro-TWT, the amplified RF frequency ω is approximately equal to the electron cyclotron frequency, $\Omega_c = eB_0/\gamma m_0 c$, where B_0 is the axial magnetic field, $\gamma = [1 - (\beta_\perp^2 + \beta_\parallel^2)]^{-1/2}$ is the relativistic mass factor, $\beta = v/c$, v is the electron velocity, c is the speed of light in vacuum, and e and m_0 are the electron charge and rest mass, respectively. The magnetic field required for operation is directly proportional to the operating frequency. The availability of magnetic field will, therefore, practically set an upper limit on the frequency which can be amplified by a fundamental gyro-TWT. However, harmonic devices will extend this limit, making high-frequency sub-millimeter-wave amplification possible.

Because harmonic interactions are in general weaker than the fundamental interaction, they are more stable to oscillations and therefore allow much higher levels of electron beam current [28]. Thus, harmonic gyro-TWT's can yield, in principle, significantly greater power than a fundamental gyro-TWT. The electron beam geometry which yields the highest gain for harmonic interaction is an axis-encircling beam, but the cusp guns which can create these beams are still undergoing development [29] and have not yet demonstrated the requisite parameters. However, it is shown in this paper and in the accompanying nonlinear study [30] that a magnetron

Manuscript received October 1, 1991; revised January 30, 1992. This work was supported by AFOSR under Grant 91-0382 and by ARO under Contract DAAL03-91-G-0190.

C. S. Kou was with the Department of Electrical Engineering, University of California at Los Angeles. He is now with the Department of Physics, National Tsing Hua University, Taiwan, Republic of China.

Q. S. Wang, D. B. McDermott, and N. C. Luhmann, Jr., are with the Department of Electrical Engineering, University of California at Los Angeles, Los Angeles, CA 90024.

A. T. Lin is with the Department of Physics, University of California at Los Angeles, Los Angeles, CA 90024.

K. R. Chu was with the Department of Physics, University of California at Los Angeles, on leave from the Department of Physics, National Tsing Hua University, Taiwan, Republic of China.

IEEE Log Number 9108117.

injection gun (MIG), which is a mature technology [31], is also suitable for high-power harmonic gyro-TWT's. The general stability study presented in this paper is appropriate for both axis-encircling and MIG beam geometries.

This paper is organized as follows. In Section II, a general analytical linear theory is presented. The Laplace transformation approach follows that of Park *et al.* [26]. While the equations given in [26] apply only to the TE_{n0} rectangular and TE_{0n} circular waveguide modes, the linear theory [32] described in this paper can be applied to any TE_{mn} mode of cylindrical waveguide, which is the circuit geometry most commonly employed in gyro devices. The linear theory and the time-dependent multimode particle simulation code are then used in Section III to determine the conditions for stability. The stability limits for the interaction length are found. A reduction of the interaction length can effectively stabilize [28] all forms of spontaneous oscillations. Based on the linear theory, the initial working parameter space can be searched and narrowed so that a final set of design parameters can be determined and the large-signal performance of the design can be evaluated by self-consistent, nonlinear computer simulations as presented in the accompanying paper [30]. Section IV concludes the paper with a brief discussion.

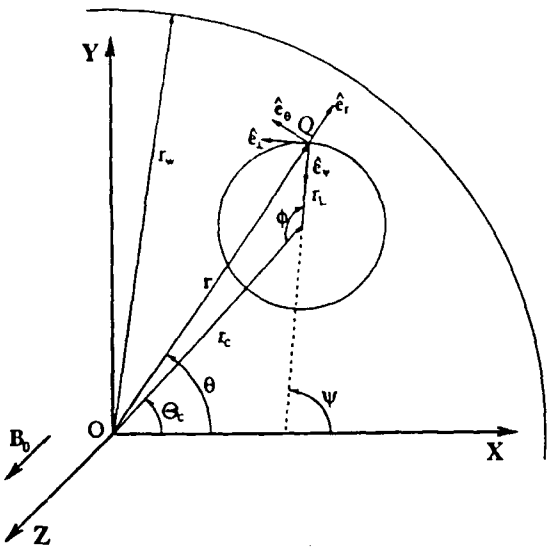

Fig. 1 Projection of equilibrium electron orbit on cross-sectional plane of waveguide in uniform magnetic field B_0. Point O is the center of waveguide, r_w is the waveguide radius, point Q is the instantaneous position of the electron. r_L, r_c, and Θ_c are the electron Larmor radius, guiding center radius, and azimuthal angle, respectively, and r and θ are real-space polar coordinates.

II. Analytical Linear Theory

Consider either an annular or an axis-encircling tenuous beam of magnetized electrons whose distribution function in real and momentum space is given by

$$f(\boldsymbol{r},p,t) = f_0(\boldsymbol{r},p) + f_1(\boldsymbol{r},p,t), \tag{1}$$

with f_0 being the unperturbed (equilibrium) and f_1 the perturbed distribution caused by a TE_{mn} circular waveguide mode written as

$$\begin{aligned} \boldsymbol{E}_\perp &= \frac{1}{k_{mn}} F(z)\hat{\boldsymbol{e}}_z \times \nabla_\perp \Psi_{mn}(\boldsymbol{r}), \\ \boldsymbol{E}_z &= 0, \\ \boldsymbol{B}_\perp &= \mathcal{F}(z)\nabla_\perp \Psi_{mn}(\boldsymbol{r}) \end{aligned} \tag{2}$$

and

$$\boldsymbol{B}_z = -j\frac{k_{mn}}{k} F(z)\Psi_{mn}(\boldsymbol{r}).$$

A time dependence of the form $e^{j\omega t}$ has been assumed with

$$\begin{aligned} \Psi_{mn}(\boldsymbol{r}) &= C_{mn} J_m(k_{mn}r)e^{-jm\theta}, \\ C_{mn} &= \frac{1}{\sqrt{\pi(x_{mn}^2 - m^2)}J_m(x_{mn})}, \\ \mathcal{F}(z) &= -j\frac{1}{kk_{mn}}\frac{\partial F}{\partial z} \end{aligned}$$

and

$$\nabla_\perp = \hat{\boldsymbol{e}}_r\frac{\partial}{\partial r} + \hat{\boldsymbol{e}}_\theta\frac{1}{r}\frac{\partial}{\partial \theta}$$

where $k = \omega/c$, $k_{mn} = x_{mn}/r_w$ and x_{mn} is the nth root such that $J'_m(k_{mn}r_w) = 0$ is satisfied at the waveguide wall radius, r_w. For a tenuous electron beam, the transverse field profiles of the waveguide modes are assumed to be the same as those of a cold waveguide. The function, $F(z)$, having the dimension of field strength, is the axial profile of the mode. Consistent with a linear analysis, the assumption of $f_1 \ll f_0$ is also made.

Using the TE_{mn} mode projection operator $\Psi^*_{mn}e^{-j\omega t}$ and Graff's addition theorem for Bessel functions, from Maxwell's wave equation one can straightforwardly obtain

$$\left(\frac{\partial^2}{\partial z^2} + k_z^2\right)F(z) = S(z) \tag{3}$$

with the source term

$$\begin{aligned} S(z) = {} & j\frac{4\pi k_{mn}^2 \omega C_{mn}}{c^2} \\ & \cdot \sum_{s=-\infty}^{\infty} \int_0^{2\pi} d\theta \\ & \cdot \int_0^{r_w} \Big(r dr J_\perp(\boldsymbol{r},t) J_{m-s}(k_{mn}r_c) \\ & \cdot J'_s(k_{mn}r_L)e^{-j\Lambda} \Big) \end{aligned} \tag{4}$$

where $k_z = \sqrt{(\omega/c)^2 - k_{mn}^2}$ is the axial wave number of the wave, r_c and r_L are the beam's guiding center and Larmor radii, respectively, $J_\perp(\boldsymbol{r},t)$ is the transverse component of the beam current density, and $\Lambda = \omega t - m\psi + (s-m)(\phi - \pi)$ is a phase variable defined with reference to Fig. 1. Equation (3) is the reduced wave equation for the axial field profile $F(z)$ driven by the induced beam current.

The induced beam current resulting from the influence of the RF field is described by the perturbed distribution function

$f_1(r,p,t)$, which can be written as

$$f_1(r,p,t) = \frac{eC_{mn}}{\omega}\sum_{s=-\infty}^{\infty} e^{j\Lambda(t)}\int_0^z dz' T_s(z-z')F_s(z') \tag{5}$$

when the linearized Vlasov equation is solved by the method of characteristics. In (5) the transfer function T_s is defined as

$$T_s(z-z') = \frac{1}{v_z}e^{-j(\omega - s\Omega_c)(z-z')/v_z} \tag{6}$$

and the effects of the RF fields are represented by (7), given at the bottom of the page. Equation (5) is a typical hysteresis integral and indicates that the RF electric field F_s at a point z' affects the electron distribution at a point z cumulatively through the transfer function $T_s(z-z')$. As a result of the modulation produced by the RF fields, the electron energies are perturbed and, therefore, so are their cyclotron frequencies, which induces an azimuthal bunching in the electron phase distribution. This electron phase modulation represents an induced beam current, $J_\perp(r,t)$, which is determined by the electron distribution function $f_1(r,p,t)$ given by (5). When $J_\perp(r,t)$ is substituted into (3) and (4), the field amplitude $F(z)$ can be determined self-consistently by solving the resulting one-dimensional integrodifferential equation.

The integrodifferential equation can be solved by using the Laplace transformation defined as

$$\mathcal{L}[F(z)] \equiv \tilde{F}(k_\parallel) \triangleq \int_0^\infty dz e^{jk_\parallel z}F(z) \tag{8}$$

where $k_\parallel$ is a complex wave number. Applying the Laplace transformation and using the convolution theorem, (3) can be reduced to a simple algebraic equation for $\tilde{F}(k_\parallel)$ in $k_\parallel$ space

$$\left(\frac{\omega^2}{c^2} - k_\parallel^2 - k_{mn}^2\right)\tilde{F}(k_\parallel) = \tilde{S}(k_\parallel) - jk_\parallel F(0) + F'(0) \tag{9}$$

where

$$F(0) = F(z)|_{z=0}$$

and

$$F'(0) = \left.\frac{dF(z)}{dz}\right|_{z=0}$$

are the initial conditions.

Under the Laplace transformation, the source term $S(z)$ on the right-hand side of (3) becomes

$$\tilde{S}(k_\parallel) = S_1(k_\parallel)\tilde{F}(k_\parallel) + S_0(k_\parallel)F(0), \tag{10}$$

where

$$S_1(k_\parallel) = \frac{16\pi^3 e^2 k k_{mn} C_{mn}^2}{m_0 c^2}\sum_{s=-\infty}^{\infty}\int_0^{r_c^{max}} r_c dr_c \int_0^\infty p_\perp dp_\perp \int_{-\infty}^\infty dp_z \cdot \frac{f_0}{\gamma}\left[\frac{-(\omega^2 - k_\parallel^2 c^2)\beta_\perp^2 H_{sm}(k_{mn}r_c, k_{mn}r_L)}{\left(\omega - k_\parallel v_z - \frac{s\Omega_{c0}}{\gamma}\right)^2} + \frac{(\omega - k_\parallel v_z)T_{sm}(k_{mn}r_c, k_{mn}r_L) - k_{mn}v_\perp U_{sm}(k_{mn}r_c, k_{mn}r_L)}{\omega - k_\parallel v_z - \frac{s\Omega_{c0}}{\gamma}}\right] \tag{11}$$

and

$$S_0(k_\parallel) = j\frac{16\pi^3 e^2 k k_{mn} C_{mn}^2}{m_0 c}\sum_{s=-\infty}^{\infty}\int_0^{r_c^{max}} r_c dr_c \cdot \int_0^\infty p_\perp dp_\perp \int_{-\infty}^\infty dp_z \frac{f_0}{\gamma} \cdot \left[\frac{-\beta_\perp^2\beta_{ph}^{-1}\omega H_{sm}(k_{mn}r_c, k_{mn}r_L)}{(\omega - k_\parallel v_z - \frac{s\Omega_{c0}}{\gamma})^2} + \frac{\beta_z T_{sm}(k_{mn}r_c, k_{mn}r_L)}{\omega - k_\parallel v_z - \frac{s\Omega_{c0}}{\gamma}}\right] \tag{12}$$

with

$$H_{sm}(x,y) = J_{s-m}^2(x)J_s'^2(y), \tag{13}$$

$$T_{sm}(x,y) = 2H_{sm}(x,y) + yJ_s'(y)\left\{2J_{s-m}^2(x)J_s''(y) - J_s(y)\left[\frac{1}{x}J_{s-m}(x)J_{s-m}'(x) + J_{s-m}'^2(x) + J_{s-m}(x)J_{s-m}''(x)\right]\right\}$$

and

$$U_{sm}(x,y) = -\frac{1}{2}yJ_s'(y)\{J_{s-1}(y)[J_{s-m-1}^2(x) - J_{s-m}^2(x)] + J_{s+1}(y)[J_{s-m+1}^2(x) - J_{s-m}^2(x)]\}.$$

The evaluation of the remaining integrals depends upon the specific functional form of the electron beam distribution function $f_0(r_c, p_\perp, p_z)$. For a monoenergetic cold beam, the initial distribution function can be written as

$$f_0 = N_b\delta(\gamma - \gamma_0)\frac{1}{2\pi p_{\perp 0}}\delta(p_\perp - p_{\perp 0})\frac{1}{2\pi r_{c0}}\delta(r_c - r_{c0}) \tag{14}$$

$$F_s(z') = J_{m-s}(k_{mn}r_c)J_s(k_{mn}r_L)\left[\left(\omega F + \frac{p_z}{\gamma m_0}kk_{mn}\mathcal{F}\right)\frac{\partial f_0}{\partial p_\perp} - \frac{p_\perp}{\gamma m_0}kk_{mn}\mathcal{F}\frac{\partial f_0}{\partial p_z}\right] - \frac{1}{m_0\Omega_{c0}}\left\{J_{m-s}'(k_{mn}r_c)J_s(k_{mn}r_L)\left(\omega F + \frac{p_z}{\gamma m_0}kk_{mn}\mathcal{F}\right) - \frac{k_{mn}p_\perp}{2\gamma m_0}F \cdot [J_{m-s-1}(k_{mn}r_c)J_{s+1}(k_{mn}r_L) - J_{m-s+1}(k_{mn}r_c)J_{s-1}(k_{mn}r_L)]\right\}\frac{\partial f_0}{\partial r_c} \tag{7}$$

and the integrations in (11) and (12) are trivially removed, with the integration variables being replaced by their initial values. In (14), the constant N_b is the number of electrons in one unit of axial length.

Making use of the $k_\parallel$ space representation of the field amplitude $\tilde{F}(k_\parallel)$, as determined by (9), of the inverse Laplace transformation

$$F(z) \equiv \mathcal{L}^{-1}[\tilde{F}(k_\parallel)] \triangleq \frac{1}{2\pi}\int_{j\delta-\infty}^{j\delta+\infty} dk_\parallel e^{-jk_\parallel z}\tilde{F}(k_\parallel),$$

and of the residue theorem, the field amplitude in real space can be expressed in terms of the initial values $F(0)$ and $F'(0)$ as

$$F(z) = F(0)\sum_i e^{-jk_{\parallel i}z}\frac{N(k_{\parallel i})}{jD'(k_{\parallel i})} + F'(0)\sum_i e^{-jk_{\parallel i}z}\frac{1}{jD'(k_{\parallel i})} \quad (15)$$

where

$$D(k_\parallel) = \frac{\omega^2}{c^2} - k_\parallel^2 - k_{mn}^2 - S_1(k_\parallel), \quad (16)$$

$$D'(k_\parallel) = \frac{d}{dk_\parallel}D(k_\parallel)$$

and

$$N(k_\parallel) = S_0(k_\parallel) - jk_\parallel. \quad (17)$$

In (15), the $k_{\parallel i}$ is the ith zero of first order of the equation

$$D(k_{\parallel i}) = 0, \quad (18)$$

which is simply the complex dispersion relation describing the coupling between the electron beam and the waveguide modes.

Given a set of beam and wave parameters, the wave evolution is completely determined by (18) and (15). For an ideal beam with the distribution function given by (14), the dispersion relation (eq. (18)) becomes

$$D(\omega,k_\parallel) = \frac{\omega^2}{c^2} - k_\parallel^2 - k_{mn}^2 - \frac{4I_b/I_A}{r_w^2\mathcal{K}_{mn}}\left[\frac{-\beta_{\perp 0}^2\left(\omega^2-k_\parallel^2c^2\right)H_{sm}(k_{mn}r_{c0},k_{mn}r_{L0})}{(\omega-k_\parallel v_{\parallel 0}-s\Omega_{c0}/\gamma_0)^2} + \frac{(\omega-k_\parallel v_{\parallel 0})\,T_{sm}(k_{mn}r_{c0},k_{mn}r_{L0})}{\omega-k_\parallel v_{\parallel 0}-s\Omega_{c0}/\gamma_0} - \frac{k_{mn}v_{\perp 0}\,U_{sm}(k_{mn}r_{c0},k_{mn}r_{L0})}{\omega-k_\parallel v_{\parallel 0}-s\Omega_{c0}/\gamma_0}\right] = 0 \quad (19)$$

where $I_A = (3\times 10^9)^{-1}(m_0c^3/e)\beta_{\parallel 0}\gamma_0 \approx 17\beta_{\parallel 0}\gamma_0$ kA is the Alfvén critical current, I_b is the dc beam current in amperes and the constant $\mathcal{K}_{mn} = J_m^2(x_{mn})(1 - m^2/x_{mn}^2)$. Equation (19) is the same as the previous result [25] derived from a different approach. In the above, it has been assumed that the axial magnetic field is tuned such that the TE_{mn} wave interacts primarily at the sth harmonic cyclotron frequency. It then follows that the H_{sm} term in (19) will dominate over terms being proportional to T_{sm} and U_{sm}, as it is inversely proportional to the second order of $(\omega - k_\parallel v_{\parallel 0} - s\Omega_{c0}/\gamma_0) \sim 0$. It is the coupling function $H_{sm}(k_{mn}r_c, k_{mn}r_L)$ that gives rise to the cyclotron instability. The dispersion relation (eq. (19)) is a fourth-order polynomial in ω and $k_\parallel$, which has four complex roots. When these four roots are substituted into (15), a superimposed wave made up of four individual waves is formed. For the situation where the beam cyclotron mode couples with the waveguide mode in the forward direction, there exist one backward wave with constant amplitude and three forward waves, of which one is growing, one is decaying, and the last one remains constant in amplitude. The situation will be reversed if the beam cyclotron mode couples with the waveguide mode in the backward direction.

Once the wave amplitude profile has been determined, the time-averaged power flow in the circuit can be calculated as

$$P_w = Re\left\{\int dA\cdot\frac{c}{8\pi}(E\times B^*)\right\} = \frac{c^2}{8\pi}\frac{1}{\omega k_{mn}^2}\mathrm{Re}\{F(z)jF'(z)^*\}. \quad (20)$$

The linear gain is then given by

$$G(z) = \frac{P_w(z)}{P_w(0)} = \frac{\mathrm{Im}\{F(z)F'(z)^*\}}{\mathrm{Im}\{F(0)F'(0)^*\}} \quad (21)$$

for a forward growing wave ($\mathrm{Re}\{k_\parallel\} > 0$), and

$$G(z) = \frac{P_w(0)}{P_w(z)} = \frac{\mathrm{Im}\{F(0)F'(0)^*\}}{\mathrm{Im}\{F(z)F'(z)^*\}} \quad (22)$$

for a backward growing wave ($\mathrm{Re}\{k_\parallel\} < 0$).

Equations (15), (19), (21), and/or (22) are solved subject to the following boundary conditions:

1) *Forward Traveling Wave Launched at $z = 0$:*

$$|F(0)| = \sqrt{\frac{8\pi\omega k_{mn}^2}{c^2k_z}P_w(0)}$$

and

$$\frac{dF(z)}{dz}|_{z=0} = -jk_zF(0).$$

2) *Backward Traveling Wave Initialized at $z = L$:*

$$\frac{dF(z)}{dz}|_{z=0} = jk_zF(0)$$

and

$$\mathrm{Re}\{F(z)\} + j\mathrm{Im}\{F(z)\} = 0 \quad \text{at } z = L. \quad (23)$$

It is straightforward to find the linear gain for the forward wave by simply following the wave evolution through the interaction tube. For the backward wave, however, one must solve the set of simultaneous nonlinear equations (eq. (23)) for the two unknowns, namely, the backward wave oscillation frequency and the start oscillation length. When both the real and the imaginary part of (23) are satisfied, the gain given by (22) will be infinite, which implies that the device will oscillate, yielding finite output power at $z = 0$.

III. Oscillation Conditions

A study of the dispersion relation reveals that two types of spontaneous oscillations may be excited in a gyro-TWT amplifier, oscillations arising from the absolute instability and gyrotron backward wave oscillations (gyro-BWO). In Fig. 2, the cold waveguide dispersion relation and the beam–wave resonance lines are shown for both a $TE_{11}^{(1)}$ and a $TE_{21}^{(2)}$ gyro-TWT amplifier (the superscripts represent the cyclotron harmonic number). A 100 kV beam with $\alpha \equiv v_\perp/v_\parallel = 1$ and $B_0 = 0.98B_g$ have been assumed, where B_g is the grazing magnetic field at which the beam–wave resonance line grazes the operating waveguide mode curve. The solid curves and solid straight lines represent the operating waveguide mode and the cyclotron harmonic resonance, respectively. Also shown in the figure by the broken curves and lines are other neighboring modes and harmonics. It is seen that in a $TE_{21}^{(2)}$ gyro-TWT, no oscillation at the fundamental frequency can be excited, since the fundamental beam–wave resonance line is well below the lowest order waveguide mode.

Wave amplification will occur when the beam cyclotron mode couples with the waveguide mode near the grazing intersection point. There will be a finite width of unstable spectrum about the intersection. If this unstable band is confined to the forward wave region only ($k_\parallel > 0$), a wave will travel down the interaction tube with convectively growing amplitude. However, if the unstable band is sufficiently wide to extend into the backward wave region ($k_\parallel < 0$), waves growing in the backward direction will be excited and provide internal feedback to yield self-oscillation near cutoff. If this oscillation occurs, it will grow in time (absolutely) when viewed at a fixed spatial position.

Relying on the original criteria in [5], one may distinguish the absolute instability from the convective instability. It is known that the absolute instability occurs as a zero of second order of the dispersion relation (eq. (19)). When the dispersion relation is solved and the behavior of its roots is traced numerically in the $\omega - k_\parallel$ space, the threshold current for the onset of the absolute instability can be determined [25]. Fig. 3 shows the threshold currents for the absolute instability in (a) $TE_{11}^{(1)}$ and (b) $TE_{21}^{(2)}$ gyro-TWT amplifiers as a function of α. A 100 kV, axis-encircling beam was assumed in both calculations. For a MIG-type beam, the start oscillation currents will be somewhat higher than those shown in Fig. 3, as the interaction between off-axis electrons and the wave is weaker. It is clear from the figure that the start oscillation current has a strong functional dependence on α. As the beam current must be maintained below the relatively low threshold current level to ensure stability, the output power capability of a fundamental gyro-TWT is greatly limited. However, a harmonic gyro-TWT has a weaker interaction strength and can therefore be operated with a much higher value of current, as shown in Fig. 3 (more than a fivefold increase in this case). In other words, a harmonic gyro-TWT amplifier is more stable to self-oscillation owing to the absolute instability than a fundamental gyro-TWT. As a result, a harmonic gyro-TWT can generate significantly higher output power than a fundamental gyro-TWT for a given beam voltage and velocity ratio α.

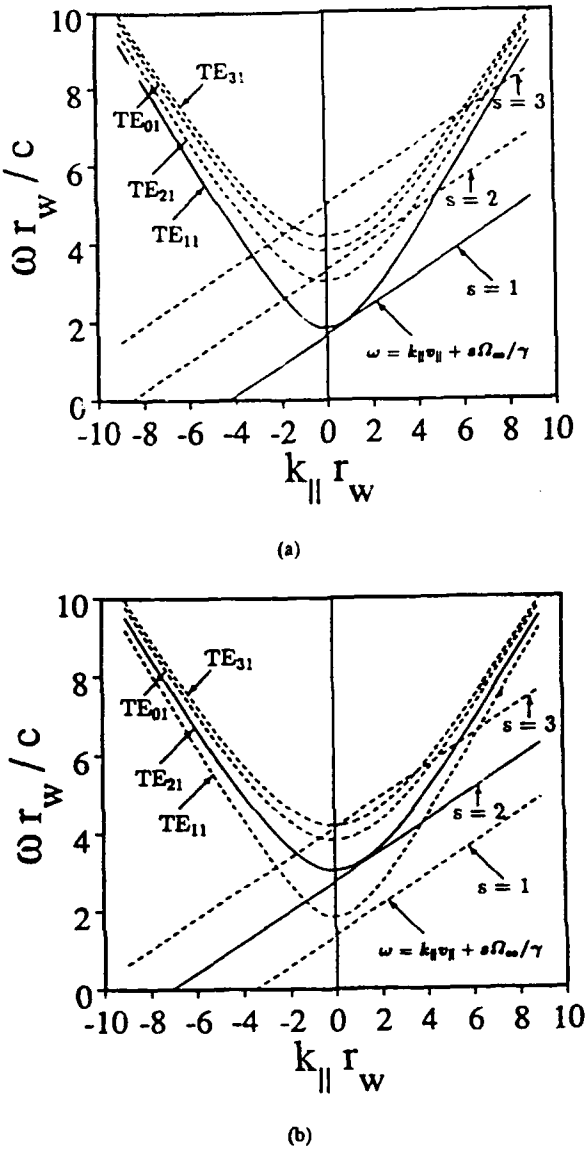

Fig. 2. Uncoupled dispersion relation of operating mode (intersection of unbroken curves) and likely oscillating modes (intersections of broken curves with negative $k_\parallel$) for (a) $TE_{11}^{(1)}$ gyro-TWT amplifier and (b) $TE_{21}^{(2)}$ gyro-TWT amplifier (100 kV, $\alpha = 1, B_0 = 0.98B_g$).

In addition to the self-excited oscillations caused by the absolute instability, a gyro-TWT amplifier is also susceptible to spontaneous backward wave oscillations which occur at intersections with negative $k_\parallel$. As shown in Fig. 2(b), there are various gyro-BWO modes, $TE_{11}^{(2)}$, $TE_{21}^{(3)}$, etc., competing with the operating $TE_{21}^{(2)}$ mode in the second-harmonic gyro-TWT. These modes will be excited with the gain profiles given by (22) if the interaction tube length is longer than the critical lengths determined by the gyro-BWO boundary conditions (eq. (23)).

The starting oscillation length of each competing gyro-BWO mode has been calculated and the results for the $TE_{31}^{(3)}$ and $TE_{11}^{(2)}$ modes, which have the shortest critical lengths, are shown in Fig. 4 as a function of beam current for a beam of 100 kV, $\alpha = 1$, $r_c/r_w = 0.4$, $r_w = 0.44$ cm, and $B_0/B_g = 0.98$.

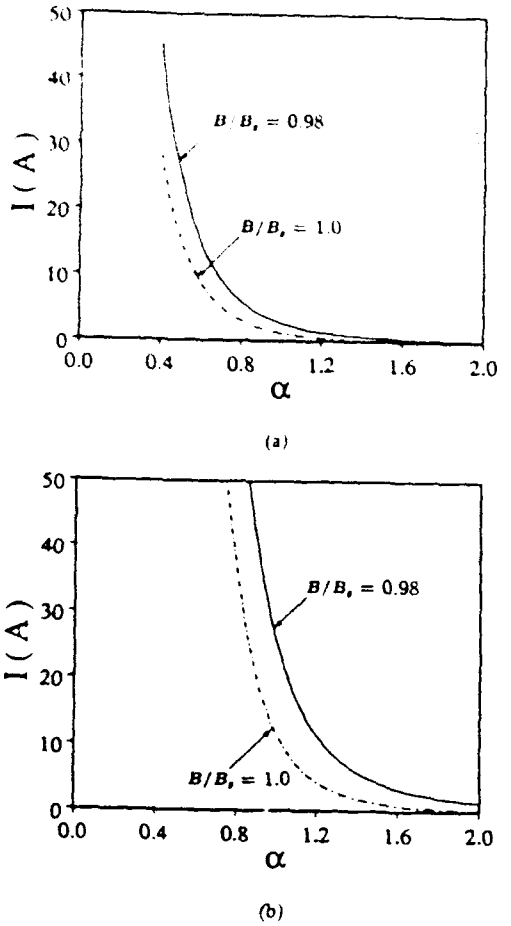

Fig. 3. Dependence of start oscillation current on velocity ratio α for absolute instability in (a) fundamental TE_{11} and (b) second-harmonic TE_{21} gyro-TWT amplifiers for two values of magnetic field (100 kV, axis-encircling beam).

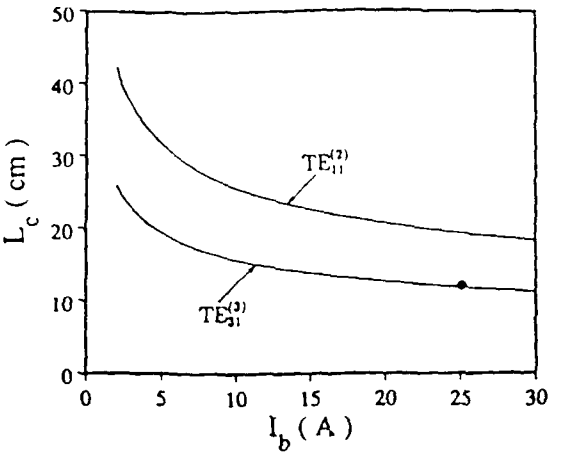

Fig. 4. Dependence of critical length on beam current for backward wave oscillations at second harmonic in TE_{11} mode and third harmonic in TE_{31} mode (100 kV, $\alpha = 1, r_c/r_w = 0.4, r_w = 0.44$ cm, $B_0/B_g = 0.98$ for $TE_{11}^{(2)}$ plot and $B_0/B_g = 1.15$ for $TE_{31}^{(3)}$ plot). Solid dot is from multimode particle simulation.

Notice from Fig. 2 that the $TE_{31}^{(3)}$ intersection actually occurs for a forward wave. Since the $TE_{31}^{(3)}$ interaction is so close to the cutoff, spontaneous oscillations arising from the absolute instability will almost definitely occur unless proper methods for its suppression are used. Using the time-dependent, multimode particle simulation code, we have observed that there also exists a critical length for oscillation owing to the absolute instability. Since the present analytical linear theory model does not include finite length effects for the spontaneous oscillations caused by the absolute instability, the magnetic field ratio B_0/B_g was artificially increased 17%. This was done so that the $TE_{31}^{(3)}$ intersection occurs for a backward wave such that the preceding analytical theory can be used to obtain a $TE_{31}^{(3)}$ critical length comparable to that predicted by the more accurate multimode particle simulation code. The critical length of 12 cm found from the multimode simulation code for $TE_{31}^{(3)}$ oscillation for the correct design value of magnetic field has also been included in Fig. 4 as a solid circle. Fig. 4 shows that it is the critical length for the $TE_{31}^{(3)}$ mode that limits the interaction length. From Fig. 4 it can be seen that the critical length is very sensitive to the beam current in the low-current regime ($L_c \approx I_b^{-1/3}$). However, in the high-beam-current regime of interest, the critical length depends only very weakly on the beam current. In this regime, the interaction length needs be reduced only slightly to maintain stability for a very large increase in the beam current.

Using an interaction length less than the shortest critical length for all possible spontaneous oscillations, a gyro-TWT amplifier can be kept stable. If the critical length is too short to allow amplification with reasonable gain, multiple stages separated by attenuating severs can be used, where the length of each stage is still kept shorter than the critical length. This procedure [28] will ensure single-mode operation together with a high amplification gain.

IV. Discussion and Conclusions

The prediction of the linear theory described in Section II has been compared with that of an existing self-consistent nonlinear theory [30]. The results are shown in Fig. 5, where the power evolution in a $TE_{21}^{(2)}$ gyro-TWT amplifier with $B_0 = 0.98B_g$ is depicted for a 100 kV, 25 A beam with $\alpha = 1$ and $r_c/r_w = 0.4$. The comparison made in Fig. 5 shows perfect agreement in the linear region between the two theories derived from completely different approaches, an indication of the validity of both theories in that region. As expected, the linear theory fails in the saturation region, where nonlinearities become important.

In addition to the stability considerations, the linear theory has also been used to evaluate the linear performance of a $TE_{21}^{(2)}$ gyro-TWT amplifier for various beam parameters. The linear growth rate is shown in Fig. 6 with axial magnetic field, beam current, and electron velocity ratio as varying parameters. As expected, the interaction strength becomes stronger as α or the beam current is increased. The linear growth rate also increases with magnetic field strength as B_0 is raised toward the grazing magnetic field, B_g. For a 25 A, 100 kV beam with $\alpha = 1$ and $r_c/r_w = 0.4$ interacting with a $TE_{21}^{(2)}$ mode wave in a uniform magnetic field of $B_0 = 0.98B_g$, the 3 dB bandwidth predicted by the linear theory is 10.6%.

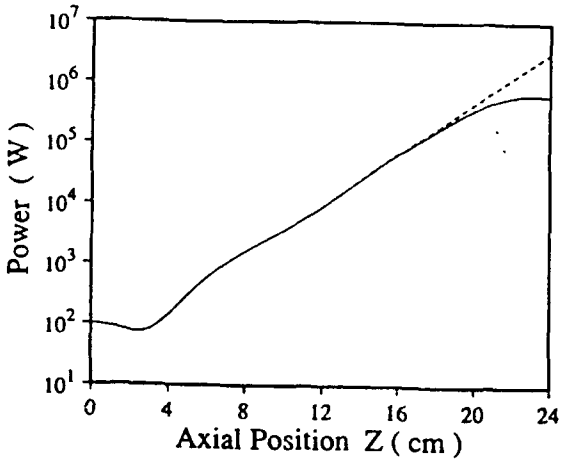

Fig. 5 Predicted spatial power profile of 35 GHz wave in $TE_{21}^{(2)}$ gyro-TWT from linear theory (broken curve) and nonlinear simulation (solid curve) (100 kV, 25 A, $\alpha = 1, r_c/r_w = 0.4$, and $B_0 = 0.98B_g$).

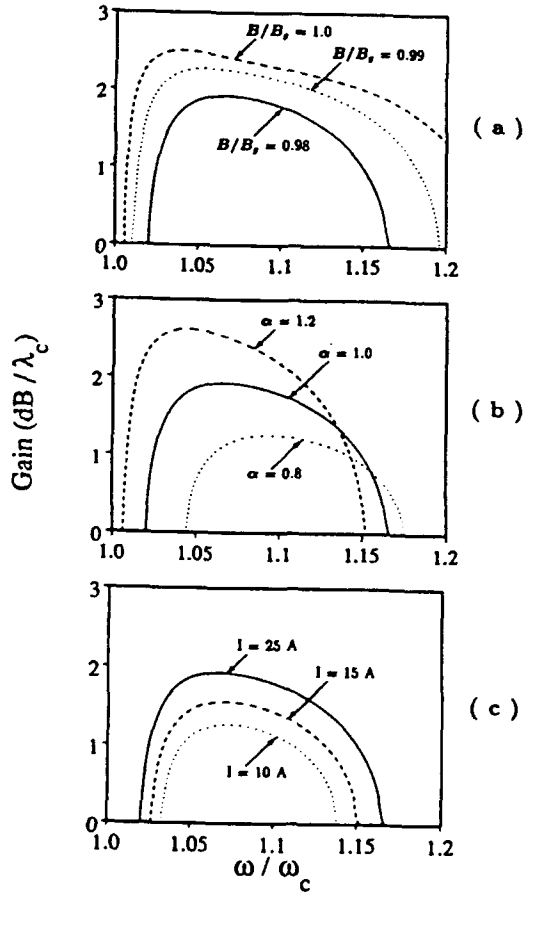

Fig. 6. Linear growth rate as a function of frequency in 100 kV, $TE_{21}^{(2)}$ gyro-TWT amplifier for (a) $I_b = 25$ A and $\alpha = 1$ for several values of magnetic field, (b) $I_b = 25$ A and $B_0 = 0.98B_g$ for several values of α, and (c) $\alpha = 1$ and $B_0 = 0.98B_g$ for several values of beam current. λ_c and ω_c are the cutoff wavelength and angular frequency, respectively. The ratio of the beam guiding center radius to the waveguide wall radius is 0.4.

The analytical linear theory presented in Section II has been developed based on a single-mode assumption and employed to analyze gyro-TWT stability, which is inherently a multi-mode problem. However, such a single-mode assumption and analysis are still proper for stability considerations, as the critical lengths so determined are less than the start oscillation lengths for the driven system. Using these critical lengths, each subsection of the gyro-TWT will, therefore, be stable to spontaneous oscillation, and the single-mode analysis for each stage will then be valid.

A general analytical linear theory has been developed for gyro devices involving any TE_{mn} circular waveguide mode at any cyclotron harmonic number. It has been demonstrated generally that harmonic gyro-TWT amplifiers not only can amplify high frequency at reduced magnetic field with ample gain, but also have potential for generating extremely high power in the millimeter-wave region. A second-harmonic gyro-TWT amplifier can be kept stable for beam current levels one order of magnitude higher than levels permitted in a stable fundamental gyro-TWT. The analytical linear theory can give a thorough physical understanding of the mechanisms of the various spontaneous oscillations and forms the basis for the design of high-power harmonic gyro-TWT amplifiers.

REFERENCES

[1] V. L. Granatstein, M. E. Read, and L. R. Barnett, "Measured performance of gyrotron oscillators and amplifiers," in *Infrared and Millimeter Waves*, vol. 5, K. J. Button, Ed. New York: Academic, 1984, pp. 267–304 (and references therein).

[2] K. R. Chu, L. R. Barnett, W. K. Lau, L. H. Chang, and C. S. Kou, "Recent developments in millimeter wave gyro-TWT research at NTHU," *Tech. Dig., IEEE Int. Electron Devices Meeting* (San Francisco), 1990, pp. 699–702.

[3] G. S. Park *et al.*, "Experimental study of a broadband millimeter-wave gyrotron travelling wave amplifier," *Tech. Dig., IEEE Int. Electron Devices Meeting* (Washington, DC), 1991, pp. 779–781.

[4] L. R. Barnett, K. R. Chu, J. M. Baird, V. L. Granatstein, and A. T. Drobot, "Gain, saturation and bandwidth measurements of the NRL gyrotron traveling wave amplifier," *Tech. Dig., IEEE Int. Electron Devices Meeting* (Washington, DC), 1979,pp. 164–167.

[5] R. J. Briggs, *Electron Stream Interaction with Plasma*. Cambridge, MA: MIT Press, 1964, ch. 2.

[6] L. R. Barnett, J. M. Baird, Y. Y. Lau, K. R. Chu, and V. L. Granatstein, "A high gain single stage gyrotron travelling wave amplifier," *Tech. Dig., IEEE Int. Electron Devices Meeting* (Washington, DC), 1980, pp. 314–317.

[7] E. Ott and W. M. Manheimer, "Theory of microwave emission by velocity-space instabilities of an intense relativistic electron beam," *IEEE Trans. Plasma Sci.*, vol. PS-3, pp. 1-5, 1975.

[8] P. Sprangle and A. T. Drobot, "The linear and self-consistent nonlinear theory of the electron cyclotron maser instability," *IEEE Trans. Microwave Theory Tech.*, vol. MTT-25, pp. 528–544, 1977.

[9] H. S. Uhm, R. C. Davidson, and K. R. Chu, "Self-consistent theory of cyclotron maser instability for intense hollow electron beams," *Phys. Fluids*, vol. 21, pp. 1866–1876, 1978; also pp. 1877–1886, 1978.

[10] K. R. Chu, A. T. Drobot, V. L. Granatstein, and J. L. Seftor, "Characteristics and optimum operating parameters of a gyrotron traveling wave amplifier," *IEEE Trans. Microwave Theory Tech.*, vol. MTT-27, pp. 178–187, 1979.

[11] K. R. Chu, A. T. Drobot, H. H. Szu, and P. Sprangle, "Theory and simulation of the gyrotron traveling wave amplifier operating at cyclotron harmonics," *IEEE Trans. Microwave Theory Tech.*, vol. MTT-28, pp. 313–317, 1980.

[12] C. J. Edgcombe, "The dispersion equation for the gyrotron amplifier," *Int. J. Electron.*, vol. 48, pp. 471–486, 1980.

[13] J. Y. Choe and S. Ahn, "General mode analysis of a gyrotron dispersion relation," *IEEE Trans. Electron Devices*, vol. ED-28, pp. 94–102, 1981.

[14] R. S. Symons and H. R. Jory, "Cyclotron resonance devices," in *Advances in Electronics and Electron Physics*, vol. 55, L. Marton and C. Marton, Eds. New York: Academic, 1981, pp. 1-75.

[15] P. Charbit, A. Herscovici, and G. Mourier, "A partly self-consistent theory of the gyrotron," *Int. J. Electron.*, vol. 51, p. 303, 1981.

[16] S. Liu and Z. Yang, "The kinetic theory of the electron cyclotron maser with space charge effect," *Int. J. Electron.*, vol. 51, p. 341, 1981.
[17] P. A. Lindsay, "Self-consistent large signal interaction in a TWT gyrotron," *Int. J. Electron.*, vol. 51, p. 379, 1981.
[18] A. T. Lin, M. Caplan, and K. R. Chu, "A study of saturated output of a TE_{01} gyrotron using an electromagnetic finite size particle code," *Int. J. Electron.*, vol. 53, p. 659, 1982.
[19] A. K. Ganguly and S. Ahn, "Self-consistent large signal theory of a gyrotron travelling wave amplifier," *Int. J. Electron.*, vol. 53, p. 505, 1982.
[20] P. A. Lindsay, R. J. Lumsden, and R. M. Jones, "A dispersion relation for gyrotron TWT's," *Int. J. Electron.*, vol. 53, p. 619, 1982.
[21] Y. Y. Lau, "Simple macroscopic theory of cyclotron maser instabilities," *IEEE Trans. Electron Devices*, vol. ED-29, p. 320, 1982.
[22] T. M. Antonsen, W. M. Manheimer, and B. Levush, "Effect of ac and dc transverse self-fields in gyrotrons," *Int. J. Electron.*, vol. 61, p. 823, 1986.
[23] A. W. Fliflet, "Linear and nonlinear theory of the Doppler-shifted cyclotron resonance maser based on TE and TM waveguide modes," *Int. J. Electron.*, vol. 61, p. 1049, 1986.
[24] Y. Y. Lau, K. R. Chu, L. R. Barnett, and V. L. Granatstein, "Gyrotron travelling wave amplifier: I. Analysis of oscillations," *Int. J. Infrared Millimeter Waves*, vol. 2, pp. 373–393, 1981.
[25] K. R. Chu and A. T. Lin, "Gain and bandwidth of the gyro-TWT and CARM amplifiers," *IEEE Trans. Plasma Sci.*, vol. 16, pp. 90–104, Apr. 1988.
[26] S. Y. Park, V. L. Granatstein, and R. K. Parker, "A linear theory and design study for a gyrotron backward-wave oscillator," *Int. J. Electron.*, vol. 57, no. 6, pp. 1109–1123, 1984.
[27] A. T. Lin and C. C. Lin, "Stabilization of the absolute instability in cyclotron autoresonance maser amplifier by a drive wave," *Phys. Fluids B*, vol. 1, no. 11, pp. 2286–2288, 1989.
[28] A. T. Lin *et al.*, "Marginal stability design criterion for gyro-TWT's and comparison of fundamental with second harmonic operation," *Int. J. Electron.*, to be published.
[29] G. P. Scheitrum, R. S. Symons, and R. B. True, "Low velocity spread axis encircling electron beam forming system," in *Tech. Dig., IEEE Int. Electron Devices Meeting* (Washington, DC), 1989, pp. 743–746.
[30] Q. S. Wang *et al.*, "High-power harmonic gyro-TWT's—Part II: Nonlinear theory and design," pp. 163–169, this issue.
[31] J. M. Baird and W. Lawson, "Magnetron injection gun (MIG) design for gyrotron applications," *Int. J. Electron.*, vol. 61, no. 6, pp. 953–967, 1986.
[32] C. S. Kou, "Design procedure for a stable high power gyro-TWT," Ph.D. dissertation, Dept. of Electrical Engineering, Univ. of California, Los Angles, 1991.

C. S. Kou, photograph and biography not available at the time of publication.

Q. S. Wang, photograph and biography not available at the time of publication.

D. B. McDermott (M'83), photograph and biography not available at the time of publication.

A. T. Lin, photograph and biography not available at the time of publication.

K. R. Chu (SM'82), photograph and biography not available at the time of publication.

N. C. Luhmann, Jr., photograph and biography not available at the time of publication.

A.3. High-Power Harmonic Gyro-TWTs - Part II: Nonlinear Theory and Design

High-Power Harmonic Gyro-TWT's—Part II: Nonlinear Theory and Design

Q. S. Wang, C. S. Kou, D. B. McDermott, *Member, IEEE*, A. T. Lin, K. R. Chu, *Senior Member, IEEE*, and N. C. Luhmann, Jr.

Abstract— **Based upon an analytical study of the stability problems of gyrotron traveling wave amplifiers (gyro-TWT's), the design of an extremely high power second-harmonic gyro-TWT has been developed and then evaluated and optimized with a self-consistent nonlinear numerical simulation code. Although an axis-encircling electron beam yields stronger interaction, a design based on the more common magnetron injection gun (MIG) type beam is presented. Using a 100 kV, 25 A MIG beam with $\alpha = 1$ and an axial velocity spread of 5%, nonlinear self-consistent analysis of a three-stage second-harmonic gyro-TWT amplifier predicts a peak output power of 533 kW, peak efficiency of 21.3% and a 7.4% saturated bandwidth, which verifies the assessments of analytical theory that a stable harmonic gyro-TWT can generate power levels an order of magnitude higher than those possible from a fundamental gyro-TWT. It is shown that the positioning of the electron beam is very important. A multistage structure is employed in the design to recover the loss in gain resulting from the shortening of the interaction sections to ensure stability.**

I. Introduction

THE gyrotron traveling wave amplifier (gyro-TWT) has been shown both theoretically and experimentally to be a highly efficient millimeter-wave amplifier. Because it employs a simple smooth waveguide structure, the gyro-TWT has far greater power handling capability than conventional TWT's. Having substantial gain and a broad bandwidth, gyro-TWT's have found a wide variety of applications such as power amplifiers in millimeter-wave radar and communication systems. To date, several experimental gyro-TWT's have been reported. An early gyro-TWT developed at the Naval Research Laboratory (NRL) [1]–[4] has amplified a TE_{01} circular waveguide mode near 35 GHz with 17–32 dB gain over a 13% bandwidth with a maximum efficiency of 16%. A recent gyro-TWT experiment at NRL [5] demonstrated the capability of broad bandwidth (33% bandwidth with 20 dB linear gain at 32.5 GHz) by tapering both the axial magnetic field and the waveguide. The first Varian gyro-TWT [6]–[8] achieved a remarkable 120 kW peak power near 5 GHz using the TE_{11} circular waveguide mode with a maximum efficiency of 26% and a bandwidth of 6%. The second Varian gyro-TWT [9] generated 30 kW at 94 GHz with a gain of 30 dB. Most recently, a group at the National Tsing Hua University has investigated the stability problem by demonstrating a 27 kW, K_a-band, severed gyro-TWT amplifier with 16% efficiency, 35 dB gain, and a full width at half maximum (FWHM) bandwidth of 7.5% using the TE_{11} circular waveguide mode [10]. All these reported gyro-TWT's have produced moderately high levels of output power (10–100 kW) and involved amplification only at the fundamental cyclotron harmonic frequency.

High-harmonic devices have also been developed to allow high-frequency operation at reduced magnetic field [11]–[16]. These high-harmonic devices used large-orbit, axis-encircling electron beams for strong interaction. However, the technique for forming such beams at high levels of current with the small axial velocity spreads required by an amplifier is still under development.

Important for a gyro-TWT's stability, the working beam current must be limited below the threshold value for an absolute instability to occur; also, the interaction length must be kept shorter than a critical length beyond which spontaneous gyrotron backward wave oscillations will take place [17]. In an sth-harmonic cylindrical TE_{s1} gyro-TWT, first-harmonic interaction will not occur, since the fundamental cyclotron resonance line is well below the lowest order waveguide mode as viewed in the uncoupled dispersion diagram. Previous theoretical studies have concluded that a harmonic gyro-TWT is more stable to oscillation than a fundamental gyro-TWT amplifier [17], [18], since harmonic interactions are in general weaker than the fundamental interaction. Therefore, harmonic interactions allow significantly higher levels of beam current and output power. If the gain of a single-stage gyro-TWT with a limited interaction length is too low, multiple stages separated by attenuating severs can be used to boost the amplification gain. Based on this marginal stability design procedure, a high-power, second-harmonic gyro-TWT design using an axis-encircling beam is given in [17]. Although an axis-encircling beam geometry is preferable for stronger interaction, cusp guns which can create these beams are still in development [19] and have not yet demonstrated the requisite parameters. Fortunately, nearly equivalent performance levels at the second harmonic can be achieved utilizing an annular beam formed by a conventional MIG. Since MIG's are a

Manuscript received October 1, 1991; revised January 30, 1992. This work was supported by AFOSR under Grant 91-0382 and by ARO under Contract DAAL03-91-G-0190.

Q. S. Wang, D. B. McDermott, and N. C. Luhmann, Jr., are with the Department of Electrical Engineering, University of California at Los Angeles, Los Angeles, CA 90024.

C. S. Kou was with the Department of Electrical Engineering, University of California at Los Angeles. He is now with the Department of Physics, National Tsing Hua University, Taiwan, Republic of China.

A. T. Lin is with the Department of Physics, University of California at Los Angeles, Los Angeles, 90024.

K. R. Chu was with the Department of Physics, University of California at Los Angeles, Los Angeles, CA 90024, on leave from National Tsing Hua University, Taiwan, Republic of China.

IEEE Log Number 9108116

mature technology [20], the high-power, second-harmonic gyro-TWT proposed in this paper employs a MIG as its electron gun.

This paper is organized as follows. In Section II, a presentation of the general three-dimensional, nonlinear self-consistent theory will be given only briefly, since many nonlinear theories have appeared in the literature [21]–[24]. The slow time-scale approach followed in developing the nonlinear formulation is similar to those used in [21] and [22]. As in [23] and [22], the formulation includes guiding center motion and spread, an axial magnetic field taper, and the modeling of attenuating severs in a smooth-wall circular waveguide. The design of a second-harmonic gyro-TWT will be described in Section III. Using the large signal code, it is shown that an output power far greater than that of state-of-the-art fundamental gyro-TWT's can be achieved for the designed three-stage gyro-TWT amplifier utilizing a MIG beam. Finally, Section IV will conclude the paper with a brief discussion of the results and possible future efforts.

II. Nonlinear Theory

Consider an annular or solid electron beam interacting with a copropagating circularly polarized circular waveguide TE_{mn} mode wave. The electron beam is injected into the interaction tube under the guidance of an applied dc magnetic field B_0. The electrons, moving along helical trajectories about guiding centers located at a radius r_{c0}, have a substantial part of their kinetic energy in the form of transverse cyclotron motion and the rest in the form of axial motion. Our nonlinear model assumes that all electrons have the same kinetic energy, $m_0c^2(\gamma - 1)$, but the partition between the transverse and longitudinal velocities may be different from electron to electron, where m_0 is the electron rest mass, $\gamma = [1 - (\beta_\perp^2 + \beta_\parallel^2)]^{-1/2}$ is the relativistic mass factor, $\boldsymbol{\beta} = \boldsymbol{v}/c, \boldsymbol{v}$ is the electron velocity, and c is the speed of light in vacuum. It is also assumed that the electron beam is sufficiently tenuous that it does not modify the normal mode of the cold waveguide and its space-charge field can be neglected. Only a single RF mode is assumed to be present in the waveguide with the specified frequency ω. Attenuation in the waveguide wall has been neglected.

For the purpose of frequency scaling and also to simplify the appearance of the set of nonlinear equations to be presented below, a normalization scheme is employed where the lengths are scaled against some arbitrarily specified length b (which is commonly chosen to be the waveguide radius, r_w). All normalized symbols are denoted by a bar. The normalization scheme is summarized in Table I. All dimensionless quantities such as $\alpha(= v_\perp/v_\parallel), \beta$, and γ are unchanged.

The electron dynamics are governed by the Lorentz force equation, given by

$$\frac{d\boldsymbol{p}}{dt} = -e\left[\boldsymbol{E} + \frac{1}{\gamma m_0 c}\boldsymbol{p} \times (\boldsymbol{B} + \boldsymbol{B}_0)\right], \tag{1}$$

where the applied magnetic field, $\boldsymbol{B}_0$, can be expressed as

$$\boldsymbol{B}_0 = B_0(z)\hat{\boldsymbol{e}}_z - \frac{1}{2}\frac{\partial B_0}{\partial z} r\hat{\boldsymbol{e}}_r. \tag{2}$$

TABLE I
Normalization for Nonlinear Formulation

Length	$\bar{r} = r/b$
Frequency	$\bar{\omega} = \omega b/c$
Time	$\bar{t} = tc/b$
Wave number	$\bar{k}_{mn} = k_{mn}b$
Momentum	$\bar{\boldsymbol{p}} = \boldsymbol{p}/m_0c = \gamma\boldsymbol{\beta}$
Power	$\bar{P}_w = P_w e^2/m_0^2c^5$
EM field	$\bar{E} = Eeb/m_0c^2$
Cyclotron frequency	$\bar{\Omega}_{c0} = \bar{B}_{0z} = eB_{0z}b/m_0c^2$
Beam current	$\bar{I}_b = I_b e/m_0c^3$
Current density	$\bar{J} = Jeb^2/m_0c^3$

In the above, $\boldsymbol{E}$ and $\boldsymbol{B}$ are the RF fields of the TE_{mn} circular waveguide mode as specified by

$$\boldsymbol{E}_\perp = \frac{1}{k_{mn}} F(z)\hat{\boldsymbol{e}}_z \times \nabla_\perp \Psi_{mn}(r),$$
$$E_z = 0,$$
$$\boldsymbol{B}_\perp = -j\frac{1}{kk_{mn}}\frac{\partial F}{\partial z}\nabla_\perp \Psi_{mn}(r)$$

and

$$B_z = -j\frac{k_{mn}}{k} F(z)\Psi_{mn}(r). \tag{3}$$

A time dependence of the form $e^{j\omega t}$ has been assumed with

$$\Psi_{mn}(r) = C_{mn}J_m(k_{mn}r)e^{-jm\theta},$$
$$C_{mn} = \frac{1}{\sqrt{\pi(x_{mn}^2 - m^2)}J_m(x_{mn})}$$

and

$$\nabla_\perp = \hat{\boldsymbol{e}}_r\frac{\partial}{\partial r} + \hat{\boldsymbol{e}}_\theta\frac{1}{r}\frac{\partial}{\partial\theta}$$

where $k = \omega/c$, $k_{mn} = x_{mn}/r_w$, and x_{mn} is the nth root such that $J_m'(k_{mn}r_w) = 0$ is satisfied at the waveguide wall radius, r_w. The function $F(z)$, having the dimension of field strength, is the unknown axial profile of the TE_{mn} mode.

Transformation of the coordinates from the cylindrical system to the guiding center system depicted in Fig. 1 and application of Graff's addition theorem for Bessel functions will change the general Lorentz force equation into a set of slow time-scale equations of motion governing the electron momentum and the phase angle, which are given by

$$\frac{\partial\bar{p}_\perp}{\partial\bar{z}} = \frac{1}{2}\frac{d\bar{\Omega}_{c0}}{d\bar{z}}\bar{r}_L - C_{mn}J_{m-s}(\bar{k}_{mn}\bar{r}_c) \cdot J_s'(\bar{k}_{mn}\bar{r}_L)\mathrm{Re}\left\{\left[\left(1 - \frac{\beta_z\bar{\kappa}}{\bar{\omega}}\right)\frac{\bar{f}}{\beta_z} - j\frac{1}{\bar{\omega}}\frac{d\bar{f}}{d\bar{z}}\right]e^{j\hat{\theta}}\right\}, \tag{4}$$

$$\frac{d\Lambda}{d\bar{z}} = \frac{1}{\beta_z}(\omega - s\bar{\Omega}_c) - (m - s)\frac{\partial\Theta_c}{\partial\bar{z}} - \frac{s}{\bar{p}_\perp}C_{mn}\frac{sJ_s(\bar{k}_{mn}\bar{r}_L)}{\bar{k}_{mn}\bar{r}_L}J_{m-s}(\bar{k}_{mn}\bar{r}_c) \cdot \mathrm{Re}\left\{\left[\left(1 - \frac{\beta_z\bar{\kappa}}{\bar{\omega}} - \frac{\bar{k}_{mn}^2\bar{r}_L^2\Omega_c}{s\bar{\omega}}\right)\frac{\bar{f}}{\beta_z} - j\frac{1}{\bar{\omega}}\frac{d\bar{f}}{d\bar{z}}\right]je^{j\hat{\theta}}\right\}, \tag{5}$$

and

$$\frac{\partial \bar{p}_z}{\partial \bar{z}} = -\frac{1}{2}\frac{d\bar{\Omega}_{c0}}{d\bar{z}}\frac{\beta_\perp}{\beta_z}\bar{r}_L - \frac{\beta_\perp}{\beta_z}\frac{C_{mn}}{\bar{\omega}} \cdot J_{m-s}(\bar{k}_{mn}\bar{r}_c)J_s'(\bar{k}_{mn}\bar{r}_L)\mathrm{Re}\left\{\left[j\frac{d\bar{f}}{d\bar{z}} + \bar{\kappa}\bar{f}\right]e^{j\theta}\right\} \quad (6)$$

where $\bar{p}_z$ and $p_\perp$ are electron axial and transverse momenta, respectively, $\Lambda = \omega t - m\varphi + (s-m)(\varphi - \pi)$ is a phase variable defined with reference to Fig. 1, r_L is the electron Larmor radius, and $\Omega_c = \Omega_{c0}/\gamma = eB_0/\gamma m_0 c$ is the relativistic electron cyclotron frequency. It has been assumed that the contribution from the sth harmonic to the interaction will dominate all the other harmonics. Similarly, the equations for the electron guiding center motion can be written in normalized form as

$$\frac{\partial \bar{r}_c}{\partial \bar{z}} = -\frac{1}{2}\frac{d\bar{\Omega}_{c0}}{d\bar{z}}\frac{\bar{r}_c}{\bar{\Omega}_{c0}} + \frac{C_{mn}}{\bar{\Omega}_{c0}} \cdot \mathrm{Re}\left\{\left(\left[\left(1 - \frac{\beta_z\bar{\kappa}}{\bar{\omega}} - \frac{s\bar{\Omega}_c}{\bar{\omega}}\right)\frac{\bar{f}}{\beta_z} - j\frac{1}{\bar{\omega}}\frac{d\bar{f}}{d\bar{z}}\right] \cdot J_{m-s}'(\bar{k}_{mn}\bar{r}_c)J_s(\bar{k}_{mn}\bar{r}_L) + \frac{\bar{r}_L}{\bar{r}_c}\frac{\bar{\Omega}_c}{\bar{\omega}}\frac{\bar{f}}{\beta_z}(m-s)J_{m-s}(\bar{k}_{mn}\bar{r}_c)J_s'(\bar{k}_{mn}\bar{r}_L)\right)e^{j\theta}\right\}, \quad (7)$$

and

$$\bar{r}_c\frac{\partial \Theta_c}{\partial \bar{z}} = \frac{C_{mn}}{\bar{\Omega}_{c0}}\mathrm{Im}\left\{\left(\left[\left(1 - \frac{\beta_z\bar{\kappa}}{\bar{\omega}} - \frac{s\bar{\Omega}_c}{\bar{\omega}}\right)\frac{\bar{f}}{\beta_z} - j\frac{1}{\bar{\omega}}\frac{d\bar{f}}{d\bar{z}}\right] \cdot \frac{(m-s)J_{m-s}(\bar{k}_{mn}\bar{r}_c)}{\bar{k}_{mn}\bar{r}_c}J_s(\bar{k}_{mn}\bar{r}_L) + \frac{\bar{k}_{mn}\bar{r}_L\bar{\Omega}_c}{\bar{\omega}}\frac{\bar{f}}{\beta_z}J_{m-s}'(\bar{k}_{mn}\bar{r}_c)J_s'(\bar{k}_{mn}\bar{r}_L)\right)e^{j\theta}\right\}. \quad (8)$$

In addition to the Lorentz force equation, it is also useful to consider the energy change equation

$$m_0c^2\frac{d\gamma}{dt} = -e\boldsymbol{v}\cdot\boldsymbol{E},$$

which, after similar manipulation, can be rewritten as

$$\frac{d\gamma}{d\bar{z}} = -\frac{\beta_\perp}{\beta_z}C_{mn}\bar{f}J_{m-s}(\bar{k}_{mn}\bar{r}_c)J_s'(\bar{k}_{mn}\bar{r}_L)\cos\bar{\theta}. \quad (9)$$

Equations (4)–(9) describe the electron motion in the presence of a strong axial magnetic field and the RF fields. A self-consistent formulation is completed when the amplitude of the wave field is calculated from the induced ac current density. This is done by lengthy but straightforward manipulations, very similar to those leading to (4) through (9), to rewrite the wave equation for the axial component of the magnetic field in terms of the slow time-scale variables. The normalized wave equations can be obtained as follows:

$$\left(\frac{\partial^2}{\partial\bar{z}^2} + \bar{\omega}^2 - \bar{k}_{mn}^2 - \bar{\kappa}^2\right)\bar{f} = -8\pi\bar{I}_b\bar{k}_{mn}^2\bar{\omega}C_{mn} \cdot \left\langle\frac{\bar{v}_{z0}}{\langle\bar{v}_{z0}\rangle}\frac{\bar{v}_\perp}{|\bar{v}_z|}J_{m-s}(\bar{k}_{mn}\bar{r}_c)J_s'(\bar{k}_{mn}\bar{r}_L)\sin\bar{\theta}\right\rangle \quad (10)$$

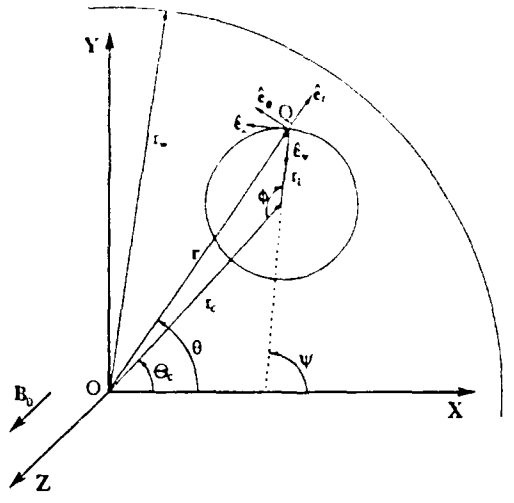

Fig. 1. Projection of equilibrium electron orbit on cross-sectional plane of waveguide in uniform magnetic field B_0. Point O is center of the waveguide, r_w is the waveguide radius, and point Q is the instantaneous position of the electron. r_L, r_c, and Θ_c are the electron Larmor radius, the guiding center radius, and the azimuthal angle, respectively, and r and θ are real-space polar coordinates.

and

$$\frac{\partial}{\partial\bar{z}}(\bar{\kappa}\bar{f}^2) = 8\pi\bar{I}_b\bar{k}_{mn}^2\bar{\omega}C_{mn}\bar{f} \cdot \left\langle\frac{\bar{v}_{z0}}{\langle\bar{v}_{z0}\rangle}\frac{\bar{v}_\perp}{|\bar{v}_z|}J_{m-s}(\bar{k}_{mn}\bar{r}_c)J_s'(\bar{k}_{mn}\bar{r}_L)\cos\bar{\theta}\right\rangle. \quad (11)$$

In deriving (10) and (11), which determine the wave's amplitude and phase, as well as (4)–(9), which describe electron motion, the normalized axial spatial profile of the RF wave field has been assumed to be of the form

$$\bar{F}(\bar{z}) = \bar{f}(\bar{z})e^{-j\zeta(\bar{z})}, \quad (12)$$

where $\zeta(\bar{z}) = \bar{k}_z\bar{z} - \varphi(\bar{z})$, $\bar{\kappa}(\bar{z}) = d\zeta/d\bar{z} = \bar{k}_z - d\varphi/d\bar{z}$, and φ is the wave phase. Also $\bar{\theta} = \Lambda - \zeta(\bar{z})$ is the electron phase with respect to the wave and $\langle\ \rangle$ stands for the ensemble average over the initial electron distributions of the axial momenta, guiding center positions, and gyro phases.

Finally, the spatial rate of change of power flow along the waveguide is calculated from the Poynting theorem and appears as

$$\frac{d\bar{P}_w}{d\bar{z}} = \bar{I}_bC_{mn}\bar{f}\left\langle\frac{\bar{v}_{z0}}{\langle\bar{v}_{z0}\rangle}\frac{\bar{v}_\perp}{|\bar{v}_z|}J_{m-s}(\bar{k}_{mn}\bar{r}_c)J_s'(\bar{k}_{mn}\bar{r}_L)\cos\bar{\theta}\right\rangle, \quad (13)$$

where $\langle v_{z0}\rangle$ is the electrons' average initial velocity, and I_b is the dc beam current.

Equations (4)–(13) form a closed set of ordinary differential equations. Two of them ((9) and (13)) are auxiliary equations which are included to monitor the accuracy of the numerical calculations. The nonlinear behavior of the electron motion as well as the wave evolution in gyro-TWT's, CARM amplifiers, etc. is completely and self-consistently determined by solving this set of equations. We employ a fourth-order Runge-Kutta algorithm to solve the differential equations, subject to the

initial conditions that $\kappa = k_z$ and $df/dz = 0$, as there is no net energy transfer for the initially unbunched beam assumed at the input ($z = 0$). The wave amplitude $f(z = 0)$ is calculated from the input signal power. The initial phase of the wave can be chosen arbitrarily, because all relevant quantities have been averaged over the initial electron phases.

The initial state of the electrons is chosen in such a way that the injection of a monoenergetic, axisymmetric beam is well represented. It is assumed that a finite number of electrons are uniformly distributed in phase, Λ_0, over a Larmor orbit with a radius r_{L0}. They are also uniformly distributed over the ring of an average guiding center radius. There may be a finite amount of spread in the guiding center radius. For an injected warm beam, a Gaussian distribution function of the form

$$G_0(p_z) = A\,\delta(\gamma - \gamma_0)\,e^{-(p_z - p_{z0})^2/2(\Delta p_z)^2}$$

is assumed for the beam axial momentum distribution. In the above, A is a normalization constant and p_{z0} is the average initial axial momentum.

III. Design of a Stable 0.5 MW Second-Harmonic Gyro-TWT

Application of the above nonlinear theory to a 100 kV, 25 A beam with $\alpha = 1$ and $r_c/r_w = 0.4$ in a single-stage second-harmonic TE_{21} gyro-TWT amplifier with waveguide radius $r_w = 0.44$ cm and $B_0 = 0.98B_g$ is shown in Fig. 2, where the spatial power profile is plotted. B_g is the magnetic field which results in a grazing intersection between the operating mode and the operating cyclotron harmonic resonance line. Also included in Fig. 2 is the result calculated from the linear theory [18] for the same set of beam and wave parameters. It can be seen that the two theories formed from different approaches agree very well in the linear region, an indication of the validity of both theories in that region. As expected, when nonlinearities become important in the saturation region, where the linear theory fails, an accurate nonlinear theory is needed to assess the large-signal behavior.

As pointed out in the introduction, harmonic interaction is relatively weak, leading to lower gain and a longer interaction length than the conventional fundamental gyro-TWT amplifier, unless other methods are applied. For example, for the case shown in Fig. 2, where the critical length for spontaneous oscillations to occur has been found to be 12 cm [18], an input power of more than 30 kW is required to drive the device into saturation, resulting in a power gain of only 14 dB. It is then essential to use a multistage gyro-TWT amplifier if high gain is needed. An accurate simulation of this system requires a nonlinear theory which is capable of modeling the attenuating severs which divide the gyro-TWT into multiple sections.

To model a severed gyro-TWT, the nonlinear formulation presented in Section II can still be applied to each individual stage. However, inside the sever region, the formulation has been modified to accommodate the assumption of infinite attenuation such that

$$F(z) = \frac{dF(z)}{dz} = 0$$

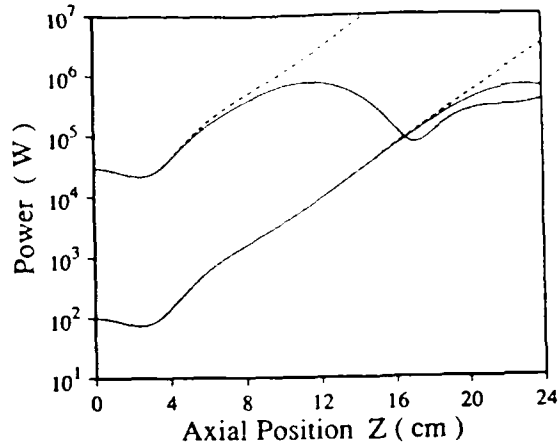

Fig. 2. Predicted spatial power profile of 35 GHz wave in $TE_{21}^{(2)}$ gyro-TWT from linear theory (broken curve) and nonlinear simulation (solid curve) for input powers of 100 W and 30 kW (100 kV, 25 A, $\alpha = 1$, $r_c/r_w = 0.4$, $r_w = 0.44$ cm, and $B_0 = 0.98B_g$).

inside the sever. The electron beam dynamics are still determined by (4)–(9) except that all the field quantities are set to zero. The assumption of infinite attenuation is reasonable inside a sever, because the presence of either lossy materials or the perturbation to the waveguide geometry will destroy the electron–wave synchronism. As a result, the effective field seen by the electrons will be essentially zero insider a sever even if the wave attenuation is finite. Because of the interaction with the RF field prior to the sever section, the electrons are azimuthally bunched in phase and will inertially preserve the bunch through the sever region.

At the exit of the sever, the ac electron beam parameters are continuous. This alternating current will then coherently induce an RF field in the circuit of the next stage. At the entrance to the next stage, it is assumed that the amplitude of the induced RF field is small (approaching zero) and $dF/dz = -jk_zF$. In the actual numerical simulations, the wave amplitude f has been set to be a very small value (< -40 dB of the initial value at $z = 0$), but still sufficiently large to avoid possible computer overflow difficulty. The phase of the wave at the entrance is set to the value at which the wave grows fastest, as the electron beam has been phase bunched by the RF field in the previous stages.

Using both the linear theory developed in [18] and the nonlinear theory described in the previous section, extensive parameter space searches have been performed, leading to the set of design parameters listed in Table II, upon which an experiment under construction at UCLA is based. All numerical simulations to be shown in this section are for the case listed in the table unless specified otherwise.

The MIG beam used in the design has a guiding center radius $r_c = 0.4r_w$, which is chosen by careful study of the behavior of the coupling function $H_{sm}(k_{mn}r_c, k_{mn}r_L)$ defined as [25], [18]

$$H_{sm}(x, y) = J_{s-m}^2(x)J_s'^2(y),$$

which has the physical meaning of being the effective

TABLE II
SECOND-HARMONIC 35 GHZ GYRO-TWT AMPLIFIER DESIGN

Beam voltage	100 kV
Beam current	25 A
Magnetic field	6.4 kG
Center frequency	35 GHz
Mode	TE_{21}
Cyclotron harmonic	2nd
Circuit radius	0.44 cm
r_c/r_w	0.4
α	1.0
B/B_g	0.98
$\Delta v_\parallel/v_\parallel$	5%
Number of stages	3
Section length	11.5 cm
Sever length	3 cm
Circuit length	40.5 cm
Simulation Results:	
Output power	533 kW
Saturated gain	54 dB
Efficiency	21.3%
Constant drive bandwidth	6%
Saturated bandwidth	7.4%

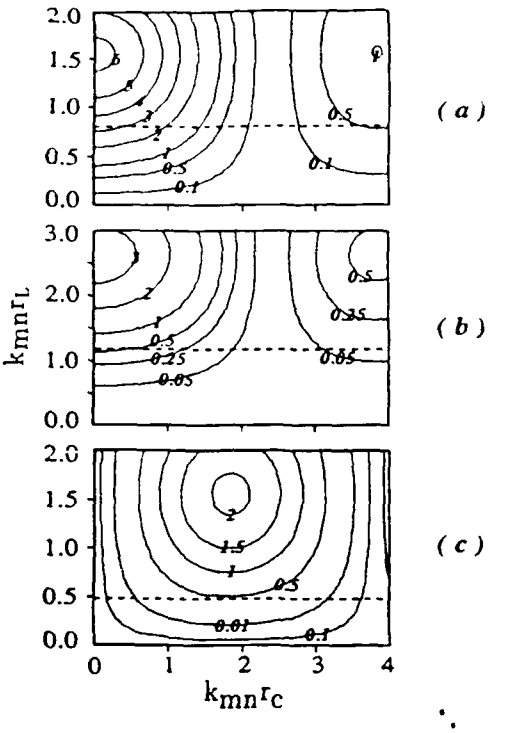

Fig. 3. Contour plot for coupling functions (a) H_{22}, (b) H_{33}, and (c) H_{21}. Absolute values of H_{sm}'s have been magnified by 100. Dashed line corresponds to 100 kV, $\alpha = 1$, and $B_0/B_g = 0.98$.

sth harmonic component of the TE_{mn} mode electric field seen by the electrons. Fig. 3 shows the contour plots of $H_{sm}(k_{mn}r_c, k_{mn}r_L)$ for the operating $TE_{21}^{(2)}$ mode and its two strongest competing oscillation modes, the $TE_{11}^{(2)}$ and $TE_{31}^{(3)}$, where the superscripts represent the cyclotron harmonic numbers. The dashed lines on the figures represent the electron Larmor radius corresponding to an axial magnetic field $B_0 = 0.98B_g$ for the operating $TE_{21}^{(2)}$ mode. Clearly, the positioning of the electron guiding center is extremely important, since it changes the relative interaction strength of all the modes. A properly placed beam will maximize the value of H_{sm} for the operating mode (H_{22} in this case), while minimizing the H_{sm}'s for all the other modes. Given an electron Larmor radius, Fig. 3(a) shows that H_{22} is maximum for an axis-encircling beam. For such a beam, H_{21} vanishes while H_{33} is about six times smaller than H_{22}. A $TE_{21}^{(2)}$ gyro-TWT amplifier design based upon this beam geometry has recently been developed with appreciable power, efficiency, and gain [17]. However, difficulties encountered in forming such a high-current axis-encircling beam with low velocity spread still need to be overcome.

As the beam moves away from the waveguide center so that it corresponds to the more common annular beam formed by a MIG, a much more mature technology, both H_{22} and H_{33} will decrease while H_{21} increases. Notice that H_{33} decreases more rapidly than H_{22} does, resulting in an increase in the ratio H_{22}/H_{33}. For the chosen ratio of guiding center radius to waveguide wall radius, $r_c/r_w = 0.4$, both H_{33} and H_{21} are at least one order of magnitude smaller than H_{22}.

The power evolution in the three-stage $TE_{21}^{(2)}$ gyro-TWT obtained from simulation is shown in Fig. 4 for three different input powers (0.5 W, 1.9 W, and 4 W). The length of each section has been chosen to be less than the critical length for $TE_{31}^{(3)}$ oscillation, which has been found to be the most threatening spontaneous oscillation [18]. As in a single-stage gyro-TWT amplifier, the output power saturates at shorter distance as the input power is increased. It is found that the electrons will suffer from overbunching if the input power is too strong, resulting in lower saturated output power [27]. Simulation results have indicated that it is easier to overdrive the electron beam in a multistage device because saturation occurs close to the sever in the last section. For the case shown in Fig. 4, the electron beam is highly overdriven when the input power is increased merely 3 dB from 1.9 W to 4 W.

Shown in Fig. 5 is the constant drive bandwidth of the second-harmonic gyro-TWT amplifier for several values of axial velocity spread ($\Delta v_z/v_z$ = 0, 3%, and 5%), where all parameters except the RF input signal frequency are held constant. The input power is set to the value at which the amplifier saturates at 35 GHz. Clearly, the beam axial velocity spread narrows the constant drive bandwidth. Whereas an ideal beam without a velocity spread gives a FWHM bandwidth of 7.1%, a beam with an axial velocity spread of 5% yields a FWHM bandwidth of 5.2%. Fig. 6 shows the predicted saturated bandwidth of the harmonic gyro-TWT amplifier design for several values of axial velocity spread. The saturated bandwidths were obtained for a fixed device length (40.5 cm) with varying input power such that the maximum power appeared at the output end of the amplifier. Again the FWHM bandwidth is reduced from 13% to 7.4% as the axial velocity spread increases from 0% to 5%. The velocity spread has its

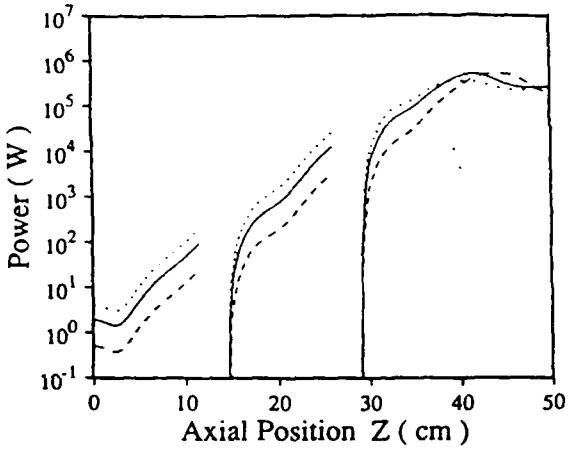

Fig. 4. Predicted spatial power profile of 35 GHz wave in proposed three-stage $TE_{21}^{(2)}$ gyro-TWT (Table II) for input powers of 0.5 W (dashed curve), 1.9 W (solid curve), and 4 W (dotted curve).

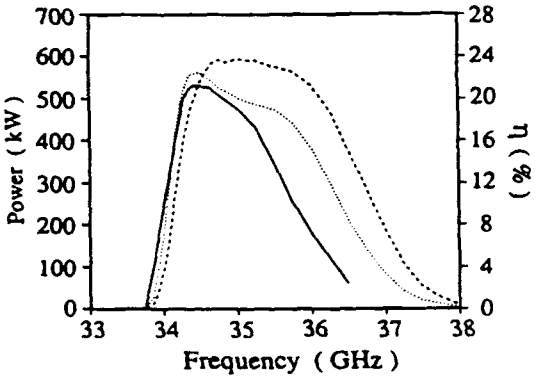

Fig. 5. Constant drive bandwidth of proposed three-stage $TE_{21}^{(2)}$ gyro-TWT (Table II) for axial velocity spreads of 0% (dashed curve), 3% (dotted curve), and 5% (solid curve).

greatest effect in the high-frequency region of the bandwidth. This is because the larger wave numbers associated with the higher frequencies yield a larger Doppler shift spread and therefore a greater mismatch of the beam–wave resonance condition. For the case of $\Delta v_z/v_z = 5\%$, a peak output power of 533 kW is predicted at 34.5 GHz, which is almost an order of magnitude higher than the power levels achieved by state-of-the-art fundamental gyro-TWT's. At 34.5 GHz, the peak efficiency and gain are 21.3% and 54 dB, respectively.

IV. Discussion and Conclusions

Although reducing the interaction length is a general, effective, and practical way to suppress all spontaneous oscillations in a high-power gyro-TWT, external feedback caused by reflections from poor input/output wave couplers, poor sever matching circuits, etc., could induce oscillation, rendering wave amplification impossible. These external reflections, however, have been neglected in the nonlinear simulations. The critical interaction length for oscillation can be expected to decrease for nonzero reflection coefficient, but the technique of using multiple stable sections to boost the gain is still

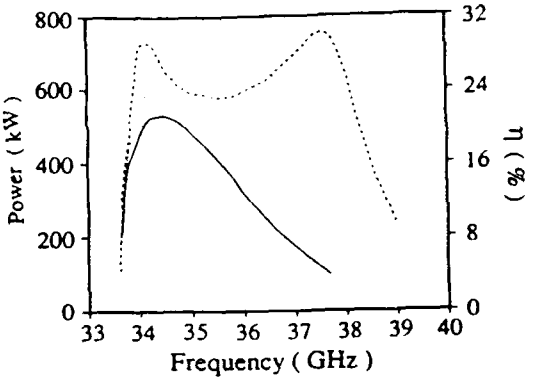

Fig. 6. Saturated bandwidth of proposed three-stage $TE_{21}^{(2)}$ gyro-TWT (Table II) for axial velocity spreads of 0% (dashed curve), 3% (dotted curve), and 5% (solid curve).

appropriate. To prevent oscillations from occurring, the sum of the return loss from each sever and its complement, a coupler or another sever, must be greater than the maximum gain per stage, which is approximately 20 dB for the three-stage gyro-TWT amplifier in Section III. Since it is fairly straightforward to build broadband couplers and attenuators with a return loss of over 10 dB, this constraint is not too demanding.

It is also assumed in developing the nonlinear theory that space charge effects can be neglected. This assumption will be valid for a single-stage device employing a low value of beam current. For the harmonic gyro-TWT amplifiers studied here, the validity of this assumption remains to be verified experimentally, as both high levels of beam current and multiple severs are required for stable high-power generation.

The validity of the theoretical prediction [17], [18] that harmonic gyro-TWT amplifiers can generate extremely high power in the millimeter-wave region has been demonstrated through a numerical design study. By limiting the length of each interaction section, a multistage device can be kept stable and still yield ample gain. It has also been shown that a MIG beam can be utilized with satisfactory performance. A 533 kW, 35 GHz, three-stage second-harmonic TE_{21} gyro-TWT amplifier with 21.3% efficiency and 7.4% bandwidth has been simulated numerically and will be constructed at UCLA. Further improvement of the performance of the designed harmonic gyro-TWT amplifier may be expected if enhancement schemes such as tapering the axial magnetic field [28], [29] and/or waveguide wall [5] are employed.

References

[1] V. L. Granatstein, P. Sprangle, M. Herndon, R. K. Parker, and S. P. Schlesinger, "Microwave amplification with an intense relativistic electron beam," *J. Appl. Phys.*, vol. 46, pp. 3800–3805, 1975.

[2] K. R. Chu, A. T. Drobot, V. L. Granatstein, and J. L. Seftor, "Characteristics and optimum operating parameters of a gyrotron travelling wave amplifier," *IEEE Trans. Microwave Theory Tech.*, vol. MTT-27, no. 2, pp. 178–187, 1979.

[3] J. L. Seftor, V. L. Granatstein, K. R. Chu, P. Sprangle, and M. E. Read, "The electron cyclotron maser as a high-power traveling wave amplifier of millimeter waves," *IEEE J. Quantum Electron.*, vol. QE-15, no. 9, pp. 848–853, 1979.

[4] L. R. Barnett, Y. Y. Lau, K. R. Chu, and V. L. Granatstein, "An experimental wide-band gyrotron traveling-wave amplifier," *IEEE Trans. Electron Devices*, vol. ED-28, no. 7, pp. 872–875, 1981

[5] G. S. Park *et al.*,"Experimental study of a broadband millimeter-wave gyrotron travelling wave amplifier," in *Tech. Dig., IEEE Int. Electron Devices Meeting* (Washington, DC), 1991, pp. 779–781.
[6] R. S. Symons, H. R. Jory, and S. J. Hegji, "An experimental gyro-TWT," in *Tech. Dig., IEEE Int. Electron Devices Meeting* (Washington, DC), 1979, p. 676.
[7] P. Ferguson and R. S. Symons, "A C-band gyro-TWT," in *Tech. Dig., IEEE Int. Electron Devices Meeting* (Washington, DC), 1980, pp. 310–313.
[8] P. Ferguson, G. Valier, and R. S. Symons, "Gyrotron-TWT operating characteristics," *IEEE Trans. Microwave Theory Tech.*, vol. MTT-29, pp. 794–799, Aug. 1981.
[9] V. L. Granatstein and S. Y. Park, "Survey of recent gyrotron developments," in *Tech. Dig., IEEE Int. Electron Devices Meeting* (Washington, DC), 1983, pp. 263–266.
[10] K. R. Chu, L. R. Barnett, W. K. Lau, L. H. Chang, and C. S. Kou, "Recent developments in millimeter wave gyro-TWT research at NTHU," in *Tech. Dig., IEEE Int. Electron Devices Meeting* (San Francisco), 1990. pp. 699–702.
[11] W. W. Destler, R. Kulkarni, C. D. Striffler, and R. L. Weiler, "Microwave generation from rotating electron beams in magnetron-type waveguides," *J. Appl. Phys.*, vol. 54, no. 7, pp. 4152–4162, 1983.
[12] W. Namkung, "Observation of microwave generation from a cusptron device," *Phys. Fluids*, vol. 27, no. 2, pp. 329–330, 1984.
[13] D. B. McDermott, N. C. Luhmann, Jr., D. S. Furuno, A. Kupiszewski, and H. R. Jory, "Observation of a millimeter-wave harmonic gyrotron," *Int. J. Infrared and Millimeter Waves*, vol. 4, no. 4, pp. 639–664, 1983.
[14] D. S. Furuno *et al.*, "A four cavity, high harmonic gyroklystron amplifier," *Int. J. Electron.*, vol. 65, no. 3, pp. 429–435, 1988.
[15] D. S. Furuno, D. B. McDermott, C. S. Kou, N. C. Luhmann, Jr., and P. Vitello, "Theoretical and experimental investigation of high harmonic gyro-travelling-wave-tube amplifier," *Phys. Rev. Lett.*, vol. 62, no. 11, pp. 1314–1317, 1989.
[16] D. S. Furuno *et al.*, "Operation of a large-orbit high-harmonic gyro-traveling-wave tube amplifier," *IEEE Trans. Plasma Sci.*, vol. 18, no. 3, pp. 313–320, 1990.
[17] A. T. Lin *et al.*, "Marginal stability design criterion for gyro-TWT's and comparison of fundamental with second harmonic operation," *Int. J. Electron.*, to be published.
[18] C. S. Kou *et al.*, "High-power harmonic gyro-TWT's—Part I: Linear theory and oscillation study," *IEEE Trans. Plasma Sci.*, pp. 155–162, this issue.
[19] G. P. Scheitrum, R. S. Symons and R. B. True, "Low velocity spread axis encircling electron beam forming system," *Tech. Dig., IEEE Int. Electron Devices Meeting* (Washington, DC), 1989, pp. 743–746.
[20] J. M. Baird and W. Lawson, "Magnetron injection gun (MIG) design for gyrotron applications," *Int. J. Electron.*, vol. 61, no. 6, pp. 953–967, 1986.
[21] A. W. Fliflet, "Linear and nonlinear theory of the Doppler-shifted cyclotron resonance maser based on TE and TM waveguide modes," *Int. J. Electron.*, vol. 61, no. 6, pp. 1049–1080, 1986.
[22] A. K. Ganguly, S. Ahn, and S. Y. Park, "Three dimensional nonlinear theory of the gyropeniotron amplifier," *Int. J. Electron.*, vol. 65, no. 3, pp. 597–618, 1988.
[23] A. K. Ganguly and S. Ahn, "Large-signal theory of a two-stage wideband gyro-TWT," *IEEE Trans. Electron Devices*, vol. ED-31, no. 4, pp. 474–480, 1984.
[24] A. K. Ganguly and S. Ahn, "Non-linear analysis of the gyro-BWO in three dimensions," *Int. J. Electron.*, vol. 67, no. 2, pp. 261–276, 1989.
[25] K. R. Chu, "Theory of electron cyclotron maser interaction in a cavity at the harmonic frequencies," *Phys. Fluids*, vol. 21, no. 12, 1978.
[26] A. T. Lin and C. C. Lin, "Stabilization of the absolute instability in cyclotron autoresonance maser amplifier by a drive wave," *Phys. Fluids B*, vol. 1, no. 11, pp. 2286–2288, 1989.
[27] C. S. Kou, "Design procedure for a stable high power gyro-TWT," Ph.D. dissertation, Dept. of Electrical Engineering, Univ. of Calif. Los Angles, 1991.
[28] K. D. Pendergast, B. G. Danly, R. J. Temkin, and J. S. Wurtele, "Self-consistent simulation of cyclotron autoresonance maser amplifiers," *IEEE Trans. Plasma Sci.*, vol. PS-16, pp. 122–128, 1988.
[29] Q. S. Wang *et al.* "CARM amplifier designs for high power," *Int. J. Infrared and Millimeter Waves*, vol. 12, no. 4, pp. 297–322, 1991.

Q. S. Wang, photograph and biography not available at the time of publication.

C. S. Kou, photograph and biography not available at the time of publication.

D. B. McDermott (M'83), photograph and biography not available at the time of publication.

A. T. Lin, photograph and biography not available at the time of publication.

K. R. Chu (SM'82), photograph and biography not available at the time of publication.

N. C. Luhmann, Jr., photograph and biography not available at the time of publication.

A.4. Bragg Reflectors

Bragg Reflectors

C. K. Chong, D. B. McDermott, *Member, IEEE*, M. M. Razeghi, N. C. Luhmann, Jr., J. Pretterebner, D. Wagner, M. Thumm, M. Caplan, and B. Kulke, *Member, IEEE*

Abstract—**A Bragg reflector composed of periodic cylindrically symmetric corrugations can provide a reflection of nearly unity through the principles of constructive interference, allowing the formation of a frequency selective resonator. Mode conversion will occur, but can be reduced by tapering the amplitude of the corrugations. Reflection measurements are compared with theoretical predictions for untapered sinusoidal and rectangular corrugation as well as a reflector tapered according to the Hamming-window prescription. Measurements of Bragg resonators are also presented.**

I. Introduction

A Bragg resonator is the most suitable cavity structure for providing frequency selective feedback for overmoded, high-power oscillators such as the cyclotron autoresonance maser (CARM) [1] and the free electron laser (FEL) [2]. It can be obtained from corrugated waveguide as shown in Fig. 1. A Bragg resonator also allows good beam transport. Since the corrugation amplitude can be quite small, the path for the electron beam is unobstructed. The corrugation scatters a forward wave coherently into a backward wave if the period satisfies the Bragg condition

$$2k = k_b, \tag{1}$$

where k is the axial propagation constant of the wave, $k_b = 2\pi/l$, and l is the corrugation period. A resonator comprising two Bragg reflectors separated by a smooth tube as in Fig. 1 can have a high quality factor ($Q > 1000$) for a frequency satisfying the Bragg condition.

A characteristic of a Bragg reflector is that it can also convert the mode of a wave, especially if two modes are close in frequency for the axial wave vector which satisfies the Bragg condition. Our mode of interest is the TE_{11} mode, the lowest order mode of cylindrical waveguide. The four nearest modes are the TE_{21}, TE_{01}, TM_{01}, and TM_{11} modes. Because our corrugation geometry is cylindrically symmetric, the azimuthal mode number cannot change during conversion; therefore the TE_{11} mode will not couple to the TE_{21}, TE_{01}, or TM_{01} modes, but it does to the TM_{11} mode. If these two modes are close in frequency, then strong parasitic intercoupling can occur between them. This places an upper limit on the corrugation amplitude for a given corrugation geometry.

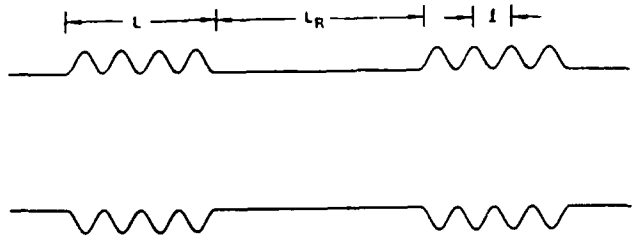

Fig. 1. Schematic of Bragg resonator with sinusoidal corrugation.

The organization of this paper is as follow. In Section II, the theory and measurement of Bragg reflectors are given. It is shown that tapering the corrugation can dramatically improve the mode quality. The theory and measurement of Bragg resonators are presented in Section III, and Section IV contains the final discussion and conclusions.

II. Reflector

A. Theory

The general case of a waveguide whose cross section varies smoothly along the axis has been treated by Solymar [3], who formulated the set of coupled equations for the wave amplitudes of the forward and backward propagating waves, namely the generalized telegraphist's equation. From this equation, under the assumption of a weak sinusoidal corrugation one can derive either a set of coupled differential equations, where all modes are assumed to be isolated from the other modes, or a more exact set of multicoupled differential equations, where the modes are allowed to intercouple. By solving the uncoupled and coupled differential equations, the behavior of sinusoidal corrugation Bragg reflectors can be examined as well as the basic characteristics of a Bragg reflector with general corrugation geometry.

1) Single Mode: Throughout, we will consider TE_{mn} and TM_{mn} modes whose fields satisfy

$$f(z,t) = A(z)e^{i(\omega t - kz)}. \tag{2}$$

We will assume a slow variation of the amplitude such that

$$k \gg \left|\frac{1}{A}\frac{dA}{dz}\right|. \tag{3}$$

Manuscript received October 1, 1991; revised January 30, 1992. This work was supported by the Rome Air Development Center (ATRI) under Contract F30602-91-C-0200, by ARO under Contract DAAL03-91-K-0190, by AFOSR under Grant 89-0005, by ONR under Contract N00014-87-K-2032 through NRL, and by DOE under Contract W-7405-ENG-48 through the Lawrence Livermore National Laboratory.

C. K. Chong, D. B. McDermott, M. M. Razeghi, and N. C. Luhmann, Jr., are with the Department of Electrical Engineering, University of California at Los Angeles, Los Angeles, CA 90024.

J. Pretterebner and D. Wagner are with the Institute for Plasma Research, University of Stuttgart, Stuttgart, Germany.

M. Thumm is with the Institute for High Frequency Electronics, University of Karlsruhe and the Institute for Technical Physics, KFK Karlsruhe, Karlsruhe, Germany.

M. Caplan and B. Kulke are with the Lawrence Livermore National Laboratory, Livermore, CA 94550.

IEEE Log Number 9108097.

We will also assume cylindrical geometry with a weak axisymmetric sinusoidal ripple in the waveguide wall, so that the radial profile follows

$$h(z) = a + h\cos(k_b z), \tag{4}$$

where a is the mean radius and the corrugation amplitude h satisfies $h \ll a$. For the single-mode case, the coupled equations for the forward (A^+) and backward (A^-) wave amplitudes are

$$\frac{dA^+}{dz} = -(\alpha + i\Delta)A^+ - iGA^- \tag{5}$$

and

$$\frac{dA^-}{dz} = (\alpha + i\Delta)A^- + iGA^+, \tag{6}$$

where $\Delta = k - k_b/2$ is the Bragg mismatch, $k = ((\omega/c)^2 - (x_{mn}/a)^2)^{1/2}$ is the axial wave vector, x_{mn} represent the zeros of the Bessel functions (TM) and their first derivatives (TE), a is the wall radius, α is the ohmic dissipation loss constant (it is usually a good approximation to let $\alpha = 0$), and G is the wave coupling coefficient. The reflectivity for a single section reflector can be obtained analytically [4] for the boundary conditions

$$A^+(0) = 1 \tag{7}$$

and

$$A^-(L) = 0, \tag{8}$$

where the origin is taken to be at one end of the reflector of length L. The reflectivity is found to be

$$R \equiv |A^-(0)/A^+(0)|^2 = \left| \frac{G\sinh\gamma L}{(\alpha + i\Delta)\sinh\gamma L + \gamma\cosh\gamma L} \right|^2, \tag{9}$$

where $\gamma^2 = G^2 + (\alpha + i\Delta)^2$.

Fig. 2 shows the predicted reflection coefficient from (9) for a single-section reflector as a function of Bragg mismatch normalized to the coupling coefficient. As one can see from the figure, the bandwidth is directly proportional to the coupling coefficient and therefore is inversely proportional to the length of the corrugation section for a fixed reflectivity (fixed GL). Thus, for a narrower bandwidth reflector with a specific desired reflectivity, one should reduce the corrugation amplitude and increase the length of the reflector (i.e., fix GL and decrease G/L).

2) Multimode: In a given Bragg reflector, all modes satisfy the Bragg condition at some frequency. In addition, the corrugation can couple a mode to other modes if the two waves satisfy the Bragg condition

$$k_1 + k_2 = k_b \tag{10}$$

and the symmetry allows it. The most general set of equations for the multicoupled case is

$$\frac{dA_j^+}{dz} = -(\alpha_j + i\Delta_j)A_j^+ - i\sum_i G_{ji}A_i^- \tag{11}$$

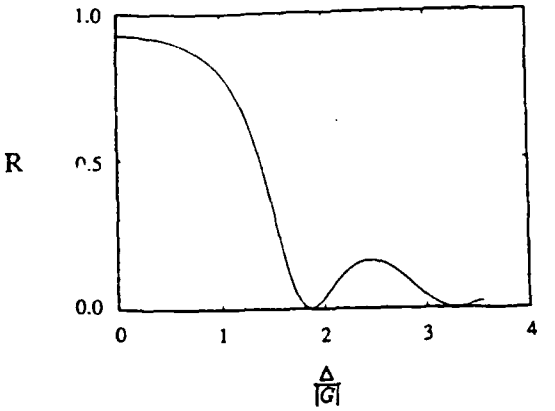

Fig. 2. Reflection coefficient from uncoupled mode theory for a section of corrugated waveguide with $GL = 2$ versus Bragg resonance mismatch.

and

$$\frac{dA_j^-}{dz} = (\alpha_j + i\Delta_j)A_j^- + i\sum_i G_{ji}A_i^+, \tag{12}$$

where the subscript refers to the various transverse modes and G_{ij} is the wave coupling coefficient tensor.

Since our mode of interest is the TE_{11} mode, we will confine the rest of the analysis to just the TE_{11} and TM_{11} modes. Then the general equations for the multicoupled case reduce to four first-order linear equations (H representing TE_{11} and E representing TM_{11}):

$$\frac{dA_H^+}{dz} = -(\alpha_H + i\Delta_H)A_H^+ - iG_H A_H^- - iG_X A_E^- \tag{13}$$

$$\frac{dA_H^-}{dz} = (\alpha_H + i\Delta_H)A_H^- + iG_H A_H^+ + iG_X A_E^+ \tag{14}$$

$$\frac{dA_E^+}{dz} = -(\alpha_E + i\Delta_E)A_E^+ - iG_E A_E^- - iG_X A_H^- \tag{15}$$

and

$$\frac{dA_E^-}{dz} = (\alpha_E + i\Delta_E)A_E^- + iG_E A_E^+ + iG_X A_H^+, \tag{16}$$

where again Δ_H and Δ_E represent the Bragg mismatches for the TE_{11} and TM_{11} modes, respectively, and G_H, G_E, and G_X are the wave coupling coefficients for $TE_{11} - TE_{11}$, $TM_{11} - TM_{11}$, and $TE_{11} - TM_{11}$ conversion, respectively. The general coupling coefficients for sinusoidal corrugation are given by [5]

$$G_H = \frac{h}{2a^3}\frac{(-x_{mn}^2 x_{m'n'}^2 + mm'a^2(\omega^2/c^2 + kk'))}{(kk')^{1/2}((x_{mn}^2 - m^2)(x_{m'n'}^2 - m'^2))^{1/2}} \tag{17}$$

for the coupling of TE_{mn} with $TE_{m'n'}$ modes,

$$G_E = \frac{h}{2a}\frac{(\omega^2/c^2 + kk')}{(kk')^{1/2}} \tag{18}$$

for the coupling of TM_{mn} with $TM_{m'n'}$ modes, and

$$G_X = \frac{h}{2a}\frac{m(\omega/c)}{(x_{mn}^2 - m^2)^{1/2}}\frac{(\cdot + k')}{(kk')^{1/2}} \tag{19}$$

for the coupling of TE_{mn} with $TM_{m'n'}$ modes. If the operating frequency is much greater than the cutoff frequency, the

coupling coefficients can be simplified as

$$G_H = 0.42\frac{h}{a}\frac{\omega}{c} \tag{20}$$

for the TE_{11} mode,

$$G_E = \frac{h}{a}\frac{\omega}{c} \tag{21}$$

for the TM_{11} mode, and

$$G_X = 0.65\frac{h}{a}\frac{\omega}{c} \tag{22}$$

for the intercoupling resonance. From (17)–(19) or (20)–(22), one can observe that the coupling strength is proportional to the normalized corrugation amplitude h/a.

Athough we cannot obtain a simple closed-form solution of the four coupled equations, a numerical solution can be obtained for the wave amplitudes by using the eigenvalue/eigenvector method. The four coupled equations can be expressed in vector form as shown in (23), at the bottom of the page. Letting the amplitudes satisfy $A \propto e^{\lambda z}$, where λ is a complex constant, one can express the coupled vector differential equations as a compact 4×4 matrix eigenvalue problem given by

$$(\mathcal{M} - \lambda\mathcal{I})\vec{e} = \vec{0}, \tag{24}$$

where $\mathcal{M}$ is the 4×4 matrix on the RHS of (23), λ is an eigenvalue, $\vec{e}$ is the corresponding eigenvector, $\mathcal{I}$ is the 4×4 identity matrix, and $\vec{0}$ is the zero vector. One can recognize that (24) is in the familiar eigenform and therefore the eigenvalues and eigenvectors can straightforwardly be obtained.

Once the eigenvalues and eigenvectors have been found, the amplitude vector $\vec{A}$ at any position of the corrugation section can be expressed as a linear combination of the four eigenvectors as

$$\vec{A} = \sum_{i=1}^{4} K_i \vec{e}_i e^{\lambda_i z}, \tag{25}$$

where K_i are constants to be found by satisfying the boundary condition. The equations have been solved for the boundary conditions

$$A_H^+(0) = 1(0) \tag{26}$$

$$A_E^+(0) = 0(1) \tag{27}$$

$$A_H^-(L) = 0(0) \tag{28}$$

and

$$A_E^-(L) = 0(0) \tag{29}$$

TABLE I
CORRUGATION REFLECTOR PARAMETERS

Case	250 GHz (a)	10.6 GHz (b)	10.6 GHz (c)
Period	0.603 mm	1.575 cm	1.575 cm
Mean radius	3.525 mm	1.809 cm	1.809 cm
Corrugation amplitude	0.026 mm	0.210 cm	0.203 cm
Corrugation length	18.09 cm	46.86 cm	31.50 cm
ω/ω_c	10	2.2	2.2
Corrugation profile	constant	constant	constant
Corrugation geometry	sinusoidal	sinusoidal	rectangular

for $TE_{11}(TM_{11})$ input.

Using this analytical theory, the reflectivity characteristics of sinusoidal corrugation have been examined. The reflectivity for TE_{11} and TM_{11} modes is given by

$$R_H = \left|A_H^-(0)\right|^2 \tag{30}$$

and

$$R_E = \left|A_E^-(0)\right|^2. \tag{31}$$

Similarly, the transmission through the reflector is given by

$$T_H = \left|A_H^+(L)\right|^2 \tag{32}$$

and

$$T_E = \left|A_E^+(L)\right|^2. \tag{33}$$

Fig. 3(a) shows the reflection characteristics for TE_{11} input from a sinusoidal corrugation Bragg reflector with the parameters listed in Table I (case (a)). This reflector was built at the Lawrence Livermore National Laboratory (LLNL) for a 250 GHz CARM oscillator experiment [6], [7]. If the amplitude is increased from the value in Fig. 3(a), the reflectivity in the TE_{11} mode actually decreases because the resonances begin to overlap and interfere with one another. Notice in Fig. 3(b) that intercoupling destroys the performance of the reflector for a large corrugation amplitude. The reflectivity for TM_{11} mode input for the same reflector is shown in Fig. 3(c). Notice that the $TE_{11} - TM_{11}$ intercoupling resonance occurs at the same frequency in Fig. 3(c) as in Fig. 3(a), as would be expected from reciprocity. It is observed in Fig. 3(d) that the mode purity of the TM_{11} mode is also degraded as a result of overlap with the $TE_{11} - TM_{11}$ intercoupling resonance for a large corrugation amplitude.

The maximum allowable corrugation amplitude for a high mode purity reflector is determined by the need

$$\frac{d}{dz}\begin{pmatrix} A_H^+ \\ A_H^- \\ A_E^+ \\ A_E^- \end{pmatrix} = \begin{pmatrix} -(\alpha_H + i\Delta_H) & -iG_H & 0 & -iG_X \\ iG_H & (\alpha_H + i\Delta_H) & iG_X & 0 \\ 0 & -iG_X & -(\alpha_E + i\Delta_E) & -iG_E \\ iG_X & 0 & iG_E & (\alpha_E + i\Delta_E) \end{pmatrix}\begin{pmatrix} A_H^+ \\ A_H^- \\ A_E^+ \\ A_E^- \end{pmatrix} \tag{23}$$

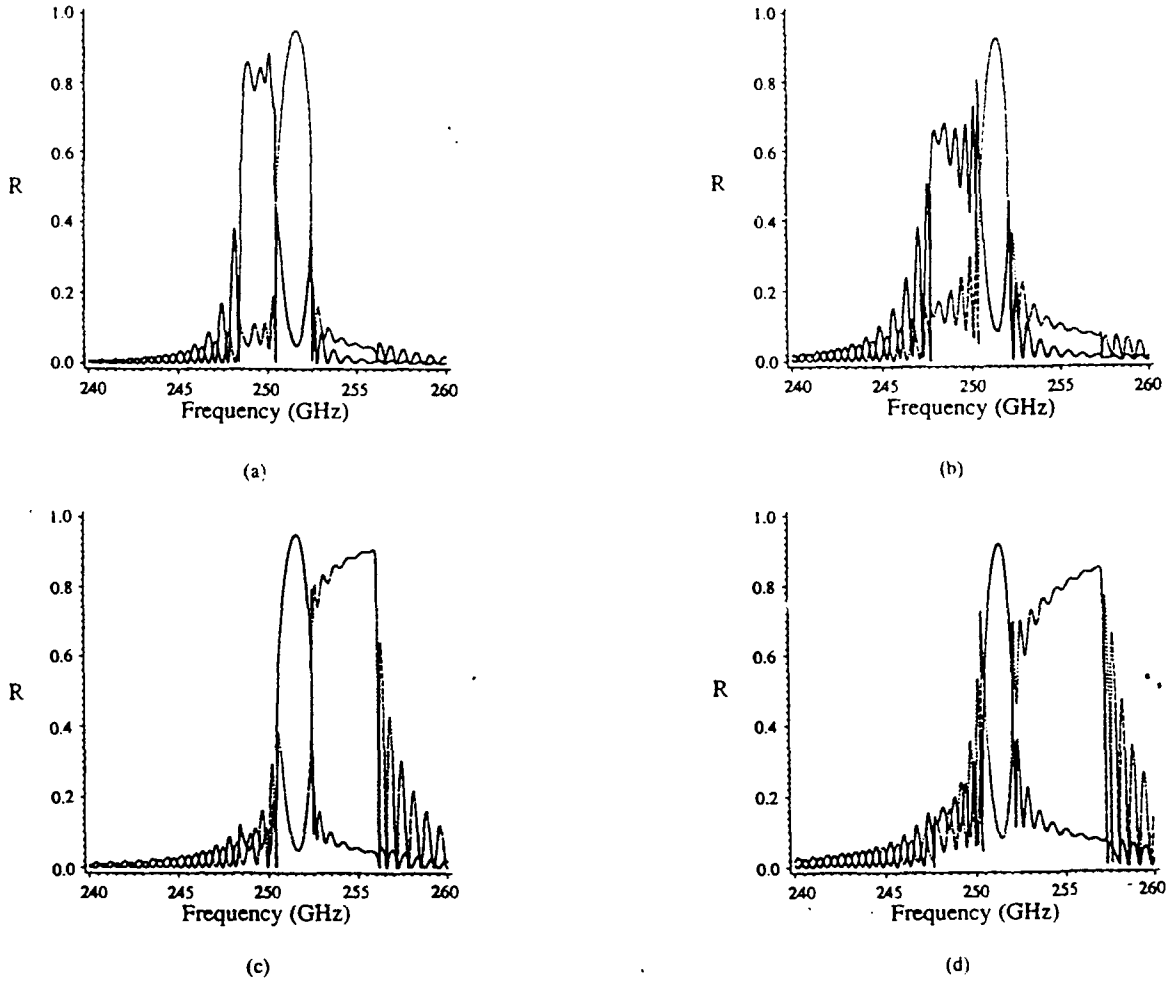

Fig. 3. Dependence on frequency of reflection in TE_{11} (solid line) and TM_{11} (dashed line) modes from sinusoidal corrugation reflector with parameters otherwise corresponding to those in Table I, case (a), with corrugation amplitudes of (a) 0.026 mm and (b) 0.039 mm for TE_{11} mode input and (c) 0.026 mm and (d) 0.039 mm for TM_{11} mode input

to minimize the overlap of the nearest intercoupling resonance with the desired Bragg resonance. The frequency separation between the two modes must be at least greater than the sum of the half-widths of each resonance. For the case of interest and using $\Delta k = 3G$ as the full width (see Fig. 2), small mode overlap requires

$$\omega_X - \omega_H \geq (3/2)c(|G_H| + |G_X|), \tag{34}$$

where ω_H and ω_X are the center frequencies of the pure TE_{11} and $TE_{11} - TM_{11}$ resonances, respectively. Multiplying both sides by $(\omega_X + \omega_H) \simeq 2\omega_H$, we obtain the condition

$$\omega_X^2 - \omega_H^2 \geq 3\omega_H c(|G_H| + |G_X|). \tag{35}$$

By using the dependence of frequency on the cutoff frequency and propagation constant, it can be shown that

$$\omega_X^2 - \omega_H^2 = \frac{3(\omega_{cE}^2 - \omega_{cH}^2)}{4}, \tag{36}$$

where ω_{cE} and ω_{cH} are the cutoff frequency of the TM_{11} and TE_{11} modes, respectively. Substituting (20), (22) and (36) into (35) and expressing ω_{cE} in terms of ω_{cH}, we find that the maximum allowable corrugation amplitude is determined by the condition

$$h/a \leq 0.78(\omega_{cH}/\omega)^2. \tag{37}$$

It is evident that the further the device is operated above cutoff, the smaller the maximum allowable corrugation amplitude.

Bragg reflectors are designed by setting the corrugation amplitude to a value at which the resonances are well separated and then choosing the length of the reflector to obtain the desired reflection. Fig. 4 shows the dependence on length of Bragg reflection for the 250 GHz LLNL Bragg reflector as predicted by the coupled mode theory. Reducing the corrugation amplitude further would yield a smaller fraction in the TM_{11} mode.

3) Scattering Matrix Code: Since the frequency selectivity of a Bragg reflector depends only on the axial periodicity of the waveguide wall perturbation, the corrugation geometry, in general, can be chosen arbitrarily. However, the previous analytical theory, which assumed a slow and weakly varying

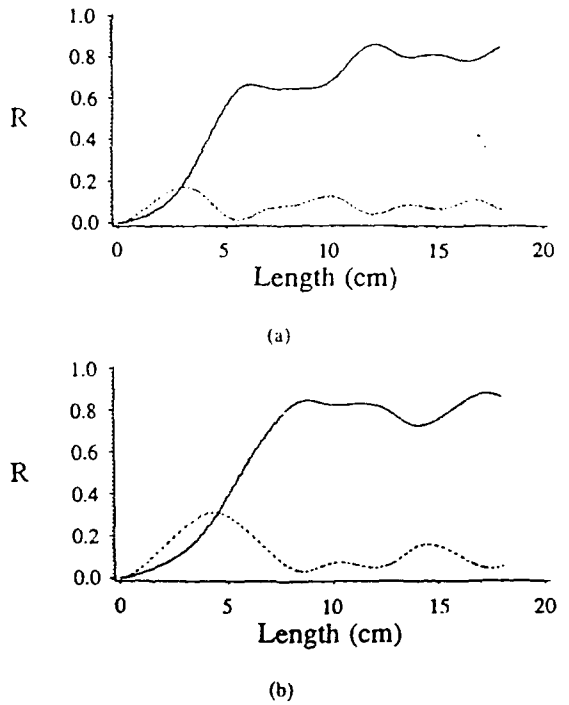

Fig. 4. Dependence on corrugation length of reflection at (a) 249 GHz and (b) 250 GHz in TE_{11} (solid lines) and TM_{11} modes (dashed lines) from sinusoidal corrugation reflector (Table I, case (a)). The injected wave is in TE_{11} mode.

corrugation, is not truly appropriate for a Bragg reflector with step discontinuities. To study the reflectivity characteristics of rectangular corrugation reflectors, in lieu of determining the correct coupling coefficients, a numerical scattering matrix simulation is used. The scattering matrix method [8], [9] is a multimode formulation where many propagating modes are included as well as the evanescent modes. Inclusion of the evanescent modes is especially important when they propagate as real waves in the corrugation vanes.

In this approach, the waveguide is decomposed into a discrete number of modules, corresponding to the number (minus one) of radial discontinuities. Each consists of an abrupt junction of two circular waveguides with different diameters. If the reflector is externally excited in the fundamental TE_{11} mode, the complete set of eigenfunctions for each module is represented by the forward and backward traveling and evanescent cylindrical waveguide TE_{1n} and TM_{1n} modes. Each TE_{1n} or TM_{1n} wave incident on a discontinuity excites an infinite sum of transmitted and reflected TE_{1n} and TM_{1n} waves as determined by the coupling coefficients at the interface. Truncation of this system for the numerical evaluation leads to the individual scattering matrix of each corrugation module.

The complete scattering matrix for the entire reflector is determined by repetitively cascading the modules. Finite conductivity is included in the computer code to model the performance of the Bragg reflector accurately. Since the fields in each module are expressed by a sum of the eigenfunctions of smooth waveguide with a constant radius, rectangular corrugation is the most convenient geometry for this calculation. However, this method can be extended to the simulation of any periodic form by dividing a corrugation

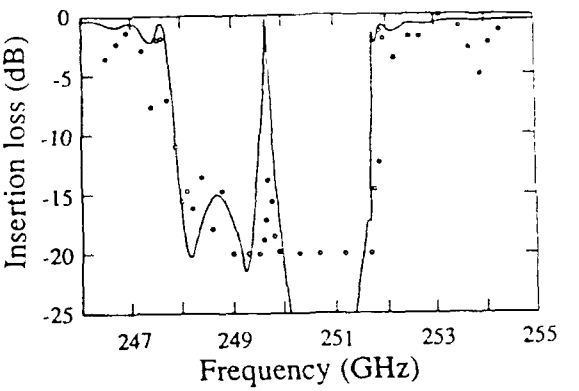

Fig. 5. Frequency dependence of insertion loss through sinusoidal corrugation reflector (Table I, case (a)) of TE_{11} mode from two-mode theory (solid line) and measurement (circles).

with an arbitrary shape into many small steps of rectangular discontinuities to approximate the particular geometry.

B. Measurement

Three sets of constant-corrugation-amplitude Bragg reflectors have been fabricated and tested. Two sets of Bragg reflectors designed for 10.6 GHz with $\omega/\omega_c = 2.2$ were built and tested at UCLA and another set designed for 250 GHz with $\omega/\omega_c = 10$ was built and tested at LLNL. All three sets were electroformed with copper. The inner surfaces of the UCLA reflectors were plated with gold to avoid oxidation during the test measurement phase.

The insertion loss of the 250 GHz sinusoidal corrugation reflector specified by Table I (case (a)) was measured by attaching a tunable source to the reflector through a down-taper to fundamental rectangular waveguide. The other end of the corrugation section was left open. The transmitted signal was picked up by a horn and measured with a large dynamic range heterodyne receiver. The measured insertion loss is shown in Fig. 5 and should be compared with the predicted transmissivity from the analytical coupled mode theory also shown in Fig. 5. The resonance at 248.8 GHz is due to pure TE_{11} coupling and the resonance at 250.7 GHz is from $TE_{11} - TM_{11}$ intercoupling. The measurements are in good agreement with the theoretical predictions including the small gap between the desired $TE_{11} - TE_{11}$ resonance and the destructive $TE_{11} - TM_{11}$ intercoupling resonance. Even though the reflector was designed for a large overmoded value of $\omega/\omega_c = 10$, the mode overlap is at a tolerable level because of the corrugation's small amplitude.

The return loss of each UCLA Bragg reflector was measured with an HP 8720A automated vector network analyzer. The measurement setup is shown is Fig. 6. A down-taper is attached to one end, followed by a circular to TE_{10} rectangular waveguide transformer, while the other end is left open. For frequencies within the design bandwidth, the converted TM_{11} mode will be cut off in the down-taper. Neglecting interference effects, the total reflected power picked up by the receiver can

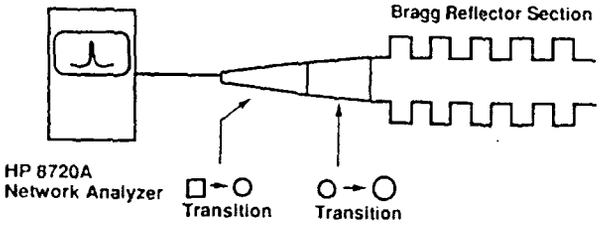

Fig. 6. Schematic diagram of the UCLA measurement setup to determine the Bragg reflection coefficient (S_{11}).

be expressed as

$$R_{\mathrm{TOTAL}} = R_H + R_X^2 \sum_{i=0}^{\infty} [R_E]^i, \tag{38}$$

where R_H and R_E are the single pass reflection from TE_{11} and TM_{11} modes, respectively, R_X is the mode conversion between TE_{11} and TM_{11} modes, and R_{TOTAL} is the the total reflected power into the TE_{11} mode.

Fig. 7(a) shows the predicted reflectivity from the analytical coupled mode theory for the sinusoidal corrugation reflector specified in Table I (case (b)). The measurement of the return loss (S_{11}) for this reflector is shown in Fig. 7(b) and should be compared with the solid line in Fig. 7(a), which includes the effect of multiple reflection (eq. (38)). The agreement of the measurement with the theoretical prediction is fairly good except that the experimental bandwidth is 25% broader than the theoretical prediction.

The Bragg reflector's corrugation need not be sinusoidal. A reflector was also built and tested with a rectangular profile. Fig. 8(a) shows the theoretical reflectivity of the rectangular corrugation reflector specified by Table I (case (c)) as predicted by the scattering matrix simulation code. Once again, the solid curve includes the effect of multiple reflection. The measurements of this reflector are shown in Fig. 8(b). Notice that the 10.5–12.5 GHz $\mathrm{TE}_{11} - \mathrm{TM}_{11}$ intercoupling resonance interferes with the desired $\mathrm{TE}_{11} - \mathrm{TE}_{11}$ coupling resonance at 9.5–11 GHz, as predicted by the scattering matrix simulation. The experimental results are in very good agreement with the scattering matrix simulation results, including the bandwidth of the two resonances. However, the analytical theory (Fig. 8(c)) using the larger ($\times 4/\pi$) equivalent fundamental sinusoidal corrugation amplitude obtained from Fourier decomposition, which does not include the cutoff modes in the analysis, failed to predict the extended bandwidth below the cutoff frequency for the TM_{11} mode (10.1 GHz) as well as the stronger coupling characteristics of the rectangular corrugation.

C. Hamming-Window

From the simulation results for the previous constant-amplitude corrugation reflectors, we have observed that the side lobes of the intercoupling resonance destroys the mode purity of the pure $\mathrm{TE}_{11} - \mathrm{TE}_{11}$ resonance. The problem of undesirable side lobes can be reduced by tapering the corrugation amplitude profile as prescribed by a Hamming-window distribution [10], a common technique in filter theory

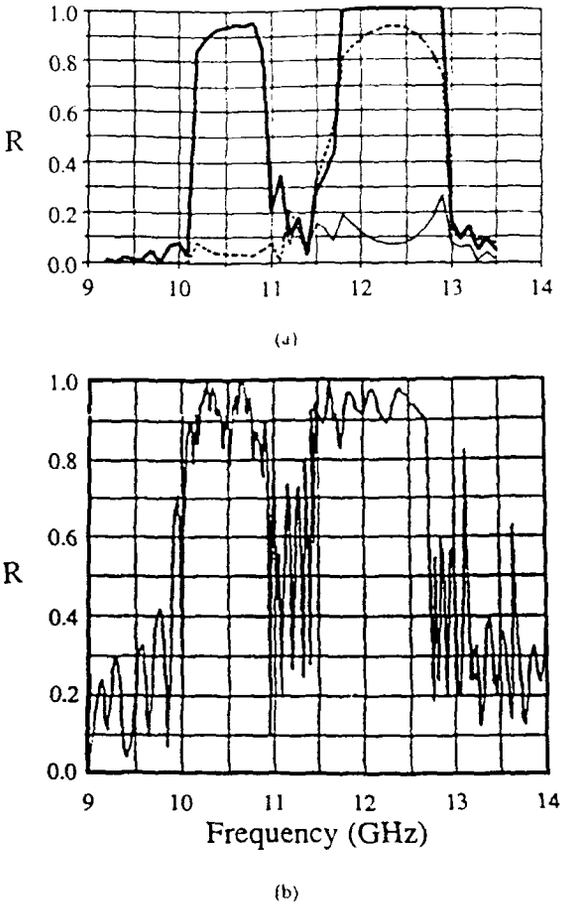

Fig. 7. Frequency dependence of reflection from sinusoidal corrugation reflector (Table I, case (b)) (a) in TE_{11} (thin line) and TM_{11} (dashed line) modes from two-mode theory including total theoretical TE_{11} reflection (dark line) from multiple reflections and (b) from measurement. The input wave is in the TE_{11} mode.

to suppress the side lobes of a filter's response. The envelope of the Hamming-window amplitude distribution is a modified raised cosine distribution given by

$$h(z) = h_0(0.54 - 0.46\cos(2\pi z/L)). \tag{39}$$

where $h(z)$ is the amplitude of the corrugation at position z (distance being measured from the beginning of the reflector of length L) and h_0 is the peak amplitude of the corrugation.

We have tested the reflectivity of two Hamming-window Bragg reflectors with rectangular corrugation for the gun and collector ends of the cavity for a planned 400 kV CARM oscillator experiment at 10.6 GHz ($\omega/\omega_c = 2.2$) [11]. They were also electroformed with copper. We have chosen rectangular corrugation for our Hamming-window reflector because the rectangular geometry is mechanically easier to fabricate than the curved surfaces of sinusoidal corrugation and the change from untapered to tapered amplitude profile in the scattering matrix formulation is a relatively straightforward modification. The corrugation orientation of our Hamming-window reflectors is positive ($h(z) \geq 0$) to avoid creating a high-Q cavity at the cutoff frequency. The positive corrugation also provides a larger open passage for the electron beam to

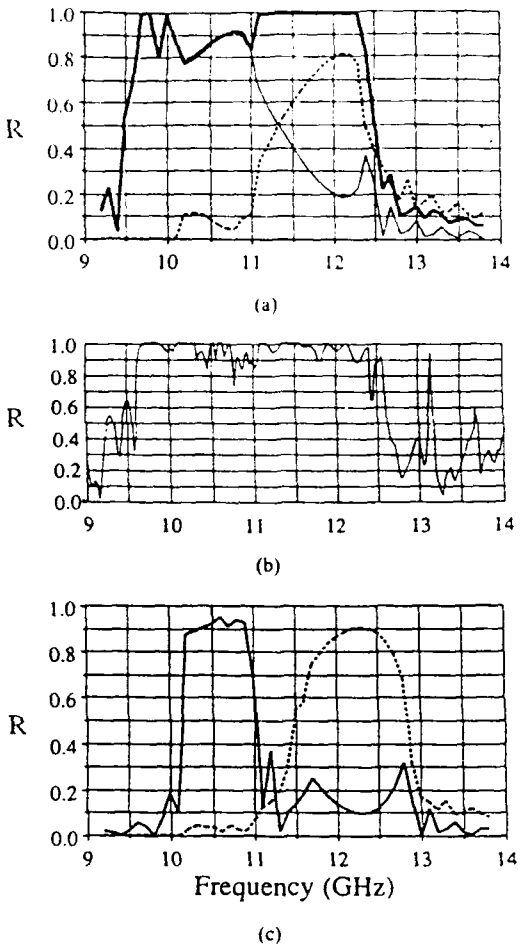

Fig. 8. Frequency dependence of reflection from rectangular corrugation reflector (Table I, case (c)) (a) in TE_{11} (thin line) and TM_{11} (dashed line) modes from scattering matrix simulation including total TE_{11} reflection (dark line) from multiple reflections, (b) from measurement, and (c) from two-mode theory. The input wave is in TE_{11} mode.

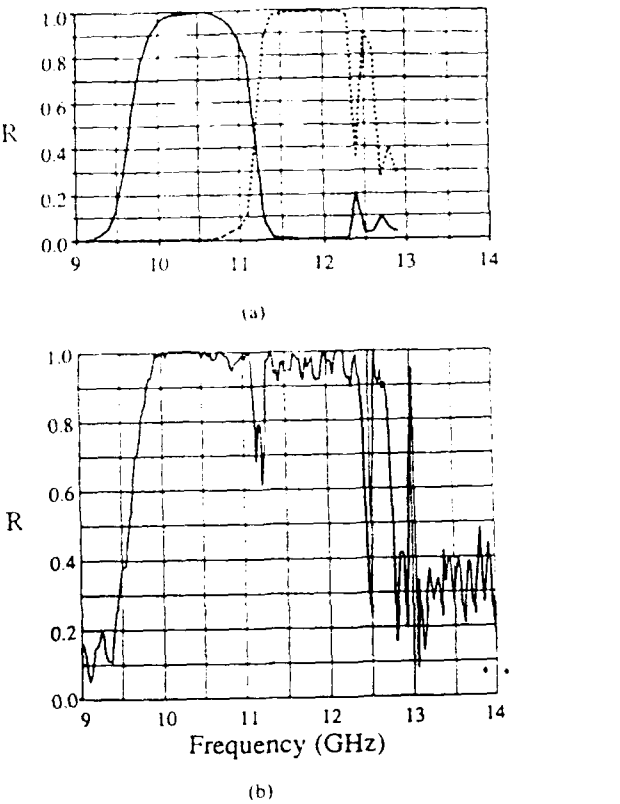

Fig. 9. Frequency dependence of reflection from Hamming-window gun-side reflector (Table II) (a) in TE_{11} (solid line) and TM_{11} (dashed line) modes from scattering matrix simulation and (b) from measurement. The input wave is in the TE_{11} mode.

pass through. The positive corrugation amplitude is defined with respect to the minimum inner wall radius.

Figs. 9(a) and 10(a) show the scattering matrix simulation results for the gun-side and output Bragg reflectors, respectively, described by Table II. Ohmic loss is included. The simulation found a peak reflectivity of 99.4% for the gun-side reflector and 96.0% for the output reflector. For an injected TE_{11} wave, the simulation also found that the reflected wave at 10.6 GHz from both the gun-side and the output reflector is 99.9% TE_{11}. The measured S_{11} values for the corresponding reflectors are shown in Figs. 9(b) and 10(b). As shown in the figures, the results for the reflectivity and bandwidth are seen to be in excellent agreement with theory. As predicted by the simulation, the frequency dependence of the reflection for both tapered reflectors is very smooth compared with the untapered sinusoidal corrugation measurement (Fig. 7(b)).

The transmission characteristics of the Hamming-window reflectors are shown in Fig. 11. The results from the scattering matrix simulation are shown in parts (a) and (b) of the figure for the gun-side and output reflectors, respectively. At the design frequency of 10.6 GHz, the gun-side reflector transmits only 0.085% of the input TE_{11} wave in the TE_{11} mode and 0.10% in the TM_{11} mode, while the output reflector transmits 3.41% in the TE_{11} mode and 0.11% in the TM_{11} mode.

III. Resonator

A. Theory

A Bragg resonator cavity can be formed by separating two corrugation sections by a smooth section of length L_R. The diffractive quality factor for the cavity can be approximated by the well-known expression [1]

$$Q = (\omega/c)^2 L_R/[k(1 - R_1 R_2)]. \tag{40}$$

where R_1 and R_2 are the reflectivities (in amplitude) of the two corrugated sections. However, the above result is only valid for

$$GL_R \gg 1 \tag{41}$$

$$R_1 \simeq 1 \tag{42}$$

$$R_2 \simeq 1. \tag{43}$$

A better prediction for Q, including intercoupling as well as the energy resonating inside the reflectors themselves, can be obtained by using the previous eigenvalue/eigenvector method (eq. (23)) for the sinusoidal corrugation reflectors. In this analysis, the wave is injected through one of the two reflectors. In the resonating section, the uncoupled amplitudes satisfy

$$dA_j^{\pm}/dz = \mp(\alpha_j + ik_j)A_j^{\pm} \tag{44}$$

or (45), shown at the bottom of the next page.

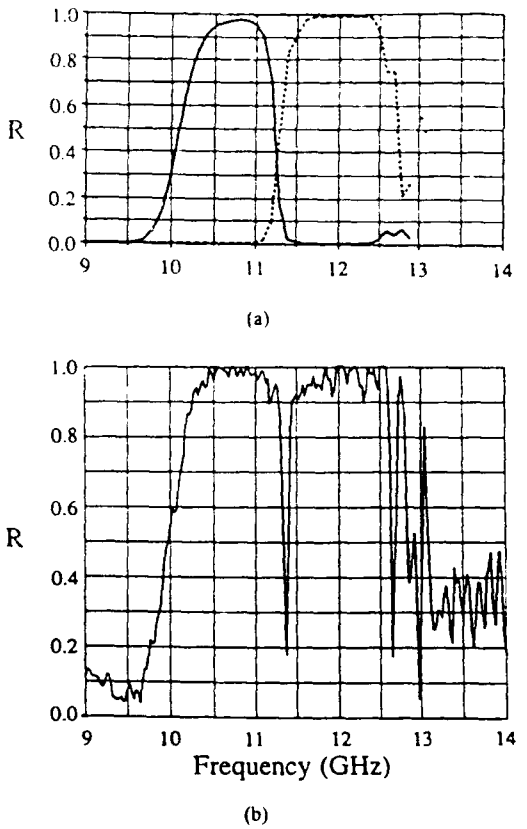

Fig. 10. Frequency dependence of reflection from Hamming-window output reflector (Table II) (a) in TE_{11} (solid line) and TM_{11} (dashed line) modes from scattering matrix simulation and (b) from measurement. The input wave is in the TE_{11} mode.

TABLE II
PARAMETERS OF HAMMING-WINDOW BRAGG REFLECTORS FABRICATED FOR 10.6 GHz CARM OSCILLATOR EXPERIMENT

	Gun-Side	Output
Period	1.500 cm	1.500 cm
Mean radius	1.809 cm	1.809 cm
Corrugation amplitude	0.400 cm	0.325 cm
Corrugation length	36.75 cm	36.75 cm
ω/ω_c	2.2	2.2
Corrugation orientation	positive	positive
Corrugation profile	tapered	tapered
Corrugation geometry	rectangular	rectangular

The matrix $\mathcal{M}$ for the smooth section is therefore composed of only the propagating constants for the TE_{11} and TM_{11}

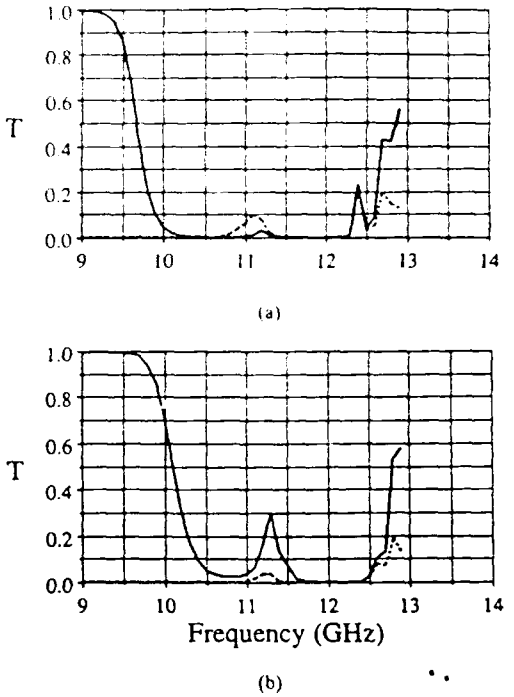

Fig. 11. Frequency dependence of TE_{11} (solid lines) and TM_{11} (dotted lines) mode transmission through Hamming-window reflectors (Table II) from scattering matrix simulation for (a) gun-side reflector and (b) output reflector. The input wave is in the TE_{11} mode.

modes. There are four eigenvalues and eigenvectors in the resonator section and each of the reflectors and therefore a total of 12 unknown coefficients. A unique solution for the wave amplitudes can be obtained when 12 boundary conditions are specified. In addition to the four input and output boundary conditions, the eight additional boundary conditions are realized by the continuity of the waves at the two ends of the resonating section.

Fig. 12 shows the predicted frequency response of energy resonating in a Bragg cavity with two Bragg reflectors described by Fig. 3(a) and separated by a smooth section of length $L_R = 5$ cm. The calculation includes an ohmic loss of twice the theoretical value in both the reflectors and the central resonator section. The modes at 249.0 GHz and 250.2 GHz are predominantly TE_{11}, while the mode at 251.0 GHz is approximately a 50% mixture of TE_{11} and TM_{11}. The Q of a mode in the resonator can be calculated as

$$Q = \frac{f_0}{\Delta f}, \tag{46}$$

where f_0 is a resonant frequency and Δf is the half-power width. This gives Q values of 11 000 and 4000 for the modes at 249 GHz and 250.2 GHz, respectively.

$$\frac{d}{dz}\begin{pmatrix} A_H^+ \\ A_H^- \\ A_E^+ \\ A_E^- \end{pmatrix} = \begin{pmatrix} -(\alpha_H + ik_H) & 0 & 0 & 0 \\ 0 & (\alpha_H + ik_H) & 0 & 0 \\ 0 & 0 & -(\alpha_E + ik_E) & 0 \\ 0 & 0 & 0 & (\alpha_E + ik_E) \end{pmatrix}\begin{pmatrix} A_H^+ \\ A_H^- \\ A_E^+ \\ A_E^- \end{pmatrix} \tag{45}$$

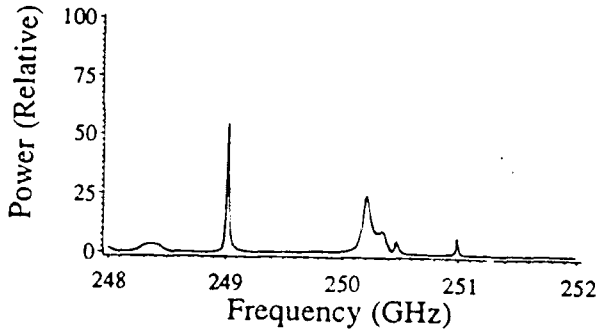

Fig. 12. Frequency response of resonator with two sinusoidal corrugation reflectors described in Table I (case (a)) for L_R = 5.0 cm (ohmic loss included).

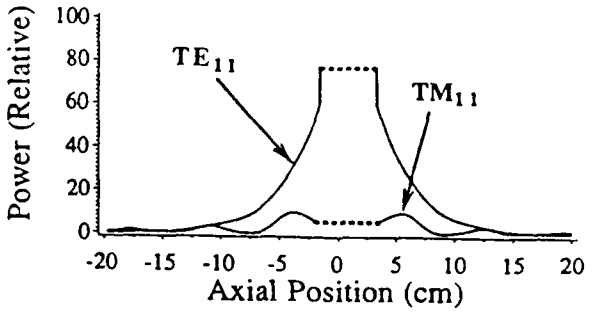

Fig. 13. Spatial variation of the mode from Fig. 12 at 249.0 GHz for L_R = 5 cm. The dashed line shows the envelope of the energy profile and the solid line shows the energy profile itself.

The spatial profile of the central mode (f = 249.0 GHz) from the resonator described in Fig. 12 is shown in Fig. 13. It is evident that a significant amount of energy leaks into each reflector from the cavity region.

B. Measurement

Two Bragg resonators, one with the sinusoidal corrugation reflectors described in Table I (case (b)) and the other with the two dissimilar Hamming-window Bragg reflectors described in Table II, were formed by separating two reflector sections by a smooth uncorrugated aluminum tube. The inner radius of the smooth central section is equal to the minimum inner radius of the corrugation for both resonators. The transmission method has been used to measure the resonant frequency and Q of the modes in both cavities. The signal was coupled in and out through ports on the sidewall of the smooth resonator section.

The transmission method measures the loaded Q of the resonating system, given by

$$\frac{1}{Q_L} = \frac{1}{Q_{\text{Bragg}}} + \frac{1}{Q_{\text{ohmic}}} + \frac{1}{Q_{\text{ext}}}. \tag{47}$$

In order to directly measure the quality factor Q of the Bragg cavity, Q_{ext} must be large compared with Q_{Bragg}. The value of Q_{ext} can be adjusted by decreasing the coupling strength of the sidewall coupling port such that

$$Q_{\text{ext}} \gg Q_{\text{Bragg}}. \tag{48}$$

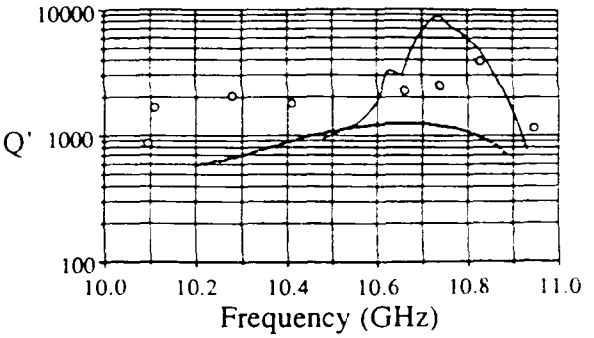

Fig. 14. Theoretical dependence of a sinusoidal Bragg resonator's quality factor on frequency from measurement (open circles), the eigenvalue/eigenvector method (solid line), and eq. (40) (dashed line). The reflectors are described in Table I (case (b)) and the variable smooth section's length is approximately 23 cm (ohmic loss included).

Then, the effective loaded Q of the resonator, neglecting Q_{ext}, is given by

$$\frac{1}{Q'_{\text{Bragg}}} = \frac{1}{Q_{\text{Bragg}}} + \frac{1}{Q_{\text{ohmic}}}. \tag{49}$$

Both the experimental and theoretical values of Q'_{Bragg} have been found over the bandwidth of the sinusoidal corrugation Bragg reflector by changing the length of the smooth section of the resonator, thereby changing the resonant frequency of the mode. The theoretical values are calculated for the $\text{TE}_{1,1,15}$ axial mode. The measurements of Q'_{Bragg} are shown in Fig. 14 along with the theoretical predictions from the eigenvalue/eigenvector method, which includes ohmic losses equal to twice the theoretical value, and the qualitative approximation (eq. (40)) using the theoretical values of R from Fig. 7(a). The experimental bandwidth for Q'_{Bragg} is broader than the theoretical prediction, as was the experimental bandwidth for reflectivity.

The measured Q'_{Bragg} of the resonator with Hamming-window Bragg reflectors is shown in Fig. 15 along with the qualitative approximation (eq. (40)) using the reflectivity predicted by the scattering matrix code. The measured Q'_{Bragg} over the bandwidth is in very good agreement with the theoretical prediction. Considering the sensitivity of (40) on $1/(1 - |R_1||R_2|)$ for $|R_1||R_2| \approx 0.95$, the small discrepancy in the Q values is quite reasonable.

IV. Conclusions

Measurements of the reflectivity characteristics of sinusoidal corrugation and rectangular corrugation, both tapered and untapered, have been compared favorably with theory. It was shown that both sinusoidal and rectangular corrugation can be used as a Bragg reflector. Tapered corrugation was shown to reduce mode conversion in the reflector and thus yield a reflector with high mode purity.

Q measurements of Bragg resonators with sinusoidal corrugation reflectors and Hamming-window reflectors were also presented. It has been shown that Bragg reflectors can provide a high-Q, frequency selective resonator with good mode purity.

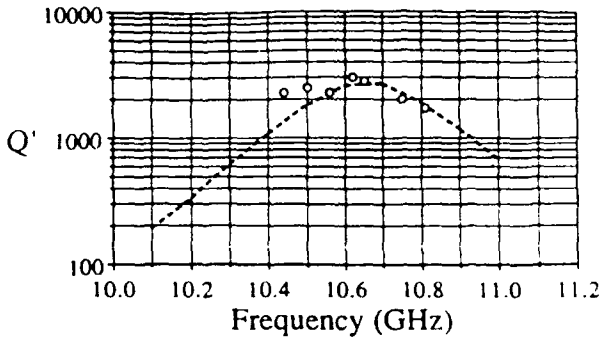

Fig. 15. Theoretical dependence of a Hamming-window Bragg resonator's quality factor on frequency from measurement (open circles) and eq. (40) (dashed line). The two dissimilar reflectors are described in Table II and the variable smooth section's length is approximately 24 cm (ohmic loss included).

ACKNOWLEDGMENT

The authors wish to thank R. Stever for performing careful measurements of the LLNL Bragg reflectors.

REFERENCES

[1] V. L. Bratman, G. G. Denisov, N. S. Ginzberg, and M. I. Petelin, "FEL's with Bragg reflection resonators: Cyclotron autoresonance masers versus Ubitron," *IEEE J. Quantum Electronics*, vol. 19, no. 3 pp. 282–293, 1983.

[2] T. J. Orzechowski *et al.*, "High-efficiency extraction of microwave radiation from a tapered-wiggler free electron laser," *Phys. Rev. Lett.*, vol. 57, no. 17 pp. 2172–2175, 1986.

[3] L. Solymar, "Spurious mode generation in nonuniform waveguide," *IRE Trans. Microwave Theory and Techniques*, vol. MTT-7, pp. 379–383, 1959.

[4] R. B. McCowan, A. W. Fliflet, S. H. Gold, V. L. Granatstein, and M. C. Wang, "Design of a waveguide resonator with rippled wall reflectors for a 100 GHz CARM oscillator experiment," *Int. J. Electronics*, vol. 65, no. 3 pp. 463–475, 1988.

[5] G. G. Denisov and M. G. Reznikov, "Corrugated cylindrical resonators for short-wavelength relativistic microwave oscillators," *Izv. Vyssh. Ucheb. Zaved. Radiofiz.* vol. 25, no. 5, pp. 562–569, 1982.

[6] Q. S. Wang *et al.*, "Cyclotron autoresonance maser amplifier and oscillators," in *Dig. IEEE Int. Electron Dev. Meeting*, 1989, pp. 759–762.

[7] B. Kulke, M. Caplan, and R. D. Stever, "250 GHz cold tests for the LLNL CARM experiment," in *Dig. Particle Accelerator Conf.*, 1991, pp. 763–765.

[8] M. Thumm, "Computer-aided analysis and design of corrugated TE_{11} to HE_{11} mode converters in highly overmoded waveguides," *Int. J. Infrared and Millimeter Waves*, vol. 6, no. 7, pp. 577–597, 1985.

[9] T. Itoh, *Numerical Techniques for Microwave and Millimeter-Wave Passive Structures*. New York: Wiley Interscience, 1989.

[10] J. Pretterebner and M. Thumm, "Design of improved Bragg reflectors for resonators in over-moded high-power microwave oscillators," in *Dig. Infrared and Millimeter Wave Conf.*, *SPIE 1514*, 1990, pp. 298–300.

[11] Q. S. Wang, D. B. McDermott, A. T. Lin, N. C. Luhmann, and K. R. Chu, "High power CARM for high gradient rf linac," in *Proc. 1990 SPIE (1226) Conf. Intense Microwave and Particle Beams*, 1990, pp. 220–227.

Photographs and biographies of the authors were not available at the time of publication.